

Finite Elements for Linear Analysis of Micropolar Continuum and the Relationship between the Linked Interpolation and Interpolations on Lie Groups in Linear Form

Grbac, Laura

Doctoral thesis / Disertacija

2024

Degree Grantor / Ustanova koja je dodijelila akademski / stručni stupanj: **University of Rijeka, Faculty of Civil Engineering / Sveučilište u Rijeci, Građevinski fakultet**

Permanent link / Trajna poveznica: <https://urn.nsk.hr/urn:nbn:hr:157:519227>

Rights / Prava: [Attribution-NoDerivatives 4.0 International/Imenovanje-Bez prerada 4.0 međunarodna](#)

Download date / Datum preuzimanja: **2024-06-24**



Repository / Repozitorij:

[Repository of the University of Rijeka, Faculty of Civil Engineering - FCERI Repository](#)



University of Rijeka
Faculty of Civil Engineering

Laura Grbac

**Finite Elements for Linear Analysis of
Micropolar Continuum and the
Relationship between the Linked
Interpolation and Interpolations on Lie
Groups in Linear Form**

Doctoral Thesis

Rijeka, 2023

University of Rijeka
Faculty of Civil Engineering

Laura Grbac

**Finite Elements for Linear Analysis of
Micropolar Continuum and the
Relationship between the Linked
Interpolation and Interpolations on Lie
Groups in Linear Form**

Doctoral Thesis

Supervisor: Prof. Gordan Jelenić, PhD

Rijeka, 2023

Mentor rada: Prof. dr. sc. Gordan Jelenić

Doktorski rad obranjen je dana _____ na Građevinskom fakultetu Sveučil-
išta u Rijeci, pred povjerenstvom u sastavu:

1. Izv. prof. dr. sc. Dragan Ribarić, Sveučilište u Rijeci, Građevinski fakultet, predsjednik
2. Doc. dr. sc. Edita Papa Dukić, Sveučilište u Rijeci, Građevinski fakultet, član
3. Prof. dr. sc. Zdenko Tonković, Sveučilište u Zagrebu, Fakultet strojarstva i brodogradnje,
vanjski član

Acknowledgements

The findings presented in this thesis are the result of the work within the research project IP-2018-01-1732: "Fixed-Pole Concept in Numerical Modelling of Cosserats' Continuum" (*FIMCOS*), in addition to the "Young Researchers' Career Development Project – Training New Doctoral Students" grant, both financially supported by the Croatian Science Foundation. *Without these grants, this thesis would not have been achievable. Thus, I am immensely grateful for this opportunity.*

The greatest gratitude also goes to my supervisor, Prof. Gordan Jelenić, without whom the FIMCOS project and the entire conducted research within the project would not exist.

"Gordan, thank you very much for everything you have generously taught me, for the patience you have shown throughout the entire process, and for consistently guiding me back to the right track whenever I strayed. I greatly admire your commitment to your work, and I am sincerely lucky to have been your student."

Thanks a lot, to all the co-workers on the FIMCOS project for the pleasant meetings and the productive and healthy collaboration we have had. I would also like to thank all my dear colleagues from the Chair of Technical Mechanics for the quality working environment. My special thanks go to the head of the Chair, Edita; she has shown so many times that she cares about each member of our group, as well as the whole group in general. Thanks to Nina Č. for numerous conversations that motivated me countless times to keep pushing forward.

I also express my gratitude to the entire Faculty of Civil Engineering in Rijeka: the administration, the library, and all other colleagues. Many thanks go to Dominik Štrok for his help in carrying out the experimental part of this thesis, as well as to the Centre for Micro- and Nanosciences and Technologies, Laboratory for Precision Engineering and Micro- and Nanosystems Technologies with the valuable help of Assoc. Prof. Ervin Kamenar.

Special thanks to the Erasmus+ programme, which enabled my three-month student exchange

at the University of Ljubljana. Heartfelt thanks to Prof. Dejan Zupan, who kindly hosted me at the Faculty of Civil and Geodetic Engineering, and dedicated his precious time.

On a more personal note:

I am truly thankful to my whole family - Žiković, Kontošić, Milović, and Grbac - for their endless love and support. Without all of you, I wouldn't be where I am today.

Thanks to my dear friends from the "Rizikovanje" group. Spending time with you has always been like recharging the batteries, with a dose of optimism, laughter, understanding, and support. To put it simply, you are friends for life.

Many thanks to my dear Izabela, who has always offered a hand of friendship in any phase of life.

Enormous gratefulness goes to my dearest colleague, best friend, and husband Marin, for always being there. All the good words in the world are simply not enough.

This thesis is dedicated:

- to **the honour of the past**: to everyone who had the curiosity and courage to participate in the domino effect that shapes all the previous discoveries and the current knowledge we have access to.

- to **the gratitude of the present**: to all those who sustain the momentum of research and contribute to the development of existing knowledge, and also, to all those who have been supporting this research in any way.

- to **the faith in the future**: “Dear curious reader, a seeker of knowledge, I humbly hope that this thesis will somehow assist you in your quest to find answers to the questions you have asked yourself, and I also hope that it will ignite a thirst for further investigation.”

Abstract

The core of this thesis lies in the micropolar (Cosserats') theory of elasticity, developed as one of the possible generalisations of the classical (Cauchy's) theory, in order to describe the behaviour of heterogeneous materials with a pronounced internal structure (microstructure), which the classical theory neglects. In addition to the standard displacement field, an additional independent microrotation field exists in the micropolar theory due to the consideration of the microstructure of the material, and to completely describe the behaviour of a linear-elastic isotropic and centrosymmetric micropolar material, the values of six micropolar material parameters must be known. However, due to the lack of a reliable and accepted methodology for their determination, the theory is still not widely applied in practice. Therefore, this research is conducted through two major phases in order to somehow contribute to the development of the necessary methodology.

In the first part, a new family of finite elements of arbitrary order for the linear analysis of the micropolar continuum is presented, where the displacement field is interpolated by enhanced fixed-pole interpolation which arose from an investigated correlation between known interpolation schemes, originating from the analysis of geometrically exact 3D beams, highlighting here interpolations on Lie groups SE (3) – helicoidal interpolation and SR (6) – fixed-pole interpolation, in their linearised form, with a linked interpolation. The enhanced fixed-pole interpolation derived from this observed relationship represents a possible interpretation of the linked interpolation, which is widely used in the linear analysis of the Timoshenko beam, but is not sufficiently explored in the general micropolar continuum theory. Static and vibrational analyses of the micropolar continuum are conducted through several numerical examples, demonstrating improved efficiency of the newly developed finite elements compared to conventional elements.

In the second part, the newly developed finite elements are used for the identification of micropolar material parameters by inverse analysis based on two specific experiments. The first experiment involved a four-point bending virtual experiment on perforated specimens, where the value of the coupling number, as one of the two existing micropolar parameters in 2D, is determined by inverse analysis. The second example investigates the discrepancy between the theoretically predicted stress concentration factor around a circular hole in a plate subjected to uniaxial tension and the experimental results. In pursuit of improved theoretical predictions, the application of micropolar theory is explored and a detailed methodology based on parametric and inverse analysis is presented for this purpose. However, it is demonstrated that there is

no unique combination of micropolar parameters that simulates the experimental results for all tested specimens, and based on the conducted analysis, we indeed affirm that the micropolar theory is not suitable for materials with a very low-scale internal structure and can not predict the obtained experimental results.

Keywords: Cosserat theory of elasticity, micropolar continuum, finite element method, fixed-pole concept, linked interpolation, interpolations on Lie groups, identification of micropolar parameters, inverse analysis, stress concentration factor.

Sažetak

Srž istraživanja ovog doktorskog rada je mikropolarna (Cosseratova) teorija elastičnosti razvijena kao jedna od mogućih generalizacija klasične (Cauchyjeve) teorije s glavnom namjenom da opiše ponašanje heterogenih materijala s izraženom unutarnjom strukturom (mikrostrukturom) koju klasična teorija zanemaruje. Uzimanjem u obzir mikrostrukture materijala, u mikropolarnoj teoriji uz standardno polje pomaka, postoji dodatno neovisno polje mikrorotacije te da bismo mogli u potpunosti opisati ponašanje linearno-elastičnog izotropnog i centrosimetričnog mikropolarnog materijala, moramo poznavati vrijednosti šest mikropolarnih materijalnih konstanti. Ipak, zbog nedostatka pouzdane i usvojene metodologije za njihovo određivanje, teorija se još uvijek ne primjenjuje široko u praksi. Stoga je ovo istraživanje provedeno kroz dvije glavne etape kako bi se doprinijelo razvoju potrebne metodologije.

U prvom dijelu je predstavljena nova familija konačnih elemenata proizvoljnog reda za linearnu analizu mikropolarnog kontinuuma kod kojih se polje pomaka interpolira poboljšanom fixed-pole interpolacijom, a koja je proizašla na temelju međusobne usporedbe nekih već poznatih interpolacijskih shema čije je izvoriste u analizi geometrijskih točnih 3D greda s dobro poznatom interpolacijom. Ovdje su posebno istaknute interpolacije na Liejevim grupama $SE(3)$ – helikoidalna interpolacija i $SR(6)$ – fixed-pole interpolacija, u svom lineariziranom obliku. Ovako izvedena poboljšana fixed-pole interpolacija predstavlja varijantu vezane interpolacije koja se već široko koristi u linearnoj teoriji Timošenkovih greda, no njena primjena nije dovoljno istražena na mikropolarnom kontinuumu. Provedena je potom statička i vibracijska analiza mikropolarnog kontinuuma kroz nekoliko numeričkih primjera, gdje je na temelju konvergencijskih krivulja pokazano poboljšanje primjene novo razvijenih konačnih elemenata u usporedbi sa konvencionalnim elementima.

U drugom dijelu rada se novo razvijeni konačni elementi koriste za identifikaciju mikropolarnih materijalnih parametara inverznom analizom na temelju dva specifična eksperimenta. U prvom se provodi virtualni eksperiment na modelu perforiranih uzoraka za kojih se putem inverzne analize utvrđuje vrijednost jednog mikropolarnog parametra – faktora povezanosti. Drugi primjer razmatra razliku između teorijskih rješenja faktora koncentracije naprezanja oko kružne rupe u ploči podvrgnutoj jednoosnom rastezanju sa eksperimentalnim rezultatima. Kao moguću bolju teorijsku predikciju ispitujemo primjenu mikropolarne teorije za čiju je svrhu predstavljena detaljna metodologija temeljena na parametarskoj i inverznoj analizi. Međutim, pokazano je da ne postoji jedinstvena kombinacija mikropolarnih parametara koja simulira eksperimen-

talne rezultate za sve ispitane uzorke te na temelju provedene analize doista potvrđujemo da mikropolarna teorija nije prikladna za materijale s unutarnjom strukturom na maloj skali.

Ključne riječi: Cosseratova teorija elastičnosti, mikropolarni kontinuum, metoda konačnih elemenata, koncept nepomičnog pola, vezana interpolacija, interpolacije na Lievim grupama, identifikacija mikropolarnih parametara, inverzna analiza, faktor koncentracije naprezanja.

Contents

1	Introduction	1
1.1	Demand for generalised theories of elasticity	1
1.2	Micropolar continuum theory and its historical development	4
1.3	Numerical investigations of micropolar continuum	5
1.4	Experimental procedures in micropolar elasticity	9
1.5	Research aims	10
1.6	Thesis scope	11
1.6.1	Numerical analysis	11
1.6.2	Experimental analysis	12
2	Micropolar theory of elasticity	15
2.1	Generalised Cauchy's stress theorem	15
2.2	Equations of motion in linear analysis	28
2.3	Kinematic equations in linear analysis	29
2.4	Constitutive equations in homogeneous and isotropic linear elasticity	30
2.4.1	Micropolar material parameters	33
2.4.2	Plane stress and plane strain formulation	35
3	Manifestations of helicoidal interpolation and fixed-pole approach in linear elasticity	37
3.1	Problems arising from FEM implementation of beam theories with rotational degrees of freedom	39
3.2	Standard and innovative interpolations in non-linear problems with large 3D rotations and their linearised forms	44
3.2.1	Configuration of 3D geometrically non-linear beam	44

3.2.2	Standard (Lagrangian) interpolation of displacements and rotations	46
3.2.3	Helicoidal interpolation of displacements	47
3.2.4	Original fixed-pole interpolation	48
3.2.5	Linked interpolation	50
3.2.6	Relationships between the presented interpolations	51
3.3	Conclusion	53
4	Numerical analysis of micropolar continuum	55
4.1	Analysis of 3D micropolar continuum	56
4.1.1	Integral form of equations of motion	56
4.1.2	Hexahedral finite element with eight nodes	59
4.1.3	Numerical examples	61
4.2	Analysis of 2D micropolar continuum	75
4.2.1	Integral form of equations of motion	75
4.2.2	Quadrilateral micropolar FE with four and nine nodes	77
4.2.3	Numerical examples	78
4.3	Conclusion	85
5	Virtual experiments on perforated specimens	87
5.1	Capturing coupling number N – displacement calculation	88
5.1.1	Description of modelled specimens	88
5.1.2	Set-up	90
5.1.3	Virtual-experiment procedure	92
5.1.4	Inverse numerical analysis	95
5.2	Discussion	98
6	Experimental investigation of plates with circular hole under tension	101
6.1	Motivation: Why is stress concentration factor based on classical theory doubtful?	102
6.2	Experimental testing	107
6.2.1	Specimen description	107
6.2.2	Preparation for strain measurements	109
6.2.3	Experimental setup	111
6.2.4	Data collection	112

6.2.5	Control experiment	114
6.3	Numerical investigation based on the classical theory of elasticity	116
6.4	Numerical investigation based on the micropolar theory of elasticity	120
6.4.1	Numerical model based on the micropolar theory of elasticity	120
6.4.2	Results of parametric and inverse analyses	121
6.5	Conclusion	126
7	Conclusions and future work	129
7.1	Development of new micropolar finite elements	129
7.2	Identification of micropolar material parameters	130

Chapter 1

Introduction

1.1 Demand for generalised theories of elasticity

In nature, materials consist of discrete atoms connected by interatomic forces and surrounded by empty space, forming a crystal structure. This structure, along with possible occurrences of defects within it, determines the response of the material to external forces. In engineering, however, based on the idea that the material is treated as a continuous medium instead of considering the behaviour of individual atoms or molecules from which the material is made up, the concept of the continuum has been adopted [1]. Therefore, the continuum theory assumes that the material consists of an infinite number of points that completely fill a given volume, and that its behaviour can be described by applying a mathematical model to each point within the continuum. Such a simplified homogeneous model of a solid body averages out all microstructures of the material which are thus neglected [2]. In reality, most materials are non-homogeneous to varying degrees, where their influence at the macroscopic level depends on the scale of the material sample under consideration. For some materials (e.g. metals), various constituent phases that form their microstructures can only be observed at the microscopic level, while in other materials, such as foams or cork, the (micro)structure is visible by the naked eye and it cannot be neglected, since it significantly affects the material's response to loading [3, 4].

One of the materials commonly used for building structures is steel, in which properly arranged crystals already lead to anisotropy at the level of the crystal lattice that forms the steel structure. Additionally, various metal processing methods change the orientation of the crystals, bringing impurity grains (remnants from other materials) and air bubbles into the metal blocks. Metal rolling is one such process in which the introduced air bubbles and impurities are stretched

in the rolling direction. At the microscopic level, the deformation depends on the behaviour of the individual microstructural phases and their interaction with the surrounding phases. On the other hand, at the macroscopic level, steel is considered as a homogeneous and isotropic material, whose macroscopic behaviour can be accurately described by the classical continuum theory, which actually averages its microscopic response [5]. Therefore, the classical theory of elasticity developed by the French mathematician and physicist Augustin Louis Cauchy in the 19th century as a branch of continuum mechanics, is commonly used to analyse the strain and stress conditions of (macroscopically) homogeneous bodies under external loads. Hooke's law, which describes the linear-elastic relationship between the deformation of a body and the applied external force, was one of the starting points in developing the theory of elasticity. Many scientists such as Lamé, Poisson, Green, Airy, Kirchhoff, Lord Rayleigh, Saint-Venant, Timoshenko and many others have also contributed to the development of the theory [2,6–8].

In classical theory, the static interaction between two material particles of a body is described only by a force vector. Of course, it is natural to conclude that in addition to the resultant of interparticle forces, there is also a resultant moment of these forces, but according to the fundamental principle of continuum mechanics, which states that a body is considered as a continuum containing infinitely many points, where the surface of each continuum element tends to zero, the resultant moment disappears as a result. In other words, this means that no distributed moment can be applied in classical linear theory and therefore, the response of a body under the action of external forces is described by a stress and strain tensor, both of which are symmetric [9].

However, if we want to describe the behaviour of materials with a more pronounced microstructure in relation to the observed sample scale, the classical theory of elasticity does not provide the best solution compared to the results obtained from experiments on specimens made for example, of bones, foams or lattice structures [10,11]. Metal foam is also an example of a significantly heterogeneous and anisotropic material consisting of metal particles and gaseous substances. Due to their good properties, which include low density, fire resistance, low thermal conductivity and high sound absorption, metal foams are increasingly used for sandwich panels, facade cladding for buildings, aircraft wings, various parts in the automotive industry, etc. [12]. Precisely because of the development of new material types and the increasing use of heterogeneous materials in structural elements, the quest for a more convenient model that better describes their behaviour is an active research topic.

Due to the absence of microstructure of the material in the classical idealised and homoge-

neous model, regardless of its observed scale, the classical theory cannot describe the so-called *size-effect*, an experimentally observed phenomenon in which the smaller specimens seem to be stiffer than the larger ones made of the same material [13]. Additional deviations between the experimental results and theory appear in dynamic problems, specifically in the cases of elastic vibrations characterised by high frequencies and small wavelengths (i.e. ultrasonic waves), where the microstructure of the body also becomes a significant factor [10]. Furthermore, many published papers bring to light that the classical theory overestimates stress concentration factor values near geometric discontinuities, where one such example is a homogeneous plate with a circular hole in the centre under symmetric uniaxial loading [10, 11]. Hence, in order to more realistically describe the behaviour of materials with a pronounced microstructure and to capture the above-mentioned effects that the classical theory cannot, various alternative theories have been developed that generalise the classical theory and incorporate heterogeneity and scale size, which contributes to the understanding of the complex behaviour of both natural and artificially produced materials under different conditions and allows better prediction of their behaviour in practice.

The step up from the classical (local) theory begins with the development of non-local theories, in which the stress state at the considered point depends not only on the deformation at that point, but also on the deformations of surrounding points. These include gradient theories, polar theories and peridynamics among others. Polar theories assume that material points possess additional information about the orientation and structure of the material, and the crucial difference between these types of theories is the way in which microstructural effects are incorporated into the modelling of strain and stress in the material. Compared to the classical theory, a material point in the micromorphic continuum theory has three additional deformable directions, including nine degrees of freedom, consisting of microrotation, microstretch, and microshear [3]. The microstretch theory [3] can then be derived from the micromorphic theory by eliminating the microshears of the material particles. As a result, in the microstretch theory, a material particle is considered as a volume element with three microrotation and one dilatational stretch (microstretch) degree of freedom. Eliminating the dilatational microstretch, we arrive at the micropolar theory [3], in which a material particle has microrotational degrees of freedom that give it an orientation which is independent of displacements. If the microrotations are equal to the macrorotation, this theory reduces to the couple-stress theory, which belongs to the gradient theories (for more details see e.g [3, 7, 14]).

1.2 Micropolar continuum theory and its historical development

The main interest of this thesis lies in the exploration of the micropolar (Cosserats') theory of elasticity, in which the static interaction between two material particles is described using both a stress vector and a couple-stress vector. It follows that there are now two stress tensors, both of which are non-symmetric [15]. Given that there is an additional couple-stress tensor, there is also an additional angular strain tensor (curvature) that represents the gradient of the additional kinematic field - the microrotation [3]. Microrotation represents the orientation of each material point and it is completely independent of the skew-symmetric part of the displacement gradient at the observed point (macrorotation). If we consider a linear-elastic isotropic centrosymmetric material according to the micropolar theory, the connection of two independent stress and couple-stress tensors with strain and curvature tensors is described by two fourth-order constitutive tensors consisting of six independent material parameters in total: Young's modulus and Poisson's ratio, which are already known from the classical theory; the coupling number which gives us the ratio between the microrotation and the macrorotation, the polar ratio which has a similar effect in torsion as the Poisson's ratio has in axial deformation, and the last two are the characteristic lengths for torsion and for bending [10].

The first generalisation of Cauchy's theory of elasticity goes back to the work of German physicist Woldemar Voigt, who in 1887. proposed a mathematical model that describes the interparticle static interaction of a body not only by a force vector but also by a moment vector [16]. He also gave both differential equilibrium equations from which he obtained non-symmetric stress and couple-stress tensors. Twenty-two years later, as an extension of Voigt's work, a complete non-symmetric theory of elasticity was developed by the Cosserat brothers (Eugene, who was a mathematician and Francois, who was an engineer) throughout their thirteen years of work. In their theory, the Cosserat brothers assumed that each material point in a deformable body has an attached rigid triad, also known as a "trièdre", which consists of three mutually orthogonal vectors denoted as \mathbf{e}_1 , \mathbf{e}_2 and \mathbf{e}_3 . The Cosserat brothers proposed that the triad can translate and rotate independently during the deformation process, allowing for the description of small-scale translations and rotations of material elements. By introducing a new degree of rotational freedom, we can give each particle an orientation. Moreover, the brothers obtained equations for the equilibrium of momentum for the dynamic case [15], but they did not give a specific microinertia nor a conservation law for the microinertia tensor, which are crucial to

solve dynamic problems in solids and flowing media [3]. This material model was later called the Cosserat (or micropolar) continuum. Unfortunately, the elder brother Francois died prematurely five years after the publication of their theory. The other brother was no longer answerable to the theory of elasticity because he was unwilling to confront the anguish of recalling their years of fruitful collaboration [17]. Despite its novelty, the theory remained untouched for almost half a century until several independent authors reopened it: Grad [18] derived constitutive equations for a linear polar fluid, Günther [19] and Schafër [17] recapitulated linear Cosserat elasticity and showed that the continuum used in dislocation theory is an incompatible Cosserat continuum. A few years later, Mindlin, Tiersten [20], and Toupin [21] introduced the so-called Cosserat pseudo-continuum (couple-stress theory), in which the non-symmetric stress tensor is retained but the microrotation coincides with the macrorotation. In 1964, A. C. Eringen [3] extended the linear Cosserat theory by including the missing microinertia effects of the body, the law of conservation of microinertia and he renamed it the micropolar theory of elasticity. Since the "reopening" of the theory, it has been further developed in detail, e.g., [22, 23], but it is still not widely considered in the numerical analysis of structures in practical applications. The key to a broader application of the micropolar theory lies in the knowledge of the material parameters, for which a reliable methodology for detection has not yet been determined.

1.3 Numerical investigations of micropolar continuum

In the 80's of the last century, numerical methods began to be used in the analysis of the micropolar continuum, in particular the finite element method, since it is additionally difficult and often impossible to obtain analytical solutions in closed form for many problems with complex geometry or dynamic problems of micropolar elasticity. There are a large number of papers about linear static analysis of the micropolar continuum using the finite element method. The first researchers who implemented the micropolar theory into finite elements were Baluch, Goldberg, and Koh in [24] where they formulated a simple triangular finite element using linear interpolation to interpolate both unknown fields. However, up to that point, they did not present any numerical example. Two years later, Goldberg and his colleagues [25] formulated a triangular micropolar plate element with three nodes and five degrees of freedom per node (vertical displacement, two rotations, and two microrotations) to model the bending problem of micropolar plates. Numerical results for classical and micropolar elasticity were compared, and their difference is a consequence

of the influence of micropolar material parameters.

Another attempt to formulate displacement-type finite elements based on micropolar elasticity was given by Nakamura et. al. [26], where 1st order triangular elements with Lagrangian interpolation were used. The developed finite elements were verified on the numerical example of an "infinite" plate with a circular hole for an isotropic micropolar material for which an analytical solution is known [27]. The authors have made a comparison between isotropic and orthotropic micropolar material cases and have generally concluded that there is a dependence between the stress concentration factor and micropolar material parameters. Ghosh and Liu [28] presented a new Voronoi cell finite element model for the analysis of steady-state heat conduction and micropolar thermoelastic stress problems for heterogeneous materials. The finite elements for isotropic and orthotropic axisymmetric micropolar continua based on the variational principle (principle of virtual work) presented in [26], were developed in Huang's doctoral thesis under the supervision of Dr. Sachio Nakamura [29]. To solve a 3D micropolar elasticity problem, Huang used isoparametric Lagrangian elements with eight nodes and twenty nodes, while for a 2D problem, he used elements with four and eight nodes. The numerical procedure was coded in Fortran programming language, and to verify the developed planar finite elements, the patch test of a simple uniform tension was conducted. The second numerical example was a U-shaped circumferential groove in a bar of circular cross-section discretised by hexahedral elements with 20 nodes. Huang compared the numerical results for an arbitrary ratio between the radius of the groove r and the thickness of the bar d for the case where the coupling number fades away (which turns out to be the classical theory as a special case) with the known Peterson's stress concentration factor curves obtained by a combination of experimental measurements and theoretical analyses of the stress distribution [30]. The numerical results were found to agree well with the empirical solutions, with only minor deviations in the case of a smaller $\frac{r}{d}$ ratio, and it was also shown that increasing the value of the coupling number resulted in an increase in the value of stress concentration [29]. However, the micropolar elements were not fully verified at that time. Later, Huang et al. [31] formulated a 3D brick element with Wilson's incompatible modes to solve the micropolar elastic beam problems.

In 1995, Nakamura and Lakes developed a finite element analysis program named MIRACS (MIcroRotation And Couple-Stress) [32], in which micropolar CST and quadrilateral finite elements with four or eight nodes were implemented. In their work, they primarily investigated the Saint-Venant principle for the case of a micropolar continuum, specifically on the example

of a strip loaded with a concentrated force at one end. This showed a slower rate of decay of stress as we move away from the considered position from the point of applied force, compared to the classical continuum where a faster stress diffusion is expected with increasing distance from the applied load. The micropolar continuum may exhibit slower homogenization of the stress distribution due to microstructural effects, i.e., the distribution is slower as the characteristic length increases. Yang and Huang [33] analysed the relationship between Poisson's ratio and micropolar parameters for the rectangular plate subjected to uniform tension and discretised by a linear triangular finite element with three degrees of freedom per node. Providas and Kattis [34] introduced a set of three patch tests to completely validate the micropolar finite elements (tests that reproduce the condition of constant symmetric stress and strain, constant non-symmetric shear, or constant curvature). They derived three displacement/rotation-type triangular finite elements using the principle of minimum potential energy: the bi-linear element MLINT with three nodes, the six-node element with quadratic interpolation for the displacement field and linear interpolation for the rotation MQLT, and the bi-quadratic finite element MQUAT with six nodes. All three elements were tested through the presented set of patch tests and, in addition, their solutions were compared on a numerical example of the stress concentration around the circular hole in an "infinite" plate with the known analytical solution according to Neuber [35]. It was shown that the MQLT elements clearly give the best results.

Li et al. [36] performed a linear analysis of a 2D micropolar continuum using quadrilateral elements Q4 with Lagrangian interpolation and Q8 with bubble mode, which were found to be resistant to mesh distortions. Korepanov et al. [37] performed 2D and 3D finite element analyses on several problems with stress concentration and compared the results with analytical ones. As an alternative to the finite element method, M. A. Wheel and co-workers [4, 38, 39] used a control volume-based finite element method to model micropolar elasticity, where their elements pass the required patch tests and also have an accuracy that is at least equal to their standard FE counterparts. Grbčić et al. [40] developed a 1st order hexahedral finite element enhanced with incompatible modes, concluding that this element highly reduces the computational cost for the cylindrical bending problem and correctly predicts the *size-effect* phenomenon in bending and torsion. Moreover, Grbčić et al. [41, 42] developed triangular and quadrilateral finite elements of different order for linear micropolar continuum theory using the linked interpolation for displacement field. In order to assure the convergence, they applied Petrov-Galerkin method to the proposed element formulations. Xie et al. [43] proposed a hybrid FE formulation to improve the

bending response of four-node quadrilateral and eight-node hexahedral for Cosserat elasticity problems without compromising the constant couple-stress patch test.

The literature on the linear dynamic numerical analysis of the micropolar continuum is somewhat sparser. Among the first who considered the application of the finite element method to static and dynamic problems in micropolar elasticity was Padovan [44], who developed a 3D formulation based on a semi-analytical finite element procedure. A development of displacement and rotation-based dynamic finite element formulation for Cosserat plates was presented by Godio et al. [45]. Ansari et. al. [46] investigated the influence of micro-structures on the free vibration behaviour of 3D micropolar beams and plates with various boundary conditions using 27-node micropolar finite elements. They observed a decent difference among numerical results for non-dimensional frequencies of micropolar structures and their classical counterparts for a small ratio between the thickness of the structure and the characteristic length for the bending, showing the necessity of considering microstructure effects on the size-dependent problems. Kohansal-Vajargah et. al. [47] studied the free vibration response of micropolar planar structures using linear isoparametric micropolar finite elements with 4 nodes. Furthermore, Kohansal-Vajargah and Ansari [48] studied the effect of length scale parameters on the dimensionless natural frequencies of 3D micropolar structures of various geometries using isoparametric quadratic tetrahedral micropolar finite elements with 10 nodes.

In recent publications, the application of the micropolar theory appears as a natural choice in advanced numerical simulations of auxetic materials [49], sands [50], granular media [51], dilatation effect in layered rocks with rough surfaces [52], crack propagation [53], cortical bones [54], blood flow through a stenosed artery [55], bio-ceramic materials for bone reconstruction [56], etc. However, the problem of the value of the material parameters is constantly present, which prevents a wider application of the theory in practice. Further development of high-quality micropolar finite elements is of great importance for future progress and a comprehensive understanding of Cosserat's continuum theory, both as a simulation tool directly applicable to engineering problems and as a reliable modelling tool in virtual experimental setups to determine material parameters by inverse analysis.

1.4 Experimental procedures in micropolar elasticity

Based on a standardised tensile test on a solid specimen, classical parameters such as Poisson's ratio and Young's modulus can be determined very easily. However, when it comes to determining additional micropolar parameters, the simplicity is lost. Determination of micropolar material parameters is a significant and demanding task that requires, above all, suitable and precise experimental equipment, as emphasized by Eringen's quote [3]:

"... experiments with micropolar constants require much precision and elaborate instrumentation, since we are faced with the measurements of microscopic-level quantities ... At this range, many other physical phenomena begin to interfere with observation, introducing distortions and errors."

Schijve [57] was the first who attempted to obtain the value of the characteristic length of sheet specimens made of aluminium alloy subjected to bending. He studied the effect of the sheet thickness on the flexural rigidity, but the size effect was not recorded. Furthermore, Ellis and Smith [58] studied the thin plates of steel and aluminium under cylindrical bending and found that the characteristic length of homogeneous metals is of the order of atomic particle distances and that this influence was negligible. Because of the immeasurability of this length scale (microscopic effects are insignificant compared to macroscopic material behaviour, so the micropolar theory is not required to describe such materials), the studies did not yield specific values for the characteristic length. Although these investigations were unsuccessful, they pointed scientists in the direction of studies on materials with a more pronounced microstructure compared to metals (e.g., [59]).

The analytical and experimental procedure for the determination of the micropolar material parameters was given by Gauthier and Jahsman in [60] as well as in comprehensive Gauthier's doctoral thesis [61], but apparently without particular success in the experimental part, since an opposite trend to the expected one has been observed (*anti-micropolar behaviour*). They derived analytical solutions based on the micropolar theory for a rectangular plate under cylindrical bending and for a cylinder under axial tension or torsion. In order to validate the analytical solutions with experiments, composite specimens were artificially created using an epoxy matrix with uniformly distributed aluminium shots that have elastic modulus 20 times higher than the epoxy resin. The Poisson's ratio and Young's modulus were obtained by measuring the axial and radial displacement of a cylinder subjected to tensile loading. Three cylinders of different

sizes were subjected to torque moment, where the occurrence of a *size-effect* was expected. Through this test, by calculating the torsional rigidity for several different samples, the value of the characteristic length for torsion and the polar ratio could be obtained. However, an inverse trend in behaviour was observed, i.e., the thinner specimens exhibited less rigidity than the thick ones. The third experiment, which we shall call *Gauthier's pure-bending test*, is still of interest to scientists and will be discussed in more detail in Chapter 5. Bigoni and Drugan [62] shed a light on the reason why Gauthier's specimens exhibited behaviour contrary to expectations; a composite material will behave as micropolar if the inclusions of the material is less stiff than its matrix. Later, the anti-micropolar behaviour of the material has also been frequently reported (e.g. [63]).

Further significant contributions in experimental procedures for determining micropolar material constants are provided by Lakes and his co-workers, who investigated *size-effect* phenomena (e.g. [11, 64, 65]) and conducted experiments on specimens of various materials [13, 65, 66]. Nowadays, his main focus is on the study of auxetic materials and experimental investigation of material parameters on 3D printed samples [67–70]. Unfortunately, the experimental validation is still insufficient, and the way to understand and develop accurate experimental procedures can be sought in reliable and robust numerical algorithms, which should broaden the range of solvable problems and open new opportunities for numerical simulation of experimental schemes.

1.5 Research aims

The **research aims** of this thesis are:

1. To conduct a study on the manifestation of interpolations on Lie groups SE (3) - helicoidal interpolation and SR (6) - fixed-pole approach in linear analysis and their relationship with the linked interpolation.
2. Development of a new enhanced fixed-pole interpolation and investigation of its application in the static and dynamic analysis of the Timoshenko beam.
3. Development of new 2D and 3D finite elements for linear static and dynamic analysis of the micropolar continuum using the enhanced fixed-pole (*EFP*) interpolation for the displacement field.
4. Establishment of the value of the coupling number for perforated high mass density (HMD)

aluminium specimens through the numerical simulation of the pure bending test.

5. To determine whether the classical theory can accurately describe the strain field and the value of stress concentration of aluminium strips with a hole under tension, based on the presented precise methodology that compares numerical and experimental results obtained.
6. To investigate whether the micropolar theory can provide a more suitable model for describing the problem discussed in point 5 and to propose a methodology for identifying additional micropolar parameters.

1.6 Thesis scope

The research carried out in the framework of this dissertation consists of two main parts:

- (i) Static and dynamic numerical analysis of a micropolar continuum using newly developed micropolar finite elements with the enhanced fixed-pole interpolation
- (ii) Experimental investigation on the problems in which some effects are expected to be described by the micropolar theory and where we aim to determine the micropolar material parameters using the newly developed finite elements.

1.6.1 Numerical analysis

As a starting point, we present in Chapter 2 a linear elastic micropolar model, where the equations of motion, kinematic and constitutive equations for the 3D micropolar continuum are given. Problems in the numerical implementation of the micropolar continuum may arise due to the existence of an additional kinematic field (microrotation). Depending on the choice of interpolation functions for interpolating the unknown fields, the shear-locking effect (in linear analysis) and the problem of non-objectivity (additionally in the case of non-linear analysis) may occur. Hence, in order to develop high-quality micropolar finite elements, we investigate in Chapter 3 how two different approaches (helical interpolation and fixed-pole approach) emerged from an analysis of geometrically exact beams and manifest themselves in the linear analysis. Then for the purpose of improvement, we investigate their relationship with the linked interpolation which is known to provide an exact solution for the Timoshenko beam for arbitrary polynomial loading of order p and a sufficient finite number of nodal points m ($m \geq p + 4$, $m \geq 3$ for point loading). Based on this study, the enhanced fixed-pole interpolation (EFP) is derived.

Motivated by the good properties of EFP interpolation in the numerical analysis of the 1D micropolar continuum (Timoshenko beam), we derive a formulation for a 3D micropolar finite element in Chapter 4, where EFP interpolation is used to interpolate the displacement field, while the microrotation field is interpolated by Lagrangian polynomials. After ensuring the convergence of the newly developed finite elements through a set of patch tests, two additional static benchmark problems are analysed, followed by a vibration analysis of 3D plates with different geometries and boundary conditions, comparing the numerical solutions with those obtained using Lagrangian elements. Moreover, we also present the membrane micropolar finite elements by reducing the newly developed formulation which are then applied in the vibrational analysis of the 2D micropolar continuum.

1.6.2 Experimental analysis

Two specific tests that are expected to be better described by the micropolar theory have been experimentally analysed here:

- (a) In Chapter 5, a four-point bending test on aluminium HMD specimens with artificially drilled holes in a regular pattern has been carried out based on Gauthier’s problem. Following [71] where the characteristic length for bending was determined based on Gauthier’s analytical solution and experimentally obtained strains measured by strain gauges, we present approach for identifying the second micropolar material parameter – the coupling number. An inverse numerical analysis has been conducted on homogenised models of specimens (modelled without voids), discretised by the developed micropolar finite elements where the coupling number is determined based on the obtained numerical displacement values.
- (b) In Chapter 6, the laboratory uniaxial tensile tests on three types of aluminium strips (PH specimens) with central circular hole have been performed to analyse stress concentration at the edge of the hole and the strain profile across the cross-section cut through the middle of the hole. Strain gauges and the 3D contactless optical measuring GOM system have been used for measuring strains and displacements, respectively. For the purpose of seeking an answer to our fundamental question which states: “*Can the classical theory of elasticity sufficiently well describe the considered problem?*”, we compare the obtained experimental results with analytical and numerical solutions. Furthermore, we examine whether the

micropolar theory can provide a more suitable model and we suggest a methodology based on parametric and inverse numerical analysis for the identification of the micropolar parameters present in the problem (coupling number and characteristic length for bending).

Chapter 2

Micropolar theory of elasticity

”Men pass away, but their deeds abide.”

The last words of Augustin-Louis Cauchy (1857.)

In this Chapter, the fundamental laws and theorems of a three-dimensional linear elastic micropolar continuum are presented, leading to the stress and couple-stress tensor fields. Equations of motion, kinematic and constitutive equations are then derived in a form applicable to linear analysis. The three-dimensional formulation is then reduced to two special cases of the two-dimensional formulation: plane stress and plane strain, which will be the focus of the experimental investigation in this thesis.

2.1 Generalised Cauchy’s stress theorem

It is generally considered [9, 72] that a solid body consists of small material particles (molecules) between which exists a balanced system of intermolecular (internal) forces that prevent the body from being deformed when no external force acts upon it. As a result of the action of external loading, the body will deform, causing the repositions of molecules which lead to a change in the distances between the particles, and the internal forces. The process of deformation of the body will persist until the establishment of the equilibrium between external and internal forces [72]. In other words, if the body is in equilibrium, the internal and external forces will have the same magnitude but different directions. In continuum mechanics, forces can be divided into two fundamental categories: volume and surface forces. Volume (body) forces are distributed to each material particle within the entire volume of the body (e.g., internal intermolecular forces,

gravitational force or electromagnetic force). On the other hand, forces acting on the surface of the body are e.g., contact forces between two bodies, atmospheric pressure or other types of external forces distributed over the body surface. If we observe a part of a body with a surface on which forces occur due to the interaction between this part of the body and its remainder, these forces are also surface forces.

Let us now consider a body \mathfrak{B} composed of continuous matter occupying the volume V , which is bounded by the surface S in 3D Euclidean space with an orthonormal unit basis \mathbf{e}_i for $i = 1, 2, 3$. Let us focus on an arbitrarily chosen material particle within the body \mathfrak{B} , denoted as X . The position of particle X is defined by the initial position vector \mathbf{r}_o with respect to the origin O of the Cartesian coordinate system (x_1, x_2, x_3) at the initial time t_0 when no external force is acting on the body. If the body is subjected to a system of external forces consisting of specific body (volume) force \mathbf{p}_v and moment \mathbf{m}_v , as well as a specific surface force \mathbf{p}_s and moment \mathbf{m}_s , the body deforms. The current position of the material point X is then defined by the position vector \mathbf{r} at time t , representing the current (deformed) configuration (see Fig. 2.1).

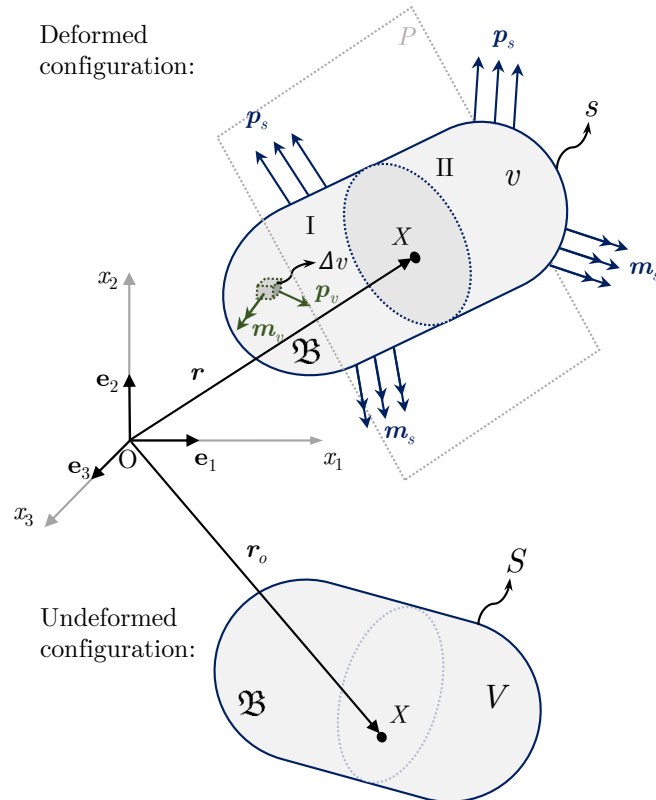


Figure 2.1: Initial (undeformed) and deformed configuration of the continuous body.

Let us imagine now that the deformed body, under equilibrium, is cut into two parts (I and

II) by an arbitrary flat plane P passing through the point X . If we remove part II, the remaining part I must remain in equilibrium. To achieve this, an appropriate system of internal forces must appear on the plane. The resultant of the internal forces and the moment of part I, caused by part II for the observed plane, is denoted by \mathbf{F} and \mathbf{M} , respectively. Only a portion of the internal forces acts on an arbitrarily small part of the surface Δs defined by a unit normal vector \mathbf{n} , resulting in a force vector $\Delta \mathbf{F}$ and an additional couple vector $\Delta \mathbf{M}$ as shown in Fig. 2.2.

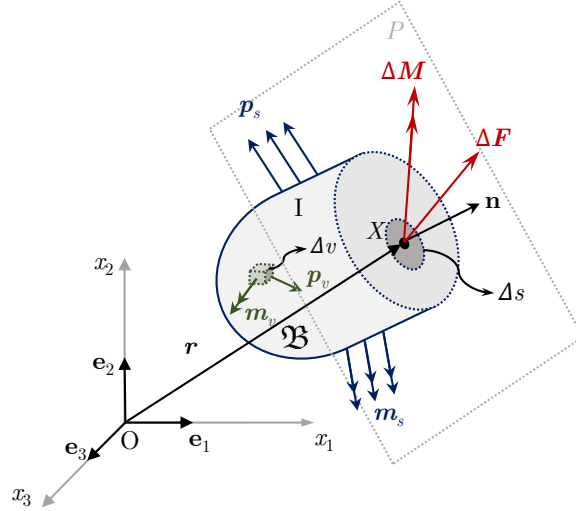


Figure 2.2: Internal forces and moments acting on a small surface of part I of the observed body under the action of an external load.

The ratio between the force vector $\Delta \mathbf{F}$, and the couple vector $\Delta \mathbf{M}$ and the surface Δs represents a mean stress vector $\tilde{\mathbf{t}}$ and a mean couple-stress vector $\tilde{\mathbf{m}}$, respectively, as

$$\tilde{\mathbf{t}} = \frac{\Delta \mathbf{F}}{\Delta s}, \quad \tilde{\mathbf{m}} = \frac{\Delta \mathbf{M}}{\Delta s}. \quad (2.1)$$

In order to describe the state of stress in the material particle X , according to Cauchy's principle we can imagine that a surface around the considering point Δs is converging to a an infinitesimally small surface ds (limiting process) [73] defining the stress vector at X as

$$\mathbf{t}(\mathbf{r}, t, \mathbf{n}) = \lim_{\Delta s \rightarrow 0} \tilde{\mathbf{t}} = \frac{d\mathbf{F}}{ds}. \quad (2.2)$$

The stress vector field $\mathbf{t}(\mathbf{r}, t, \mathbf{n})$ depends on the position vector \mathbf{r} in time t , and the unit normal vector \mathbf{n} (directed outward) of the small surface element ds .

According to Cauchy's (or classical) theory of elasticity, the interaction between two material particles is described only by force vector. In other words, this means that no distributed

volume \mathbf{m}_v or surface moments \mathbf{m}_s can be applied in classical theory, that is, a moment can only be defined as the product of force and moment arm around a certain point. Therefore, the response of a body under the action of external forces is described by a stress and strain tensor, both of which symmetric as a consequence of moment equilibrium and stored elastic energy. Consequently, at the surface defined by the plane dividing the body into two arbitrary parts, there is a surface force loading caused by a removed part of the body, which results in a stress vector \mathbf{t} (with normal and tangential components). This surface load on an arbitrarily small part of the surface Δs has a resultant force vector $\Delta \mathbf{F}$, and a moment vector ΔM around the material point X . However, if we consider an infinitesimally small surface $\Delta s \rightarrow 0$, then the moment arm also tends to zero, which defines the couple-stress vector at point X as

$$\lim_{\Delta s \rightarrow 0} \tilde{\mathbf{m}} = \mathbf{0}. \quad (2.3)$$

In the micropolar continuum theory, that takes into account the microstructural effects, the interaction between neighbouring particles additionally depends on their rotations, which can lead to additional surface moments. Thus, on the considered surface Δs , there exist both, a surface force load and a surface moment load. If we now consider an infinitesimal surface ds around the material point X after the limiting process, there also exists a couple-stress vector field at X as

$$\mathbf{m}(\mathbf{r}, t, \mathbf{n}) = \lim_{\Delta s \rightarrow 0} \tilde{\mathbf{m}} = \frac{d\mathbf{M}}{ds}. \quad (2.4)$$

For different orientation of the surface element Δs with the corresponding normal vector, the associated stress and couple-stress vectors at a point under consideration also vary. In order to prove the existence of stress tensor and couple-stress tensor, we start here from the fundamental laws and axioms of continuum mechanics.

Law of Conservation of Mass

*The mass within the system remains **constant** and it cannot be created or "wiped out" as time progresses, regardless of the shape or configuration of the body.*

The total mass of the body \mathfrak{B} , which fills the volume v in space at the time t , is obtained as

follows

$$m_{\mathfrak{B}} = \int_v \rho(\mathbf{r}, t) dv, \quad (2.5)$$

where the scalar field $\rho(\mathbf{r}, t)$ represents the mass density over the body in the deformed state. Considering that the mass is independent of the configuration of the body, we have

$$\int_v \rho(\mathbf{r}, t) dv = \int_V \rho_0(\mathbf{r}_o) dV, \quad (2.6)$$

where ρ_0 is the mass density of the body in the reference configuration. Since the mass of the body, as well as the mass of an arbitrary part of the body, is conserved during motion, the change in mass over time must be equal to zero [9]

$$\frac{d}{dt}(\rho dv) = 0, \quad (2.7)$$

Balance of Linear Momentum

The change in linear momentum \mathbf{L} of a body or any part of that body during the time t is equal to the vectorial sum of all external forces \mathbf{F} acting on that body, or on the considered part of the body including the internal forces resulting from the interactions between the particles within the body.

According to the Newton's second law it follows

$$\frac{d\mathbf{L}}{dt} = \mathbf{F}, \quad (2.8)$$

which can be applied for the body \mathfrak{B} of a volume v bounded by a surface s , and subjected to the external specific surface force \mathbf{p}_s and volume force \mathbf{p}_v as follows

$$\frac{d}{dt} \int_v (\rho \dot{\mathbf{r}}) dv = \int_v [\mathbf{p}_v(\mathbf{r}, t)] dv + \int_s [\mathbf{p}_s(\mathbf{r}, t, \mathbf{n})] ds. \quad (2.9)$$

Similarly, we can write the equation of momentum balance for an arbitrary part i of the body \mathfrak{B} of a volume v_i surrounded by a surface s_i where we have the additional surface forces that occur

due to the interaction between this part of the body and its remainder, and thus, we can write

$$\frac{d}{dt} \int_{v_i} (\rho \dot{\mathbf{r}}) dv = \int_{v_i} [\mathbf{p}_v(\mathbf{r}, t)] dv + \int_{s_i} [\mathbf{t}(\mathbf{r}, t, \mathbf{n})] ds, \quad (2.10)$$

Taking into account the law of conservation of mass, that is, $\frac{d}{dt}(\rho dv) = 0$, we can write

$$\int_{v_i} (\rho \ddot{\mathbf{r}}) dv = \int_{v_i} [\mathbf{p}_v(\mathbf{r}, t)] dv + \int_{s_i} [\mathbf{t}(\mathbf{r}, t, \mathbf{n})] ds, \quad (2.11)$$

where superimposed dot ($\dot{\bullet}$) and double dot ($\ddot{\bullet}$) represent differentiations over the time, i.e., the velocity and acceleration.

Balance of Angular Momentum

The change in the angular momentum (moment of momentum) of a body or any part of that body with respect to the reference point O during the time t is equal to the vectorial sum of all the moments acting on the body, or on the observed part of the body including the surface moments which arise within the body due to the interaction between the part of the body and its rest.

Here, we can note that the formulation of the balance of linear momentum is the same as in the Cauchy's continuum theory. However, the formulation for the balance of angular momentum in the micropolar continuum differs from the classical one because it contains additional term associated with the microinertia of a material particle, as well as the distributed body \mathbf{m}_v and surface couples \mathbf{m}_s . The balance of angular momentum for the whole body follows as

$$\frac{d}{dt} \int_v (\mathbf{r} \times \dot{\mathbf{r}} \rho + \mathbf{J} \dot{\boldsymbol{\phi}}) dv = \int_v [\mathbf{r} \times \mathbf{p}_v(\mathbf{r}, t) + \mathbf{m}_v(\mathbf{r}, t)] dv + \int_s [\mathbf{r} \times \mathbf{p}_s(\mathbf{r}, t, \mathbf{n}) + \mathbf{m}_s(\mathbf{r}, t, \mathbf{n})] ds, \quad (2.12)$$

while for an arbitrary part of the body is [23]

$$\frac{d}{dt} \int_{v_i} (\mathbf{r} \times \dot{\mathbf{r}} \rho + \mathbf{J} \dot{\boldsymbol{\phi}}) dv = \int_{v_i} [\mathbf{r} \times \mathbf{p}_v(\mathbf{r}, t) + \mathbf{m}_v(\mathbf{r}, t)] dv + \int_{s_i} [\mathbf{r} \times \mathbf{t}(\mathbf{r}, t, \mathbf{n}) + \mathbf{m}(\mathbf{r}, t, \mathbf{n})] ds, \quad (2.13)$$

$$\int_{v_i} (\mathbf{r} \times \ddot{\mathbf{r}} \rho + \mathbf{J} \ddot{\boldsymbol{\phi}}) dv = \int_{v_i} [\mathbf{r} \times \mathbf{p}_v(\mathbf{r}, t) + \mathbf{m}_v(\mathbf{r}, t)] dv + \int_{s_i} [\mathbf{r} \times \mathbf{t}(\mathbf{r}, t, \mathbf{n}) + \mathbf{m}(\mathbf{r}, t, \mathbf{n})] ds. \quad (2.14)$$

where $\boldsymbol{\phi}$ is a microrotation vector that arises as a consequence of considering the microstructure of the material in micropolar theory. This additional degree of freedom gives each material particle an orientation and it is completely independent of the skew-symmetric part of the displacement

gradient at the observed point (macrorotation) [3]. Since there is a microrotation vector, a second-order tensor of a material microinertia density \mathbf{J} also occurs which refers to the resistance of the particles inside the material to changes in its rotational motion. It was first introduced by Eringen in [74], where he also derived the conservation law for the microinertia density tensor. Generally speaking, the microinertia density is a tensor, but if we consider a special case of a linear micropolar elasticity where particles have a spherical shape (as we do in this thesis for simplicity), tensor \mathbf{J} becomes a diagonal tensor with components ρj , that is, $\mathbf{J} = \rho j \mathbf{I}$, where \mathbf{I} stands for a diagonal identity matrix, and j represents a microinertia coefficient that depends on the internal structure of a material and it is necessary to determine it experimentally for each material. In other words, the microinertia density tensor becomes the identity tensor multiplied by a scalar.

Cauchy's Fundamental Lemma

The stress vectors acting on both opposite sides of a material area through any particle in the body have equal magnitude but opposite direction [73]

$$\mathbf{t}(\mathbf{r}, \mathbf{n}) = -\mathbf{t}(\mathbf{r}, -\mathbf{n}). \quad (2.15)$$

To generalise this Lemma to the micropolar continuum, we start from its *proof*.

Let us consider now an arbitrary part of the deformed body \mathfrak{B} , defined by the surface s' enclosing the volume v' . The volume v' contains a material particle X through which passes an arbitrary plane P that divides the body (and the observed part of the body) into two volumes v_1 and v_2 bounded by the surfaces s_1 and s_2 respectively, where both parts share a common surface Δs (see Fig. 2.3). The surfaces s_1 and s_2 are defined by unit normal vectors \mathbf{n}_1 and \mathbf{n}_2 , respectively. The balance of the linear momentum of the entire volume $v' = v_1 + v_2$ is

$$\int_{v'} (\rho \ddot{\mathbf{r}}) dv = \int_{v'} [\mathbf{p}_v(\mathbf{r}, t)] dv + \int_{s'} [\mathbf{t}(\mathbf{r}, t, \mathbf{n})] ds, \quad (2.16)$$

while applying this first law of motion to v_1 , we have

$$\int_{v_1} (\rho \ddot{\mathbf{r}}) dv = \int_{v_1} [\mathbf{p}_v(\mathbf{r}, t)] dv + \int_{s_1} [\mathbf{t}(\mathbf{r}, t, \mathbf{n})] ds + \int_{\Delta s} [\mathbf{t}(\mathbf{r}, t, \mathbf{n}_1)] ds. \quad (2.17)$$

Similarly, for part v_2 we get

$$\int_{v_2} (\rho \ddot{\mathbf{r}}) dv = \int_{v_2} [\mathbf{p}_v(\mathbf{r}, t)] dv + \int_{s_2} [\mathbf{t}(\mathbf{r}, t, \mathbf{n})] ds + \int_{\Delta s} [\mathbf{t}(\mathbf{r}, t, \mathbf{n}_2)] ds. \quad (2.18)$$

and subtracting equations (2.17), (2.18) from (2.16) for whole observed part of the body v' we obtain

$$\mathbf{0} = \int_{\Delta s} [\mathbf{t}(\mathbf{r}, t, \mathbf{n}_1) + \mathbf{t}(\mathbf{r}, t, \mathbf{n}_2)] ds. \quad (2.19)$$

For $\lim_{\Delta s \rightarrow 0}$ we get

$$\mathbf{t}(\mathbf{r}, t, \mathbf{n}_1) + \mathbf{t}(\mathbf{r}, t, \mathbf{n}_2) = \mathbf{0}, \quad (2.20)$$

and considering that $\mathbf{n}_1 = -\mathbf{n}_2$, there follows equality (2.15), which proves Cauchy's Fundamental Lemma [7].

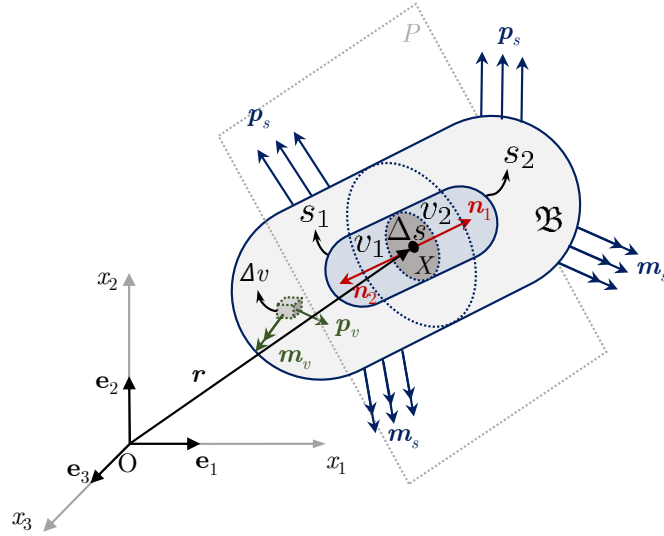


Figure 2.3: Arbitrary part of the body.

In a similar way, the lemma can be generalised for the couple-stress vector, where the balance of angular momentum can be applied to the arbitrary part of the body of volume v'

$$\int_{v'} (\mathbf{r} \times \rho \ddot{\mathbf{r}} + \mathbf{J} \ddot{\phi}) dv = \int_{v'} [\mathbf{r} \times \mathbf{p}_v(\mathbf{r}, t) + \mathbf{m}_v(\mathbf{r}, t)] dv + \int_{s'} [\mathbf{r} \times \mathbf{t}(\mathbf{r}, t, \mathbf{n}) + \mathbf{m}(\mathbf{r}, t, \mathbf{n})] ds, \quad (2.21)$$

and its two parts v_1 and v_2 , whose expressions are subtracted from (2.21) from to get

$$\mathbf{0} = \int_{\Delta s} \{ \mathbf{r} \times [\mathbf{t}(\mathbf{r}, t, \mathbf{n}_1) + \mathbf{t}(\mathbf{r}, t, \mathbf{n}_2)] + \mathbf{m}(\mathbf{r}, t, \mathbf{n}_1) + \mathbf{m}(\mathbf{r}, t, \mathbf{n}_2) \} ds, \quad (2.22)$$

and using (2.15), as well as $\mathbf{n}_2 = -\mathbf{n}_1$ we can eventually prove that for the couple-stress vector there follows

$$\mathbf{m}(\mathbf{r}, \mathbf{n}) = -\mathbf{m}(\mathbf{r}, -\mathbf{n}). \quad (2.23)$$

Cauchy's Theorem

If a continuous stress vector field exists within the continuum, that describes the stress distribution acting at each point on a surface and depends linearly on a unit vector normal \mathbf{n} of a surface, there also exists a second-order stress tensor that is independent of \mathbf{n} , such that [75]

$$\mathbf{t}(\mathbf{r}, t, \mathbf{n}) = \boldsymbol{\sigma}(\mathbf{r}, t)\mathbf{n}. \quad (2.24)$$

In order to prove the existence of a stress tensor $\boldsymbol{\sigma}(\mathbf{r}, t)$ that completely defines the state of stresses at a certain point, we can begin by considering a tetrahedral element in a continuum.

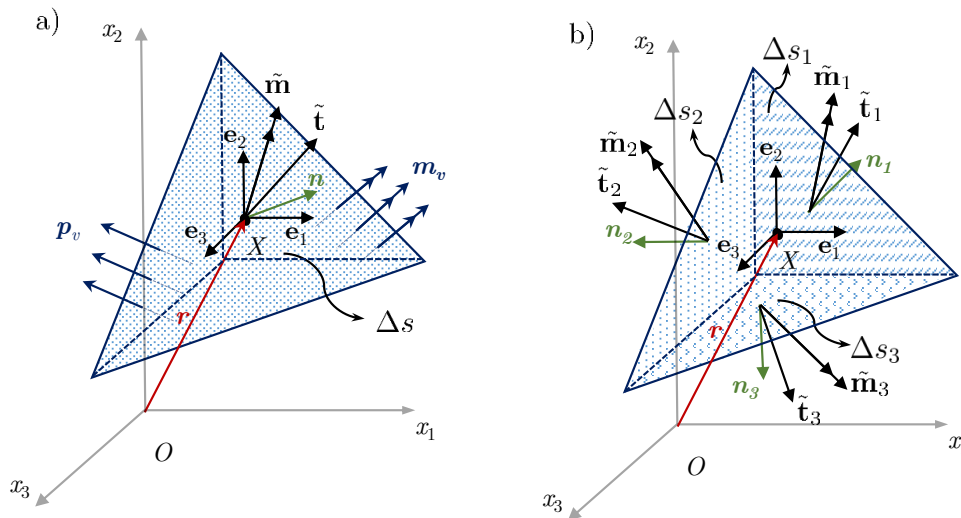


Figure 2.4: Tetrahedral element in continuum media with the mean stress and couple stress vectors on a slanted surface (left) and on surfaces with the normals parallel to the coordinate axes (right).

This tetrahedron surrounds the particle X with local orthogonal unit base vectors \mathbf{e}_i , and has three edges which are parallel with both, the base vectors \mathbf{e}_i and the Cartesian coordinate axes x_i for $i = 1, 2, 3$. The slanted face (the base) of the tetrahedron has a surface Δs with an outward

normal vector $\mathbf{n} = [n_1 \ n_2 \ n_3]^T$, while the surfaces of the remaining sides are denoted by Δs_i with the corresponding normals \mathbf{n}_i , respectively for each side (see Fig. 2.4). The tetrahedron is subjected to the volume loads \mathbf{p}_v and \mathbf{m}_v , and on each surface there are the mean stress vectors $\tilde{\mathbf{t}}$, $\tilde{\mathbf{t}}_i$ and the mean couple-stress vectors $\tilde{\mathbf{m}}$, $\tilde{\mathbf{m}}_i$. The linear momentum balance of the tetrahedron of volume $\Delta v = \frac{1}{3}h\Delta s$, where h represents the height of the tetrahedron, can be written as

$$\int_{\Delta v} [\rho\ddot{\mathbf{r}} - \mathbf{p}_v(\mathbf{r}, t)]dv = \tilde{\mathbf{t}}\Delta s + \tilde{\mathbf{t}}_1\Delta s_1 + \tilde{\mathbf{t}}_2\Delta s_2 + \tilde{\mathbf{t}}_3\Delta s_3, \quad (2.25)$$

and if we take into consideration that the areas of the sideward surfaces can be expressed as

$$\Delta s_i = (\mathbf{n}^T \mathbf{e}_i)\Delta s = n_i\Delta s, \quad (2.26)$$

we obtain

$$\int_{\Delta v} [\rho\ddot{\mathbf{r}} - \mathbf{p}_v(\mathbf{r}, t)]dv = \tilde{\mathbf{t}}\Delta s + \sum_{i=1}^3 \tilde{\mathbf{t}}_i n_i \Delta s. \quad (2.27)$$

As the tetrahedron shrinks to the considered particle X , its volume tends to zero as $\lim_{\Delta v \rightarrow 0}$, and thus becomes a third-order differential, that is negligible in comparison when its surface approaches zero as $\lim_{\Delta s \rightarrow 0}$ (which is a second-order differential). Therefore, for $\lim_{\Delta v \rightarrow 0}$ and $\lim_{\Delta s \rightarrow 0}$, we can write

$$\mathbf{0} = \mathbf{t}(\mathbf{r}, \mathbf{n})\Delta s + \sum_{i=1}^3 \mathbf{t}(\mathbf{r}, \mathbf{n})n_i\Delta s. \quad (2.28)$$

After dividing equation (2.28) by Δs , taking into account Cauchy's Lemma (2.15), and that the surface normal vectors are $\mathbf{n}_i = -\mathbf{e}_i$, we get

$$\mathbf{t}(\mathbf{r}, \mathbf{n}) = - \sum_{i=1}^3 \mathbf{t}(\mathbf{r}, -\mathbf{e}_i)n_i, \quad (2.29)$$

$$\mathbf{t}(\mathbf{r}, \mathbf{n}) = \sum_{i=1}^3 \mathbf{t}(\mathbf{r}, \mathbf{e}_i)n_i, \quad (2.30)$$

where n_i can be substituted as in (2.26)

$$\mathbf{t}(\mathbf{r}, \mathbf{n}) = \sum_{i=1}^3 \mathbf{t}(\mathbf{r}, \mathbf{e}_i) (\mathbf{e}_i^T \mathbf{n}), \quad (2.31)$$

$$\mathbf{t}(\mathbf{r}, \mathbf{n}) = \sum_{i=1}^3 \underbrace{\mathbf{t}(\mathbf{r}, \mathbf{e}_i) \mathbf{e}_i^T}_{\boldsymbol{\sigma}(\mathbf{r})} \mathbf{n}, \quad (2.32)$$

which finally leads us to the Cauchy's theorem

$$\mathbf{t}(\mathbf{r}, t, \mathbf{n}) = \boldsymbol{\sigma}(\mathbf{r}, t) \mathbf{n} \quad (2.33)$$

proving existence of the stress tensor field $\boldsymbol{\sigma}(\mathbf{r}, t)$, which is independent of the normal \mathbf{n} and reads

$$\boldsymbol{\sigma} = \sigma_{ij} \mathbf{e}_i \mathbf{e}_j^T \quad (2.34)$$

where σ_{ij} represents the component of the second-order stress tensor. Its matrix representation is

$$[\sigma_{ij}] = \begin{bmatrix} \sigma_{11} & \sigma_{12} & \sigma_{13} \\ \sigma_{21} & \sigma_{22} & \sigma_{23} \\ \sigma_{31} & \sigma_{32} & \sigma_{33} \end{bmatrix}, \quad (2.35)$$

where the first index indicates the direction of the stress components, while the second index represents their surface normal, with respect to the coordinate base. The stress components σ_{ij} for $i = j$ represent normal stresses, while those with $i \neq j$ are shear stresses.

Note: To simplify notations in this thesis, the scalar (dot) product between two vectors (\mathbf{a} , \mathbf{b}) or two second-order tensors (\mathbf{A} , \mathbf{B}) or between a vector and a tensor, is represented as a matrix multiplication, as follows: $\mathbf{a} \cdot \mathbf{b} = \mathbf{a}^T \mathbf{b}$, $\mathbf{A} \cdot \mathbf{B} = \mathbf{AB}$, $\mathbf{a} \cdot \mathbf{B} = \mathbf{a}^T \mathbf{B}$ and $\mathbf{A} \cdot \mathbf{b} = \mathbf{Ab}$.

Since the interaction between two neighbouring points in a micropolar continuum is described not only by the stress vector but also by the additional couple-stress vector, we introduce an additional couple-stress tensor by generalising the Cauchy's theorem. Let us therefore apply the balance of angular momentum (2.14) to the observed tetrahedral element, where now on each surface Δs , Δs_i , along with the mean stress vectors $\tilde{\mathbf{t}}$, $\tilde{\mathbf{t}}_i$, there are also mean couple-stress

vectors $\tilde{\mathbf{m}}, \tilde{\mathbf{m}}_i$ (see Fig. 2.4) as

$$\begin{aligned} \int_{\Delta v} (\mathbf{r} \times \ddot{\mathbf{r}}\rho + \mathbf{J}\ddot{\boldsymbol{\phi}})dv &= \int_{\Delta v} [\mathbf{r} \times \mathbf{p}_v(\mathbf{r}, t) + \mathbf{m}_v(\mathbf{r}, t)]dv + \int_{\Delta s} [\mathbf{r} \times \mathbf{t}(\mathbf{r}, t, \mathbf{n})]ds \\ &+ \tilde{\mathbf{m}}\Delta s + \tilde{\mathbf{m}}_1\Delta s_1 + \tilde{\mathbf{m}}_2\Delta s_2 + \tilde{\mathbf{m}}_3\Delta s_3. \end{aligned} \quad (2.36)$$

According to the Cauchy's stress theorem, we can replace the stress vector field with $\mathbf{t}(\mathbf{r}, t, \mathbf{n}) = \boldsymbol{\sigma}(\mathbf{r}, t)\mathbf{n}$ and rewrite the equation (2.36) as

$$\begin{aligned} \int_{\Delta v} (\hat{\mathbf{r}}\ddot{\mathbf{r}}\rho + \mathbf{J}\ddot{\boldsymbol{\phi}})dv &= \int_{\Delta v} [\hat{\mathbf{r}}\mathbf{p}_v(\mathbf{r}, t) + \mathbf{m}_v(\mathbf{r}, t)]dv \\ &+ \int_{\Delta s} [\hat{\mathbf{r}}\boldsymbol{\sigma}(\mathbf{r}, t)\mathbf{n}]ds + \tilde{\mathbf{m}}\Delta s + \sum_{i=1}^3 \tilde{\mathbf{m}}_i\Delta s_i. \end{aligned} \quad (2.37)$$

where $\hat{\mathbf{r}}$ is the skew-symmetric matrix

$$\hat{\mathbf{r}} = \begin{bmatrix} 0 & -r_{x3} & r_{x2} \\ r_{x3} & 0 & -r_{x1} \\ -r_{x2} & r_{x1} & 0 \end{bmatrix} \quad (2.38)$$

which replaces the cross product " \times " in general way $\mathbf{a} \times \mathbf{b} = \hat{\mathbf{a}}\mathbf{b}, \forall \mathbf{a}, \mathbf{b} \in \mathbb{R}^3$. For further manipulation of equation (2.37), we need to introduce the divergence theorem for 3D space, which states that the flux of a 3D vector field \mathbf{f} through a closed surface S with an outward normal \mathbf{n} is equal to the divergence of this vector field over the volume V bounded by the surface S [76]

$$\int_V (\text{div } \mathbf{f})dV = \oint_S (\mathbf{f}\mathbf{n})dS. \quad (2.39)$$

The divergence of the vector field is computed as $\text{div } \mathbf{f} = \nabla\mathbf{f}$, where ∇ is a vector of partial derivatives with respect to all coordinate axes [77]. This theorem can be generalised to the second-order tensor \mathbf{T} as follows

$$\int_V (\text{div } \mathbf{T})dV = \oint_S (\mathbf{T}\mathbf{n})dS. \quad (2.40)$$

In [42], it has been established that the divergence of a tensor is not a uniquely defined operator; that is, it can be expressed as $\nabla^T\mathbf{T} = \frac{\partial T_{pj}}{\partial x_p}\mathbf{e}_j$ or $\mathbf{T}\nabla = \frac{\partial T_{ip}}{\partial x_p}\mathbf{e}_i$, therefore, special attention should

be paid to this. The equation (2.37) can be written as

$$\int_{\Delta v} (\hat{\mathbf{r}}\ddot{\rho} + \mathbf{J}\ddot{\phi} - \hat{\mathbf{r}}\mathbf{p}_v(\mathbf{r}, t) - \mathbf{m}_v(\mathbf{r}, t) - \text{div}(\hat{\mathbf{r}}\boldsymbol{\sigma}(\mathbf{r}, t)))dv = \tilde{\mathbf{m}}\Delta s + \sum_{i=1}^3 \tilde{\mathbf{m}}_i\Delta s_i. \quad (2.41)$$

after applying the divergence theorem. Similarly as before, we consider a situation when the tetrahedral element shrinks to a material particle X , reducing the left-hand side of (2.41) to a third-order differential and the right-hand side of (2.41) to a second-order differential, i.e.,

$$\mathbf{0} = \mathbf{m}(\mathbf{r}, \mathbf{n})\Delta s + \sum_{i=1}^3 \mathbf{m}(\mathbf{r}, \mathbf{n})n_i\Delta s. \quad (2.42)$$

After dividing by Δs , taking into account generalised Cauchy's Lemma (2.23), and that the surface normal vectors are $\mathbf{n}_i = -\mathbf{e}_i$, we obtain

$$\mathbf{m}(\mathbf{r}, \mathbf{n}) = -\sum_{i=1}^3 \mathbf{m}(\mathbf{r}, -\mathbf{e}_i)n_i, \quad (2.43)$$

$$\mathbf{m}(\mathbf{r}, \mathbf{n}) = \sum_{i=1}^3 \underbrace{\mathbf{m}(\mathbf{r}, \mathbf{e}_i)\mathbf{e}_i^T}_{\boldsymbol{\mu}(\mathbf{r})} \mathbf{n}_i. \quad (2.44)$$

This bring us to the generalised Cauchy's theorem [7]

$$\mathbf{m}(\mathbf{r}, t, \mathbf{n}) = \boldsymbol{\mu}(\mathbf{r}, t)\mathbf{n}, \quad (2.45)$$

proving existence of the couple-stress tensor field $\boldsymbol{\mu}(\mathbf{r}, t)$, which is independent of the normal \mathbf{n} and reads

$$\boldsymbol{\mu} = \mu_{ij}\mathbf{e}_i\mathbf{e}_j^T \quad (2.46)$$

where μ_{ij} represents the components of the second-order couple-stress tensor. Its matrix form is

$$[\mu_{ij}] = \begin{bmatrix} \mu_{11} & \mu_{12} & \mu_{13} \\ \mu_{21} & \mu_{22} & \mu_{23} \\ \mu_{31} & \mu_{32} & \mu_{33} \end{bmatrix}, \quad (2.47)$$

where the first index indicates the direction of action (axis around which a couple-stress acts), while the second index represents the normal of the plane of action, with respect to the coordinate

base. The couple-stress components μ_{ij} for $i = j$ are the torsion couple-stresses, while for $i \neq j$ they are the bending couple-stresses.

In classical theory, the stress tensor $\boldsymbol{\sigma}$ is always symmetric, but in micropolar theory both the stress tensor $\boldsymbol{\sigma}$ and the couple-stress tensor $\boldsymbol{\mu}$ are generally non-symmetric, due to the action of the moment loads \mathbf{m}_v and \mathbf{m}_s , and the existence of the divergence of the couple-stress tensor $\text{div } \boldsymbol{\mu}$. In a situation where $\mu_{ij} = 0$, $m_{vi} = 0$ and $m_{si} = 0$, the micropolar theory reduces to the classical theory.

2.2 Equations of motion in linear analysis

In this thesis, we limit ourselves to the linear analysis, where small displacements and rotations are considered. The first set of equation of motions for micropolar continuum can be derived from the law of conservation of linear momentum, where the divergence theorem is also applied, while the second set can be analogously derived from the law of conservation of angular momentum. Using the Einstein convention on repetitive indices, the equations of motion of a micropolar (Cosserats') continuum in linear analysis with density ρ and material microinertia density $J_{ik} = \rho j \delta_{ik}$ in a rectangular spatial system with co-ordinates x_1 , x_2 and x_3 can be therefore written as [3]

$$\sigma_{ij,j} + p_{vi} = \rho \ddot{u}_i, \quad \mu_{ij,j} - \varepsilon_{ijk} \sigma_{jk} + m_{vi} = \rho j \ddot{\phi}_i, \quad (2.48)$$

where ε_{ijk} is the permutation tensor (Levi-Civita symbol) with $\varepsilon_{123} = \varepsilon_{231} = \varepsilon_{312} = 1$, $\varepsilon_{132} = \varepsilon_{321} = \varepsilon_{213} = -1$ with all other components equal to zero. The Kronecker delta symbol δ_{ij} is defined as

$$\delta_{ij} = \begin{cases} 1, & \text{if } i = j, \\ 0, & \text{otherwise.} \end{cases} \quad (2.49)$$

The comma in $\sigma_{ij,j}$ and $\mu_{ij,j}$ denotes differentiation with respect to the spatial co-ordinate x_j . The displacement and microrotation are labelled as u_i and ϕ_i , respectively, while p_{vi} and m_{vi} are the distributed volume force and moment. Since the surface is massless, the natural boundary condition remains the same as in static analysis (derived in detail in [42]), and they are valid at any point of the surface with prescribed loading as

$$\sigma_{ij} n_j = p_{si} \quad \text{and} \quad \mu_{ij} n_j = m_{si} \quad (2.50)$$

where n_i are components of the outward unit normal to the considered surface loaded by force loading p_{si} or moment loading m_{si} . On the remaining part of the boundary, we assign the kinematic boundary conditions.

2.3 Kinematic equations in linear analysis

When the influence of the microstructure of the material is taken into account, the number of degrees of freedom increases. Therefore, in the micropolar continuum theory, the difference between the initial and deformed state of the body is described by displacement field $\mathbf{u}(x_1, x_2, x_3)$, and now, with additional microrotation field $\phi(x_1, x_2, x_3)$. The microrotation attributes an orientation to each material particle and it is completely independent of the displacement field as well as its derivatives [15]. Due to the existence of an independent microrotation field ϕ there also exists a corresponding change of microrotation, i.e. a curvature (angular strain) tensor κ . The equations that establish the relationship between the strain/curvature fields and the displacement/microrotation fields are known as kinematic equations.

The kinematic equations are obtained by comparing the geometry of the initial state of a planar body on a differential level (parallelepiped) with its deformed state (geometric approach). The strain and angular strain (curvature) functions are then expanded into Taylor series, where higher-order terms are neglected. By generalising to the 3D micropolar continuum, the strain ϵ and curvature κ tensor are obtained (see [42] for a step-by-step derivation). The micropolar strain tensor ϵ is derived as

$$\begin{bmatrix} \epsilon_{11} & \epsilon_{12} & \epsilon_{13} \\ \epsilon_{21} & \epsilon_{22} & \epsilon_{23} \\ \epsilon_{31} & \epsilon_{32} & \epsilon_{33} \end{bmatrix} = \begin{bmatrix} \frac{\partial u_1}{\partial x_1} & \frac{\partial u_1}{\partial x_2} + \phi_3 & \frac{\partial u_1}{\partial x_3} - \phi_2 \\ \frac{\partial u_2}{\partial x_1} - \phi_3 & \frac{\partial u_2}{\partial x_2} & \frac{\partial u_2}{\partial x_3} + \phi_1 \\ \frac{\partial u_3}{\partial x_1} + \phi_2 & \frac{\partial u_3}{\partial x_2} - \phi_1 & \frac{\partial u_3}{\partial x_3} \end{bmatrix}, \quad (2.51)$$

which can be written in component form as

$$\epsilon_{ij} = u_{i,j} + \epsilon_{ijk}\phi_k. \quad (2.52)$$

We can observe that the normal micropolar strains are equal to those in the classical continuum theory, while the influence of the microrotation is present only in shear strains $\epsilon_{ij}, i, j = 1, 2, 3, i \neq j$. The curvature (angular strain) tensor represents the gradient of the microrotation

field

$$\begin{bmatrix} \kappa_{11} & \kappa_{12} & \kappa_{13} \\ \kappa_{21} & \kappa_{22} & \kappa_{23} \\ \kappa_{31} & \kappa_{32} & \kappa_{33} \end{bmatrix} = \begin{bmatrix} \frac{\partial \phi_1}{\partial x_1} & \frac{\partial \phi_1}{\partial x_2} & \frac{\partial \phi_1}{\partial x_3} \\ \frac{\partial \phi_2}{\partial x_1} & \frac{\partial \phi_2}{\partial x_2} & \frac{\partial \phi_2}{\partial x_3} \\ \frac{\partial \phi_3}{\partial x_1} & \frac{\partial \phi_3}{\partial x_2} & \frac{\partial \phi_3}{\partial x_3} \end{bmatrix} \quad (2.53)$$

that is

$$\kappa_{ij} = \phi_{i,j}, \quad (2.54)$$

where the first index of curvature denotes the axis around which the rotation occurs, while the second index indicates the direction of differentiation of the microrotation. The diagonal terms in curvature tensor represent torsional strains that exist only in 3D.

2.4 Constitutive equations in homogeneous and isotropic linear elasticity

In order to be able to fully determine the states of stress and strain, it is necessary to attribute certain physical properties to the deformable continuum. In other words, we should determine the relation between stresses and strains or couple-stresses and curvatures, that is achieved by constitutive equations. This set of equations describes the macroscopic behaviour of certain materials, which results from the internal constitution of the material.

If we consider an ideally elastic material in the case of small deformations, there exists a linear function between stress and strain independent of time and loading history (Hooke's law), i.e. the stress changes proportionally to the strain, and when $\sigma_{ij} = 0$, then is also $\varepsilon_{ij} = 0$. A general relationship between two second-order tensors, i.e., stress $\boldsymbol{\sigma}$ and strain $\boldsymbol{\varepsilon}$ tensors, is described by the fourth-order tensor \mathbf{C}_1 , also known as the constitutive tensor or elasticity matrix [72]. This relationship can be expressed in the Cartesian component form (generalised Hooke's law) as [78]

$$\sigma_{ij} = C_{1ijkl} \varepsilon_{kl} \quad (2.55)$$

for $i, j, k, l = 1, 2, 3$, where the total number of components C_{1ijkl} is generally 81, but in special cases (as for a homogeneous isotropic material considered here) this number of independent coefficients decreases. The components of the constitutive tensor in linear analysis remain constant, and when a material isotropy is assumed (for a material having the same physical properties in

each direction), it leads to a reduction in the number of independent elasticity constants in the constitutive tensor (in classical theory, there are only two constants) [78].

In the context of this thesis we only investigate linear-elastic isotropic centro-symmetric micropolar material, where we have two independent fourth-order constitutive tensors \mathbf{C}_1 and \mathbf{C}_2 that relate pair of independent, generally non-symmetric stress tensors $\boldsymbol{\sigma}$ and $\boldsymbol{\mu}$ with a pair of independent, also generally non-symmetric, strain tensors $\boldsymbol{\epsilon}$ and $\boldsymbol{\kappa}$ such that

$$\sigma_{ij} = C_{ijkl}\epsilon_{kl}, \quad (2.56)$$

$$\mu_{ij} = D_{ijkl}\kappa_{kl}. \quad (2.57)$$

The stress and strain tensors are symmetric according to the classical theory, and therefore, their constitutive law has only two independent elastic constants λ and μ [78], named after French mathematician Gabriel Lamé (Lamé constants). However, due to the asymmetry of stress and strain tensors in the micropolar theory, the constitutive tensor \mathbf{C}_1 is symmetric with three independent parameters as follows [3, 42, 79]

$$C_{1ijkl} = \lambda\delta_{ij}\delta_{kl} + \mu(\delta_{ik}\delta_{jl} + \delta_{il}\delta_{jk}) + \nu(\delta_{ik}\delta_{jl} - \delta_{il}\delta_{jk}), \quad (2.58)$$

with a new micropolar parameter ν , in addition to the classical constants. The Kronecker symbol is denoted as δ_{ij} and defined in (2.49), and substituting the expression of the constitutive tensor \mathbf{C}_1 (2.58) into (2.56), we can write a first set of constitutive equations as

$$\sigma_{11} = (\lambda + 2\mu)\epsilon_{11} + \lambda(\epsilon_{22} + \epsilon_{33}), \quad (2.59)$$

$$\sigma_{12} = (\mu + \nu)\epsilon_{12} + (\mu - \nu)\epsilon_{21}, \quad (2.60)$$

$$\sigma_{13} = (\mu + \nu)\epsilon_{13} + (\mu - \nu)\epsilon_{31}, \quad (2.61)$$

$$\sigma_{21} = (\mu - \nu)\epsilon_{12} + (\mu + \nu)\epsilon_{21}, \quad (2.62)$$

$$\sigma_{22} = \lambda(\epsilon_{11} + \epsilon_{33}) + (\lambda + 2\mu)\epsilon_{22}, \quad (2.63)$$

$$\sigma_{23} = (\mu + \nu)\epsilon_{23} + (\mu - \nu)\epsilon_{32}, \quad (2.64)$$

$$\sigma_{31} = (\mu - \nu)\epsilon_{13} + (\mu + \nu)\epsilon_{31}, \quad (2.65)$$

$$\sigma_{32} = (\mu - \nu)\epsilon_{23} + (\mu + \nu)\epsilon_{32}, \quad (2.66)$$

$$\sigma_{33} = \lambda(\epsilon_{11} + \epsilon_{22}) + (\lambda + 2\mu)\epsilon_{33}, \quad (2.67)$$

or consolidated as

$$\sigma_{ij} = \lambda \epsilon_{kk} \delta_{ij} + (\mu + \nu) \epsilon_{ij} + (\mu - \nu) \epsilon_{ji}. \quad (2.68)$$

It can be observed that the normal stress components remain the same as in the classical theory, while the shear stresses are non-symmetric and differ for the micropolar theory. This constitutive relationship may be written in a matrix form like

$$\left\{ \begin{array}{c} \sigma_{11} \\ \sigma_{12} \\ \sigma_{13} \\ \sigma_{21} \\ \sigma_{22} \\ \sigma_{23} \\ \sigma_{31} \\ \sigma_{32} \\ \sigma_{33} \end{array} \right\} = \underbrace{\left[\begin{array}{cccccccccc} (\lambda + 2\mu) & 0 & 0 & 0 & \lambda & 0 & 0 & 0 & \lambda & \\ 0 & (\mu + \nu) & 0 & (\mu - \nu) & 0 & 0 & 0 & 0 & 0 & \\ 0 & 0 & (\mu + \nu) & 0 & 0 & 0 & (\mu - \nu) & 0 & 0 & \\ 0 & (\mu - \nu) & 0 & (\mu + \nu) & 0 & 0 & 0 & 0 & 0 & \\ \lambda & 0 & 0 & 0 & (\lambda + 2\mu) & 0 & 0 & 0 & \lambda & \\ 0 & 0 & 0 & 0 & 0 & (\mu + \nu) & 0 & (\mu - \nu) & 0 & \\ 0 & 0 & (\mu - \nu) & 0 & 0 & 0 & (\mu + \nu) & 0 & 0 & \\ 0 & 0 & 0 & 0 & 0 & (\mu - \nu) & 0 & (\mu + \nu) & 0 & \\ \lambda & 0 & 0 & 0 & \lambda & 0 & 0 & 0 & (\lambda + 2\mu) & \end{array} \right]}_{\mathbf{C}_1} \left\{ \begin{array}{c} \epsilon_{11} \\ \epsilon_{12} \\ \epsilon_{13} \\ \epsilon_{21} \\ \epsilon_{22} \\ \epsilon_{23} \\ \epsilon_{31} \\ \epsilon_{32} \\ \epsilon_{33} \end{array} \right\}. \quad (2.69)$$

The second symmetric constitutive tensor \mathbf{C}_2 , which relates the couple-stress tensor and the curvature tensor (2.57), has additional three micropolar constants α , β and γ , and it is derived as [3, 42, 79]

$$C_{2ijkl} = \alpha \delta_{ij} \delta_{kl} + \beta (\delta_{ik} \delta_{jl} + \delta_{il} \delta_{jk}) + \gamma (\delta_{ik} \delta_{jl} - \delta_{il} \delta_{jk}). \quad (2.70)$$

By substituting (2.70) into (2.57) we obtain the second set of constitutive equations as

$$\mu_{11} = (\alpha + 2\beta)\kappa_{11} + \alpha(\kappa_{22} + \kappa_{33}), \quad (2.71)$$

$$\mu_{12} = (\beta + \gamma)\kappa_{12} + (\beta - \gamma)\kappa_{21}, \quad (2.72)$$

$$\mu_{13} = (\beta + \gamma)\kappa_{13} + (\beta - \gamma)\kappa_{31}, \quad (2.73)$$

$$\mu_{21} = (\beta - \gamma)\kappa_{12} + (\beta + \gamma)\kappa_{21}, \quad (2.74)$$

$$\mu_{22} = \alpha(\kappa_{11} + \kappa_{33}) + (\alpha + 2\beta)\kappa_{22}, \quad (2.75)$$

$$\mu_{23} = (\beta + \gamma)\kappa_{23} + (\beta - \gamma)\kappa_{32}, \quad (2.76)$$

$$\mu_{31} = (\beta - \gamma)\kappa_{13} + (\beta + \gamma)\kappa_{31}, \quad (2.77)$$

$$\mu_{32} = (\beta - \gamma)\kappa_{23} + (\beta + \gamma)\kappa_{32}, \quad (2.78)$$

$$\mu_{33} = \alpha(\kappa_{11} + \kappa_{22}) + (\alpha + 2\beta)\kappa_{33}, \quad (2.79)$$

that is

$$\mu_{ij} = \alpha\kappa_{kk}\delta_{ij} + (\beta + \gamma)\kappa_{ij} + (\beta - \gamma)\kappa_{ji}, \quad (2.80)$$

which can be written in a matrix form as

$$\begin{Bmatrix} \mu_{11} \\ \mu_{12} \\ \mu_{13} \\ \mu_{21} \\ \mu_{22} \\ \mu_{23} \\ \mu_{31} \\ \mu_{32} \\ \mu_{33} \end{Bmatrix} = \underbrace{\begin{bmatrix} (\alpha + 2\beta) & 0 & 0 & 0 & \alpha & 0 & 0 & 0 & \alpha \\ 0 & (\beta + \gamma) & 0 & (\beta - \gamma) & 0 & 0 & 0 & 0 & 0 \\ 0 & 0 & (\beta + \gamma) & 0 & 0 & 0 & (\beta - \gamma) & 0 & 0 \\ 0 & (\beta - \gamma) & 0 & (\beta + \gamma) & 0 & 0 & 0 & 0 & 0 \\ \alpha & 0 & 0 & 0 & (\alpha + 2\beta) & 0 & 0 & 0 & \alpha \\ 0 & 0 & 0 & 0 & 0 & (\beta + \gamma) & 0 & (\beta - \gamma) & 0 \\ 0 & 0 & (\beta - \gamma) & 0 & 0 & 0 & (\beta + \gamma) & 0 & 0 \\ 0 & 0 & 0 & 0 & 0 & (\beta - \gamma) & 0 & (\beta + \gamma) & 0 \\ \alpha & 0 & 0 & 0 & \alpha & 0 & 0 & 0 & (\alpha + 2\beta) \end{bmatrix}}_{\mathbf{C}_2} \begin{Bmatrix} \kappa_{11} \\ \kappa_{12} \\ \kappa_{13} \\ \kappa_{21} \\ \kappa_{22} \\ \kappa_{23} \\ \kappa_{31} \\ \kappa_{32} \\ \kappa_{33} \end{Bmatrix}. \quad (2.81)$$

2.4.1 Micropolar material parameters

Lamé elastic constants are commonly used in the theory of elasticity, while for engineering calculations an alternative set of engineering (measurable) parameters is often more suitable as they can be easily interpreted in terms of material behaviour under different conditions. To ensure the physical meaning and stability of the material model, the limits on the values of Lamé

elastic constants are computed as [80]

$$3\lambda + 2\mu > 0, \quad \mu > 0 \quad (2.82)$$

by satisfying the positive definiteness of the constitutive tensor \mathbf{C} . In the classical theory, these two elastic constants are related to two well-known engineering parameters [73]

$$\lambda = \frac{2nG}{1-2n}, \quad \mu = G, \quad (2.83)$$

where $G = \frac{E}{2(1+n)}$ is the shear modulus, n is Poisson's ratio $n \in \langle -1, 0.5 \rangle$, while E is Young's modulus. In the micropolar theory for a linear-elastic and isotropic material, we have additional four elastic constants α , β , γ and ν , whose limits are also defined by satisfying positive definiteness of \mathbf{C}_1 and \mathbf{C}_2 , and follow as [60]

$$\nu > 0, \quad 3\alpha + 2\beta > 0, \quad \beta > 0, \quad \gamma > 0. \quad (2.84)$$

These elastic constants are related to a new set of engineering parameters in the following way [42, 81]

$$\nu = \frac{GN^2}{1-N^2}, \quad \alpha = \frac{2Gl_t^2(1-\Psi)}{\Psi}, \quad \beta = Gl_t^2, \quad \gamma = G(4l_b^2 - l_t^2). \quad (2.85)$$

where $N \in \langle 0, 1 \rangle$ is a dimensionless coupling number that is a measure of the degree of coupling between the microrotation and the macrorotation vector (skew-symmetric components of the displacement gradient). When $N = 1$, the parameter ν tends to infinity, which is a case of the so-called couple-stress elasticity [21] while, for $N = 0$, ν tends to zero, as in the classical elasticity. The parameter $\Psi \in \langle 0, \frac{3}{2} \rangle$ is a dimensionless polar ratio of rotational sensitivity that has a similar effect in torsion as the Poisson's ratio in axial deformation. Characteristic lengths for bending l_b and for torsion l_t are the parameters, which represent a measure of the respective stiffening due to the microstructure of the material and they introduce the size-effect phenomenon into consideration. The influence of the microstructure of the material on its macroscopic behaviour becomes relatively minor when the values of the characteristic lengths are significantly smaller compared to the appropriate dimensions of the observed specimen (subjected to torsion or bending). Consequently, the material could behave as predicted by classical theory (without expecting the size-effect). For highly homogeneous metals, for example, the values of the characteristic lengths could be of the order of the atomic spacing [79].

It is very important to note that various authors have been using different notations for micropolar material parameters during the development of the micropolar theory. For example, Nowacki [10], Eringen [82], Neff [83] and Cowin [84] have utilized distinct expressions for the individual components of the constitutive tensor, and a comprehensive comparison of their notations can be found in [79]. In this thesis, the notation according to [40] has been adopted, which is inspired by [10].

2.4.2 Plane stress and plane strain formulation

The governing equations of the three-dimensional micropolar continuum can be reduced to the two dimensional formulation for its two special cases - the plane strain and the plane stress conditions. In the two dimensional case there are only three degrees of freedom, i.e. two displacements (u_1, u_2) and one in-plane (drilling) microrotation ϕ_3 . Hence, the kinematic equations are reduced to

$$\begin{pmatrix} \epsilon_{11} \\ \epsilon_{12} \\ \epsilon_{21} \\ \epsilon_{22} \end{pmatrix} = \begin{bmatrix} \frac{\partial}{\partial x_1} & 0 \\ \frac{\partial}{\partial x_2} & 0 \\ 0 & \frac{\partial}{\partial x_1} \\ 0 & \frac{\partial}{\partial x_2} \end{bmatrix} \begin{pmatrix} u_1 \\ u_2 \end{pmatrix} + \begin{pmatrix} 0 \\ 1 \\ -1 \\ 0 \end{pmatrix} \phi_3 \quad (2.86)$$

and

$$\begin{pmatrix} \kappa_{31} \\ \kappa_{32} \end{pmatrix} = \begin{pmatrix} \frac{\partial}{\partial x_1} \\ \frac{\partial}{\partial x_2} \end{pmatrix} \phi_3. \quad (2.87)$$

2.4.2.1 Plane strain

In the plane strain state it is assumed that the strain components involving the x_3 direction are equal to zero, that is $\epsilon_{33} = \epsilon_{13} = \epsilon_{23} = \epsilon_{31} = \epsilon_{32} = 0$. That gives the reduced constitutive equations as

$$\begin{pmatrix} \sigma_{11} \\ \sigma_{12} \\ \sigma_{21} \\ \sigma_{22} \end{pmatrix} = \begin{bmatrix} (\lambda + 2\mu) & 0 & 0 & \lambda \\ 0 & (\mu + \nu) & (\mu - \nu) & 0 \\ 0 & (\mu - \nu) & (\mu + \nu) & 0 \\ \lambda & 0 & 0 & (\lambda + 2\mu) \end{bmatrix} \begin{pmatrix} \epsilon_{11} \\ \epsilon_{12} \\ \epsilon_{21} \\ \epsilon_{22} \end{pmatrix} = \frac{E}{1 + n} \begin{bmatrix} \frac{1-n}{1-2n} & 0 & 0 & \frac{n}{1-2n} \\ 0 & \frac{1}{2(1-N^2)} & \frac{1-2N^2}{2(1-N^2)} & 0 \\ 0 & \frac{1-2N^2}{2(1-N^2)} & \frac{1}{2(1-N^2)} & 0 \\ \frac{n}{1-2n} & 0 & 0 & \frac{1-n}{1-2n} \end{bmatrix} \begin{pmatrix} \epsilon_{11} \\ \epsilon_{12} \\ \epsilon_{21} \\ \epsilon_{22} \end{pmatrix}. \quad (2.88)$$

It is also assumed that all microrotations around x_1 and x_2 axis are equal to zero, and therefore all curvature components around these axis are zero, as well as the derivative in the out-of-plane direction, e.i., $\kappa_{11} = \kappa_{12} = \kappa_{21} = \kappa_{22} = \kappa_{23} = \kappa_{13} = \kappa_{33} = 0$. This neglects certain micropolar effects in the x_3 direction, which leads to

$$\begin{Bmatrix} \mu_{31} \\ \mu_{32} \end{Bmatrix} = \begin{bmatrix} (\beta + \gamma) & 0 \\ 0 & (\beta + \gamma) \end{bmatrix} \begin{Bmatrix} \kappa_{31} \\ \kappa_{32} \end{Bmatrix} = \frac{2El_b^2}{1+n} \begin{bmatrix} 1 & 0 \\ 0 & 1 \end{bmatrix} \begin{Bmatrix} \kappa_{31} \\ \kappa_{32} \end{Bmatrix} \quad (2.89)$$

where elastic constant α , as well as the engineering parameters Ψ and l_t do not manifest themselves in 2D formulation because they are related to torsional deformations.

2.4.2.2 Plane stress

For the plane stress condition it is assumed that all stresses related to the x_3 direction are equal to zero, that is $\sigma_{33} = \sigma_{13} = \sigma_{23} = \epsilon_{31} = \sigma_{32} = 0$. Hence, the first set of constitutive equations is reduced as

$$\begin{Bmatrix} \sigma_{11} \\ \sigma_{12} \\ \sigma_{21} \\ \sigma_{22} \end{Bmatrix} = \begin{bmatrix} \frac{4\mu(\lambda+\mu)}{\lambda+2\mu} & 0 & 0 & \frac{2\mu\lambda}{\lambda+2\mu} \\ 0 & (\mu+\nu) & (\mu-\nu) & 0 \\ 0 & (\mu-\nu) & (\mu+\nu) & 0 \\ \frac{2\mu\lambda}{\lambda+2\mu} & 0 & 0 & \frac{4\mu(\lambda+\mu)}{\lambda+2\mu} \end{bmatrix} \begin{Bmatrix} \epsilon_{11} \\ \epsilon_{12} \\ \epsilon_{21} \\ \epsilon_{22} \end{Bmatrix} = \frac{E}{1+n} \begin{bmatrix} \frac{1}{1-n} & 0 & 0 & \frac{n}{1-n} \\ 0 & \frac{1}{2(1-N^2)} & \frac{1-2N^2}{2(1-N^2)} & 0 \\ 0 & \frac{1-2N^2}{2(1-N^2)} & \frac{1}{2(1-N^2)} & 0 \\ \frac{n}{1-n} & 0 & 0 & \frac{1}{1-n} \end{bmatrix} \begin{Bmatrix} \epsilon_{11} \\ \epsilon_{12} \\ \epsilon_{21} \\ \epsilon_{22} \end{Bmatrix}, \quad (2.90)$$

while the constitutive relationship involving curvatures and couple-stresses remains the same as for the plane strain condition.

Chapter 3

Manifestations of helicoidal interpolation and fixed-pole approach in linear elasticity

A part of the investigated relationship between linearised forms of some interpolation schemes originated from the non-linear analysis of a 3D beam with a linked interpolation presented in this Chapter is also shown in: [85] Grbac, L., Jelenić, G., Ribarić D., Grbčić Erdelj, S., "Hexahedral finite elements with enhanced fixed-pole interpolation for linear static and vibration analysis of 3D micropolar continuum" International Journal for Numerical Methods in Engineering. 2024; 125(8):e7440; as well as the newly developed enhanced fixed-pole interpolation that emerged from this study.

Analytical solutions can be obtained for a limited number of problems by solving differential equations provided by theories of elasticity (that is, equilibrium equations/equations of motion, kinematic and constitutive equations and additionally the compatibility equations that have not been explicitly derived for the micropolar continuum in Chapter 2, but whose detailed derivation can be found in [86] for the planar micropolar continuum), where the appropriate boundary conditions must be also considered alongside these equations. Therefore, many practical problems in structural analysis cannot be solved using the analytical approach, while in the micropolar theory solving differential equations becomes even more complex, and closed-form solutions are achievable only for a small number of very simple problems. For this reason, approximative

methods based on the physical discretisation of a continuous system are used in structural analysis, where these differential equations are replaced by a system of algebraic equations [87]. The finite element method (FEM) is the most commonly used numerical method in engineering analysis. Its roots are often associated with R. Courant, who provided a solution to the torsional problem for a discretised domain using a polynomial approximation in his work [88] from 1943. The practical application of FEM began in the aircraft industry during the 1950s, and significant contributions to the early development of FEM have been attributed to O. C. Zienkiewicz [89] and Y. K. Cheung [90]. Since its initial use in structural analysis, FEM has spread to other areas of solid mechanics, fluid mechanics, etc. [87]. The first commercial computer programmes based on FEM appeared in the 1970s, and since then a large number of FEM-based computer software has been developed and widely used. Some of the best-known programmes for structural analysis are Autodesk Robot, Tower Radimpex and STAAD.Pro, while software such as Ansys and Abaqus are recognised for even broader applications (e.g. application in biomechanics or for thermal, electromagnetic and acoustic analyses).

The main idea of FEM lies in a discretisation of a continuum model into smaller parts (finite elements) which are interconnected by nodes, forming a finite element mesh through which the load and kinematic quantities are transmitted. Each node contains the unknown parameters of the system, whose solutions are approximated using the chosen shape function (e.g. a polynomial) within the domain of the element. A set of algebraic equations of an individual finite element is obtained in this way, and the system of finite element equilibrium equations for the whole model is also obtained by assembling all finite element equations of the discretised model. The solutions for the nodal unknowns, and then for the finite element fields, can be computed by solving the system of algebraic equations for the entire model. Finite element solutions are often obtained by variational principles [87, 89, 91]. The accuracy of numerical solutions based on FEM is certainly influenced by the finite element mesh (number of elements, possible distortion of elements in the mesh, etc.). The numerical solution of unknown fields approaches the correct solution as the mesh of properly designed finite elements becomes denser. However, this also increases the number of algebraic equations in the entire system that needs to be solved, which extends the process of numerical calculation. Many authors have used various improved interpolation functions and different approaches to formulate more efficient finite elements (see, for example [92–95]).

As mentioned in Chapter 1, further development of high-quality micropolar finite elements is of great importance for the future progress of Cosserat theory and its application, both as a simulation tool directly applicable to engineering problems and as a reliable modelling tool in virtual experimental setups to determine unknown additional micropolar material parameters by inverse analysis. Accordingly, one of the main objectives of this thesis is to develop new reliable and high-quality finite elements for the linear static and dynamic analysis of the micropolar continuum, which will then be used for the identification of micropolar material parameters by inverse numerical analysis. In this work, a displacement-based approach is used, that is, the nodal displacements as well as the nodal rotations are interpolated. Considering that the Timoshenko beam (in linear analysis) and Simo-Reissner beam [96,97] (in non-linear analysis) actually represent a 1D micropolar continuum (due to the existence of independent rotational degrees of freedom), they will be our starting point for formulating appropriate interpolation functions.

In the following, we provide a brief introduction to the Timoshenko beam theory as well as the Simo-Reissner beam theory, specifically addressing how some potential problems may appear during the implementation of those beam theories in the framework of FEM. We give a brief overview of some known interpolation schemes and after that, we specifically analyse how the standard and some more innovative interpolation schemes used in non-linear mechanics involving large 3D rotations transform when the analysis becomes linear. Among these we specifically address helicoidal interpolation [98], fixed-pole interpolation [99] and linked interpolation [100], in addition to ordinary Lagrangian interpolation, pin-point the similarities in these interpolations and numerically assess them. The knowledge of this interdependence is crucial for identifying paths for possible enhancement and extension from the Timoshenko beam of arbitrary order to a new finite element of arbitrary order for linear analysis of the 3D micropolar continuum.

3.1 Problems arising from FEM implementation of beam theories with rotational degrees of freedom

A prismatic solid whose cross-sectional dimensions (height h and width w) are significantly smaller than a longitudinal dimension (length L) can be considered as a beam. We can use beam models to describe many engineering problems, which is the reason why the beam theory has been studied and significantly developed for more than three centuries. The most well-known and commonly used theories in linear analysis are the Euler-Bernoulli beam theory and the Tim-

Timoshenko beam theory. Euler and Bernoulli derived the differential equation of the elastic line, and their beam theory of bending is considered as the first comprehensive beam theory. This theory does not take into account the shear strains of the beam cross-section, and thus makes the displacement and the rotation mutually dependent quantities, that is, Euler-Bernoulli beams have displacements \mathbf{u} and dependent rotations, represented as derivatives of displacements $\frac{d\mathbf{u}}{dx}$, as their degrees of freedom. It is also assumed that the cross-section of the beam remains planar and orthogonal to the centreline (reference axis) of the beam during deformation. However, the shear strains cannot be neglected in some cases. Hence, the Timoshenko theory was developed as an extension of the Bernoulli beam theory, where the effect of shear deformation is no longer neglected. As Timoshenko theory additionally includes the angular deformation caused by the shear deformation, the cross sections are no longer perpendicular to the neutral axis of the beam after deformation. So, the total rotation of the cross-section of the beam is given by the rotation of the tangent to the centreline and the shear deformation (see for example [6, 8], for more detail about these theories). In this thesis we will only consider the Timoshenko beam theory.

In the numerical analysis of the Timoshenko beam under the influence of transverse forces, the problem of *shear-locking* arises due to the assumption of displacement and rotation independence. If this problem is not properly treated, we obtain an artificial stiffness of the observed element, which leads to extremely small values of displacements. This problem can be eliminated by applying reduced numerical integration or mitigated by increasing the degree of interpolation of the Lagrangian polynomials [101]. One of the ways to improve the solution given by finite element procedures is enhancing the displacement field with the rotations, i.e. by applying the so-called *linked interpolation* which is already widely used and thoroughly investigated in finite element applications of the Timoshenko beam [89, 102–104] and the Reissner-Mindlin plate theory [93]. An important feature of the linked interpolation is that the displacement is interpolated with a polynomial of one-degree higher than the polynomial that interpolates the rotational unknowns. To formulate the expression of the linked interpolation for the 3D Timoshenko beam finite elements, Jelenić and Papa [100] start from the analytical solution of the differential equilibrium of the spatial beam. In this way, the linked interpolation yields exact solutions for an arbitrary polynomial loading and a sufficient finite number of nodal points, thus eliminating the shear-locking problem. The beam finite element with the linked interpolation gives the exact solution of the entire unknown field and the exact strain and stress resultant distributions according to

the Timoshenko beam theory. Jelenić and Papa have presented the linked interpolation in two different ways. The first formulation represents an interpolation that depends on the material and geometrical characteristics of the beam (a problem-dependent interpolation) by introducing a full set of boundary conditions [105]. On the other hand, there is a formulation independent of the material and geometrical properties of the beam (a problem-independent interpolation) [100]. Both interpolations give us the exact stiffness matrix [103].

The Timoshenko beam theory is based on small deformations and small rotations (first-order deformation theory). The first who made a significant step in the development of beam theory in the non-linear analysis is Reissner in [96] where the plane beam theory is based on large (finite) deformations, i.e. on geometrically exact kinematic equations. The mathematical formulation of the geometrically exact beam is very suitable for describing structures that can be subjected to arbitrarily large rotations such as robotic arms, helicopter rotor blades, wind farms, cable ropes, etc. Simo and Vu-Quoc extend geometrically exact beam theory to dynamic problems [106] and additionally, Simo generalized the theory for 3D beams [97].

The implementation of Simo-Reissner's theory within the framework of the finite element method becomes non-trivial due to the property of spatial rotations. These rotations are defined by orientation matrices belonging to the special orthogonal group $SO(3)$ [107], which is also a Lie group named after Norwegian mathematician Sophus Lie. Lie group G is both: a differentiable (smooth) manifold and a continuous group [108]. Saying it is a manifold means that it looks locally like n -dimensional space \mathbb{R}^n [109]. For each Lie group there exists a corresponding Lie algebra and the exponential map for mapping the algebra into the group. It is necessary to direct a special attention to the process of interpolating the non-linear degree of freedom of the configuration space (i.e. rotations), so that the property of objectivity of the solution with the respect of the observed reference frame is not lost during the numerical procedure [110].

Borri and Bottasso [98, 111] were faced with the problem of defining the reference axis of the beam during modelling curved mechanical elements (e.g., a helicopter propeller), so they needed a formulation that would provide a solution independent of the chosen reference axis. As a possible solution, they assumed that the reference axis of the deformed beam takes the shape of a spatial helicoid resulting from the constant distribution of the translational and rotational strain components along the beam. As a result, the position vector and the rotation tensor are described by a helicoidal interpolation restricted to two-node beam elements only. The finite

element obtained in this way is resistant to the shear-locking problem, and such a formulation represents a possible solution to the problem of non-objectivity, although this was not the author's original intention.

Jelenić and Crisfield [112] proposed a path-independent geometrically exact isoparametric spatial beam element of arbitrary order, in which the current local rotations are interpolated by a strain-invariant interpolation, while the position vector is interpolated in a Lagrangian manner. This formulation shows the property of strain invariance with respect to the displacement and rotation of a rigid body and the problem of shear-locking is solved by reduced integration. It is interesting to note that in the case of a beam finite element with two nodes, the strain-invariant interpolation gives exactly the same formulation of the rotational field as the helicoidal interpolation. In the linear analysis, the formulation takes the form of the Lagrangian interpolation for both fields.

Papa Dukić et al. [113] presented a configuration-dependent interpolation for 2D beam finite elements as an extension of the helicoidal interpolation to higher-order elements using a strain-invariant methodology, and showed that such interpolation leads to solutions that are not subject to shear-locking. Two variants were proposed of which, the first provided the solution that is independent of the choice of reference axis, but not exact in linear analysis, except for the two-node elements. The second variant is complementary and gives the exact solution in the linear analysis, but only for the case when the reference axis is also the centreline of the considered beam. Both variants give the same results for two-node beams.

Subsequently, Bottasso and Borri [99] introduced the so-called fixed-pole concept, which has proved to be useful in the non-linear dynamic analysis of 3D beams. Their main idea consists in replacing the resultant of the stress-couple and the specific angular momentum, defined according to the Reissner approach with respect to the beam reference axis, with new ones, now defined with respect to the unique point as the origin of the whole observed system (fixed-pole). They have also managed to connect the displacement field to the rotation field by a configuration tensor, which belongs to the special group of rigid motion $SR(6)$ which is also a Lie group. The implementation of this concept shows the ability of simultaneous conservation of both energy and momentum vectors. However, the elements suffer from the lack of objectivity with respect to the chosen position of the observer, even in planar analysis, and consequently from the strain non-invariance due to the rigid-body motion [107]. This concept can be applied to finite element beams of arbitrary order. The authors also showed that there is a 4D matrix representation of

the configuration tensor in terms of a special Euclidean group $SE(3)$, which is also a Lie group, and for which there is also an exponential mapping in closed form.

Sonneville et al. [114] developed a geometrically exact beam finite element formulated on the $SE(3)$ group, applying a helicoidal interpolation, which led to a very robust formulation resistant to shear-locking, but also limited to two-node beams. In the linear analysis of two-node beams, this formulation takes the form of the linked interpolation.

Gaćeša and Jelenić [107] proposed a new family of geometrically exact spatial beam elements based on the fixed-pole approach, but with standard nodal degrees of freedom (displacements and rotations) called the modified fixed-pole approach. The family consists of three different interpolation formulations that are shown to be non-invariant and path-dependent. For two of these interpolation formulations, this issue can be solved easily by interpolating the total local rotations, which also makes the procedure more robust in dealing with large load increments [107].

3.2 Standard and innovative interpolations in non-linear problems with large 3D rotations and their linearised forms

In view of the fact that the mentioned interpolation schemes possess certain good properties and also some disadvantages, it is very important to understand their relationship for their further manipulation for the purpose of improvement. In particular, we will highlight here the helicoidal interpolation (which has no problems with the shear-locking and non-objectivity, but is limited only to two-node beam finite elements) and the original fixed-pole interpolation (which is characterised by a unique description of the unknown fields, has favourable properties in non-linear dynamics and is applicable to beam elements with an arbitrary number of nodes, but these elements suffer from non-objectivity), both of which originate from the non-linear analysis of beams. It has already been shown [115] that in the linear analysis, the helicoidal interpolation reduces to the linked interpolation (which is in this case limited to only two-node beam elements) and that is known to provide an exact solution for the Timoshenko beam subject to pure bending and constant shear. To the best of our knowledge, there are no known studies of the fixed-pole concept in the linear analysis, where certain advantages can still be expected, while the complexities and disadvantages that occur in non-linear analysis disappear (the configuration tensor becomes linear and the problem of non-objectivity of the solution disappears). Therefore, in the following, we provide an overview and analysis of standard and some innovative interpolation forms used for the geometrically exact beams [96, 116] and their linearised forms. In the process of the linearisation of the geometrically exact beam theory, all non-linearities in the field variables (displacements and rotations) are neglected, from which we derive the Timoshenko beam, which is, in fact, a 1D linear micropolar continuum. Some parts of the conducted research presented in the following are also shown in [85].

3.2.1 Configuration of 3D geometrically non-linear beam

Let us consider a spatial straight beam (Figure 3.1) of a length L and uniform cross-sectional area A in 3D Euclidean space defined by the orthonormal unit vectors \mathbf{e}_1 , \mathbf{e}_2 and \mathbf{e}_3 (inertial frame). For a given real scalar parameter $0 \leq x_1 \leq L$ which represents the position of the material point along the reference axis of the beam, we define an initial position of the beam reference axis in a 3D ambient space by a 3D real vector function $\mathbf{r}_0(x_1) \in \mathbb{R}^3$ concerning a spatially fixed right-handed Cartesian frame (x_1, x_2, x_3) . The orientations of the beam cross-sections are defined by

another set of right-handed orthonormal unit basis vectors of the moving frame $\mathbf{t}_{01}(x_1)$, $\mathbf{t}_{02}(x_1)$, $\mathbf{t}_{03}(x_1)$ for the initial state and $\mathbf{t}_1(x_1)$, $\mathbf{t}_2(x_1)$, $\mathbf{t}_3(x_1)$ for the deformed state. The first members of these two triads $\mathbf{t}_{01}(x_1)$, $\mathbf{t}_1(x_1)$ are perpendicular to the plane of a beam cross-section, while the other two vectors of the triads are directed along the remaining two principal axes of the cross-section.

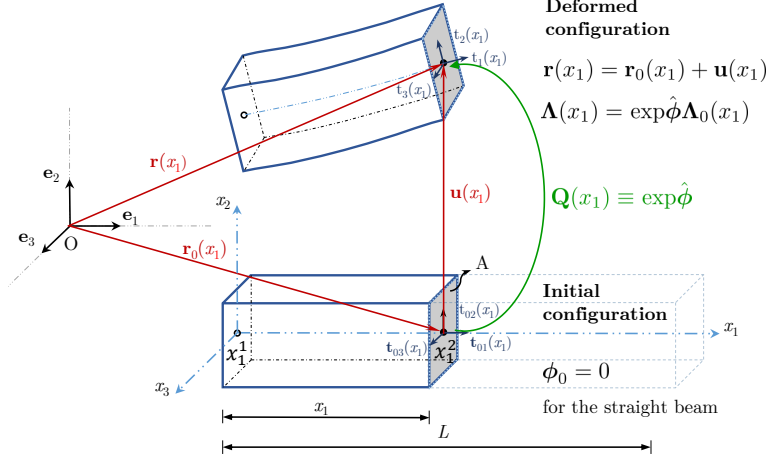


Figure 3.1: Initial and deformed state of a straight beam.

The relationship between inertial and moving frames is described by a transformation function $\mathbf{\Lambda}(x_1)$, where $\mathbf{\Lambda}$ is the rotation matrix or the orientation matrix which belongs to a special orthogonal group $SO(3)$ which is also Lie group and satisfies the conditions of orthogonality ($\mathbf{\Lambda}^T = \mathbf{\Lambda}^{-1}$) and unimodularity ($\det \mathbf{\Lambda} = +1$). Therefore, the initial orientation of the cross-section of the beam at x_1 is [97]

$$\mathbf{t}_{0i} = \mathbf{\Lambda}_0 \mathbf{e}_i, \text{ for } i = 1, 2, 3. \quad (3.1)$$

In the initial state, the cross-sections are orthogonal to the reference axis ($\mathbf{r}'_0 = \mathbf{t}_{01}$). Analogously, for the deformed state,

$$\mathbf{t}_i = \mathbf{\Lambda} \mathbf{e}_i. \quad (3.2)$$

The current configuration is completely determined by a position vector $\mathbf{r}(x_1) \in \mathbb{R}^3$ of a point along the beam reference axis with respect to the origin of a spatial coordinate system

$$\mathbf{r}(x_1) = \mathbf{r}_0(x_1) + \mathbf{u}(x_1), \quad (3.3)$$

where $\mathbf{r}_0(x_1)$ is an initial position vector and $\mathbf{u}(x_1)$ is the displacement of a point on the axis of

the observed cross section, and with the orientation tensor function

$$\mathbf{\Lambda}(x_1) = \mathbf{Q}(x_1)\mathbf{\Lambda}_0(x_1). \quad (3.4)$$

The linear transformation function $\mathbf{Q}(x_1)$ is related to a rotation vector function $\phi(x_1)$ which spins the initial orthogonal triad $\mathbf{t}_{0i}(x_1)$ into the current triad $\mathbf{t}_i(x_1)$ given by the Rodrigues rotation formula [117]

$$\mathbf{Q}(x_1) = \mathbf{I} + \frac{\sin \phi}{\phi} \hat{\phi} + \frac{1 - \cos \phi}{\phi^2} (\hat{\phi})^2 \equiv \exp \hat{\phi}, \quad (3.5)$$

where the hat operator $\hat{\bullet}$ above a 3D vector represents a skew-symmetric matrix which replaces a vector product such that for any two vectors \mathbf{a}, \mathbf{b} we have $\hat{\mathbf{a}}\mathbf{b} = \mathbf{a} \times \mathbf{b} = -\mathbf{b} \times \mathbf{a} = -\hat{\mathbf{b}}\mathbf{a}$, and ϕ represents the Euclidean norm $\phi = \sqrt{\phi_1^2 + \phi_2^2 + \phi_3^2}$, where ϕ_1, ϕ_2 and ϕ_3 are the components of ϕ in the spatial basis. In order to linearise Simo-Reissner beam theory we linearise the rotation vector such that $\sin \phi \rightarrow \phi, \cos \phi \rightarrow 1$ and all the higher-order terms in ϕ vanish, so that (3.5) reduces to

$$\mathbf{Q}(x_1) = \mathbf{I} + \hat{\phi}(x_1). \quad (3.6)$$

Substituting equation (3.6) into equation (3.4) we can express the rotation matrix $\mathbf{\Lambda}(x_1)$ for the current configuration of the initial straight beam for the linear case as

$$\mathbf{\Lambda} = (\mathbf{I} + \hat{\phi})\mathbf{\Lambda}_0. \quad (3.7)$$

The relationship between the variation of the rotation vector $\delta\phi$ and the spin vector $\delta\vartheta$ (related to the variation of the orientation matrix via $\delta\mathbf{\Lambda} = \delta\vartheta\mathbf{\Lambda}$) is given by $\delta\vartheta = \mathbf{H}(\phi)\delta\phi$, where $\mathbf{H}(\phi)$ is the tangent map defined as [118]

$$\mathbf{H}(\phi) = \mathbf{I} + \frac{1 - \cos \phi}{\phi^2} \hat{\phi} + \frac{\phi - \sin \phi}{\phi^3} \hat{\phi}^2. \quad (3.8)$$

3.2.2 Standard (Lagrangian) interpolation of displacements and rotations

To interpolate the displacement field \mathbf{u} and rotation field ϕ , we start first with a simple Lagrange interpolation in its well-known form [89, 119]

$$\mathbf{u}^h(x_1) = \sum_{i=1}^m N_i(x_1) \mathbf{u}_i \iff \mathbf{r}^h(x_1) = \sum_{i=1}^m N_i(x_1) \mathbf{r}_i, \quad (3.9)$$

$$\boldsymbol{\phi}^h(x_1) = \sum_{i=1}^m N_i(x_1) \boldsymbol{\phi}_i, \quad (3.10)$$

where superscript h denotes a discretization, m is the number of nodes of an element and $N_i(x_i)$ are the Lagrangian polynomials of order $m - 1$ defined as $N_i(x_1) = \prod_{\substack{j=1 \\ j \neq i}}^m \frac{x - x_j}{x_i - x_j}$, where x_i represents the position of the i^{th} node, while x_j is the position of the j^{th} node. It is clear that this interpolation is configuration-independent, i.e. linear in the nodal parameters. It comes with certain challenges, such as shear-locking issues, which can be eliminated by reduced numerical integration, as demonstrated in [120], where the Lagrangian interpolation is applied to a geometrically non-linear 3D beam with two nodes. There are other variants involving interpolation of rotations within the load step or within the Newton-Raphson iterative process (e.g. [116, 121]), but for linear problems they all reduce to the same form given above, as do many other alternative interpolations, which will not be discussed here.

3.2.3 Helicoidal interpolation of displacements

In [98], Borri and Bottasso presented helicoidal interpolation which arises from the requirement that the finite element solution of a beam problem should be independent of the choice of the reference axis and consistent with the configuration space. This requirement is satisfied when the position vector and the rotation tensor are interpolated using the same interpolation. It appears natural to apply the standard Lagrangian interpolation for both fields, but the Lagrangian interpolation of the rotation tensor is inconsistent with the rotation group character. As a solution, Borri and Bottasso assume that the reference axis of the deformed beam takes the shape of a spatial helicoid resulting from the constant distribution of the translational and rotational strain components along the beam. Therefore, the position vector and the rotation tensor along the beam are described by the helicoidal interpolation functions in the following way

$$\mathbf{r}^h(x_1) = \sum_{i=1}^2 \tilde{\mathbf{N}}_i \mathbf{r}_i, \quad (3.11)$$

$$\boldsymbol{\Lambda}^h(x_1) = \sum_{i=1}^2 \tilde{\mathbf{N}}_i \boldsymbol{\Lambda}_i, \quad (3.12)$$

with $\tilde{\mathbf{N}}_1 = \mathbf{I} - \tilde{\mathbf{N}}_2$, $\tilde{\mathbf{N}}_2 = \mathbf{H}(\phi^l)N_2\mathbf{H}^{-1}(\phi_2^l)$, $\phi^l = N_2\phi_2^l$ and ϕ_2^l coming from $\mathbf{\Lambda}_2 = \exp\hat{\phi}_2^l\mathbf{\Lambda}_1$ [98]. The specificity of the helicoidal interpolation is that it is limited to finite element beams with only two nodes ($m = 2$). The tangent map $\mathbf{H}(\phi^l)$ defined in (3.8), while its inverse is

$$\mathbf{H}^{-1}(\phi^l) = \mathbf{I} - \frac{1}{2}\hat{\phi}^l - \frac{1}{2}\frac{\phi^l \sin \phi^l + 2 \cos \phi^l - 2}{(\phi^l)^2(1 - \cos \phi^l)}(\hat{\phi}^l)^2. \quad (3.13)$$

In the linearised case the displacement and rotation interpolations have been shown in [115,122] to turn into

$$\mathbf{u}^h(x_1) = \sum_{i=1}^2 N_i(x_1) \left(\mathbf{u}_i + \frac{1}{2} \widehat{\phi^h - \phi_i} \mathbf{r}_{o,i} \right), \quad \phi^h(x_1) = \sum_{i=1}^2 N_i(x_1) \phi_i. \quad (3.14)$$

Borri and his co-workers [123] showed that there is also a 4D matrix representation of the configuration tensor in terms of a special Euclidean group $SE(3)$

$$\mathbf{C}_{4D} = \begin{bmatrix} \mathbf{\Lambda} & \mathbf{r} \\ \mathbf{0}^T & 1 \end{bmatrix}, \quad (3.15)$$

which also belongs to the Lie group, and for which there exists an exponential mapping in closed form. Sonnevile et al. [114] have developed a geometrically exact beam finite element formulated on $SE(3)$, applying a helicoidal interpolation, which has led to a very robust formulation for two-node beam elements. It is also interesting to note that in the case of two-node beam elements, the strain-invariant interpolation presented in [112] gives exactly the same interpolation of the rotational field as that provided by the helicoidal interpolation.

3.2.4 Original fixed-pole interpolation

The fixed-pole concept was introduced by Bottasso and Borri in [99], where they applied the concept in the geometrically non-linear analysis of a 3D beam. The idea has its origin in the approach whereby the stress resultant at a cross-section remains as it is, but the moment resultant is not referred anymore to the intersection of the cross-section with the beam reference axis, but to a *fixed pole*, usually taken to be the origin of the spatial coordinate system. This approach naturally leads to fixed-pole strains, fixed-pole velocities and fixed-pole angular moments.

The authors in [99] also presented the idea of unifying the position vector $\mathbf{r} \in \mathbb{R}^3$ and the

rotation vector $\mathbf{\Lambda} \in SO(3)$ using the six-dimensional configuration tensor \mathbf{C}_{6D} as

$$\mathbf{C}_{6D} = \begin{bmatrix} \mathbf{I} & \hat{\mathbf{r}} \\ \mathbf{0} & \mathbf{I} \end{bmatrix} \begin{bmatrix} \mathbf{\Lambda} & \mathbf{0} \\ \mathbf{0} & \mathbf{\Lambda} \end{bmatrix}, \quad (3.16)$$

i.e.

$$\mathbf{C}_{6D} = \begin{bmatrix} \mathbf{\Lambda} & \hat{\mathbf{r}}\mathbf{\Lambda} \\ \mathbf{0} & \mathbf{\Lambda} \end{bmatrix}, \quad (3.17)$$

where the left tensor in (3.16), called the transport operator stems out from the relationship between two definitions of a translational velocity: the velocity of the moving orthonormal frame (the spatial velocity) and the velocity with respect to a fixed point in space (the fixed pole velocity), while the spatial angular velocity is equal to the fixed-pole angular velocity. The second tensor in (3.16) arises from the connection between spatial translational and rotational velocities and their material counterparts [99]. The configuration tensor \mathbf{C}_{6D} belongs to the special group of rigid motions $SR(6)$, also a Lie group for which there exists a corresponding Lie algebra $sr(6)$ with a closed-form exponential mapping between them [99]. The vector element $\boldsymbol{\nu}$ of the Lie algebra $sr(6)$ which corresponds to the Lie group $SR(6)$, has 6 independent parameters and is defined as [99]

$$\boldsymbol{\nu} = \left\{ \begin{array}{c} \boldsymbol{\rho} \\ \boldsymbol{\phi} \end{array} \right\} \quad (3.18)$$

where $\boldsymbol{\phi}$ is the rotation vector and $\boldsymbol{\rho}$ is a quantity determined from exponential mapping in closed form. The corresponding element $\boldsymbol{\nu}$ of $sr(6)$ is completely defined after vectorial parametrisation, as

$$\left\{ \begin{array}{c} \boldsymbol{\rho} \\ \boldsymbol{\phi} \end{array} \right\} = \left\{ \begin{array}{c} \mathbf{H}^{-1}(\boldsymbol{\phi})\mathbf{r} - \mathbf{H}^{-T}(\boldsymbol{\phi})\mathbf{r}_o \\ \boldsymbol{\phi} \end{array} \right\} \quad (3.19)$$

with the function $\mathbf{H}(\boldsymbol{\phi})^{-T} = \mathbf{H}^{-1}(\boldsymbol{\phi}) \exp \hat{\boldsymbol{\phi}}$ (for more details see [99, 118]). In this way, instead of the standard unknown displacement field \mathbf{u} , the fixed-pole concept naturally introduces a new, non-standard kinematic $\boldsymbol{\rho}$, interpolated as $\boldsymbol{\rho}^h(x_1) = \sum_{i=1}^m N_i(x_1)\boldsymbol{\rho}_i$.

So far, there are no known investigations of the fixed-pole concept in linear analysis where a

unique description of all unknown fields can still be expected as an advantage of the concept. Thus, under the assumptions that the rotational vector is small, the trigonometric functions for small angles are approximated as $\sin \phi = \phi$, $\cos \phi = 1 - \frac{\phi^2}{2}$, and all higher order terms in ϕ vanish. Therefore, the inverse of the tangent map \mathbf{H}^{-1} takes the form

$$\mathbf{H}^{-1}(\phi) = \mathbf{I} - \frac{1}{2}\hat{\phi}. \quad (3.20)$$

and the unknown kinematic field $\boldsymbol{\rho}$ in the linear analysis is approximated as

$$\boldsymbol{\rho} = (\mathbf{I} - \frac{1}{2}\hat{\phi})\mathbf{r} - (\mathbf{I} + \frac{1}{2}\hat{\phi})\mathbf{r}_o. \quad (3.21)$$

Substituting the position vector $\mathbf{r} = \mathbf{r}_o + \mathbf{u}$, the field

$$\boldsymbol{\rho} = \mathbf{u} + \hat{\mathbf{r}}_o\phi \quad (3.22)$$

is obtained leading to the displacement interpolation $\mathbf{u}^h(x_1) = \boldsymbol{\rho}^h - \hat{\mathbf{r}}_o^h\phi^h = \sum_{i=1}^m N_i(x_1)(\mathbf{u}_i + \hat{\mathbf{r}}_{o,i}\phi_i) - \hat{\mathbf{r}}_o^h \sum_{i=1}^m N_i(x_1)\phi_i$. With the assumption that the initial geometry can be interpolated as $\mathbf{r}_o^h(x_1) = \sum_{i=1}^m N_i(x_1)\mathbf{r}_{o,i}$ (a straight beam), this gives

$$\mathbf{u}^h(x_1) = \sum_{i=1}^m N_i(x_1)(\boldsymbol{\rho}_i - \hat{\mathbf{r}}_o^h\phi), \quad (3.23)$$

or

$$\mathbf{u}^h(x_1) = \sum_{i=1}^m N_i(x_1)\left(\mathbf{u}_i + \widehat{\phi^h - \phi_i\mathbf{r}_{o,i}}\right), \quad (3.24)$$

while the rotation field is interpolated by the standard Lagrangian interpolation $\phi^h(x_1) = \sum_{i=1}^m N_i(x_1)\phi_i$.

3.2.5 Linked interpolation

In the so-called linked interpolation, the displacement field is interpolated using a one-degree higher polynomial than the polynomial that interpolates the rotational unknowns, and it has been widely used and thoroughly investigated in finite-element applications of the Timoshenko beams [89, 102, 104, 124, 125] and the Reissner-Mindlin plates [93, 126]. The linked interpolation considered here is in its general, problem-independent, form for a beam with m nodes presented

in [100] as

$$\mathbf{u}^h(x_1) = \sum_{i=1}^m N_i(x_1) \left(\mathbf{u}_i + \frac{1}{m} \widehat{\phi - \phi_i \mathbf{r}_{o,i}} \right), \quad (3.25)$$

derived from the analytical solution of the differential equation of the spatial Timoshenko beam for given kinematic boundary conditions. In this way, the linked interpolation provides exact solutions for arbitrary polynomial loading of order p and a sufficient finite number of nodal points ($m \geq p + 4, m \geq 3$ for point loading), eliminating the shear-locking problem. For the case of $m = 2$, the linked interpolation is equal to the linearised helicoidal interpolation.

3.2.6 Relationships between the presented interpolations

All the interpolation functions presented in Subsections 3.2.2 - 3.2.5 in their linear form can be unified in a simple manner as

$$\mathbf{u}^h(x_1) = \sum_{i=1}^m N_i(x_1) \left(\mathbf{u}_i + \frac{1}{k} \widehat{\phi - \phi_i \mathbf{r}_{o,i}} \right), \quad (3.26)$$

$$\phi^h(x_1) = \sum_{i=1}^m N_i(x_1) \phi_i, \quad (3.27)$$

where m and k are given in Table 3.1.

Table 3.1: Coefficients m and k in the interpolations presented in Sections 3.2.2 - 3.2.5.

Interpolation	Section	m	k
Lagrangian	3.2.2	≥ 2	∞
Helicoidal	3.2.3	2	2
Fixed-pole	3.2.4	≥ 2	1
Linked	3.2.5	≥ 2	m

Remark 1 Although they do not describe the exact distributions of displacements, the Lagrangian and the fixed-pole interpolation still provide the correct stiffness matrix [101] if the reduced numerical integration is used. Interestingly, both yield the same stiffness matrix also when the full integration is applied; however, this leads to shear-locking.

Obviously, to provide the exact solution for a static problem subject to polynomial loading, the interpolations presented in Sections 3.2.2 - 3.2.4 need to be adjusted to coincide with linked interpolation (k changed to m and, in the case of helicoidal interpolation, m allowed to be ≥ 2).

Clearly, the terms "Lagrangian", "helicoidal" and "fixed-pole" do not then retain the original meaning, but we still keep them for the sake of clarity. In particular, to achieve this, the fixed-pole interpolation (3.23) needs to be enhanced to read

$$\mathbf{u}^h(x_1) = \sum_{i=1}^m N_i(x_1) \left(\boldsymbol{\rho}_i - \frac{1}{m} \hat{\mathbf{r}}_o^h \boldsymbol{\phi} \right). \quad (3.28)$$

3.3 Conclusion

In this Chapter, we have started from some well-known interpolation schemes originating from the analysis of geometrically non-linear beams. These in particular include the helicoidal interpolation (interpolation on the SE (3) Lie group) and the fixed-pole approach (interpolation on the SR (6) group), which demonstrate certain advantages, but also some weaknesses in their application in numerical analysis. We focus here on the fixed-pole interpolation, which has not yet been investigated in a linear analysis. However, it has been shown that the linearisation of the original fixed-pole interpolation ultimately leads to a stiffness matrix equivalent to that provided by simple Lagrangian interpolation, for which we know that leads to the shear-locking problem and requires application of reduced numerical integration. On the other hand, it is already known that the helicoidal interpolation in the linear analysis takes the form of the linked interpolation for two-node beams.

From the investigation of the relationship between the Lagrangian, the helicoidal and the fixed-pole interpolation in their linear form with the well-known linked interpolation, the new enhanced fixed-pole interpolation has emerged as a possible interpretation of the linked interpolation. By introducing an additional coefficient into the enriched part of the interpolated displacement field, the same formulation is obtained as in the application of the linked interpolation for the standard degrees of freedom, which is known to provide an exact solution for the 3D Timoshenko beam of arbitrary order.

Chapter 4

Numerical analysis of micropolar continuum

The derived formulation of the hexahedral micropolar finite element of arbitrary order presented in this Chapter is also shown in: [85] Grbac, L., Jelenić, G., Ribarić D., Grbčić Erdelj, S., "Hexahedral finite elements with enhanced fixed-pole interpolation for linear static and vibration analysis of 3D micropolar continuum" International Journal for Numerical Methods in Engineering. 2024; 125(8):e7440; as well as a few selected numerical results.

In the static linear analysis of Timoshenko beams, the linked interpolation is widely used, but it is not sufficiently explored in the general micropolar continuum theory. It has only been applied to the static linear analysis of a 2D micropolar continuum in [41], where its enhanced accuracy compared to the standard Lagrangian interpolation has been observed. In Chapter 1, it has been shown that many authors have proposed diverse approaches for the numerical analysis of a micropolar continuum, but there is definitely a room for improvement, especially in the dynamic analysis. The research and the conclusions obtained in Chapter 3 motivate us to further investigate the application of the enhanced fixed-pole interpolation in the linear static analysis of the 3D micropolar continuum, while the application of both the original and the enhanced fixed-pole formulation will be also considered in the vibrational analysis.

Hence, in the first part of this Chapter, a new hexahedral finite element of arbitrary order is proposed for the linear analysis of the 3D micropolar continuum, where the enhanced fixed-pole interpolation is used to interpolate the displacement field, while the rotation field is interpolated using Lagrangian polynomials. After ensuring the convergence of the newly developed micropolar

element through a set of patch tests, two numerical examples of a 3D micropolar continuum in static equilibrium and free vibration of 3D micropolar plates with several different geometric properties are analysed. Based on these results, the newly proposed finite elements are critically assessed against the conventional elements.

In the second part, the proposed formulation is reduced for the analysis of a 2D micropolar continuum. The application of the enhanced fixed-pole interpolation leads to the identical formulation as provided by the linked interpolation, which was already applied in the static analysis of a planar micropolar continuum in [41]. However, it is noteworthy to emphasise that the fixed-pole formulation can be generalised to higher order elements in a very elegant way. It should be also noted that the Petrov-Galerkin approach is not used here, unlike in [41]. The new application of the 2D micropolar finite elements with this type of interpolation function is particularly emphasised here for the vibrational analysis.

4.1 Analysis of 3D micropolar continuum

4.1.1 Integral form of equations of motion

An integral (weak) formulation of the equations of motions in a 3D micropolar continuum follows from D'Alembert's principle (that is extension of the virtual work principle for dynamic problems) as

$$\int_V (\bar{\boldsymbol{\epsilon}}^T \mathbf{C}_1 \boldsymbol{\epsilon} + \bar{\boldsymbol{\kappa}}^T \mathbf{C}_2 \boldsymbol{\kappa}) dV - \int_V (\bar{\mathbf{u}}^T (\mathbf{p}_v - \rho \ddot{\mathbf{u}}) + \bar{\boldsymbol{\phi}}^T (\mathbf{m}_v - \mathbf{J} \ddot{\boldsymbol{\phi}})) dV - \int_S (\bar{\mathbf{u}}^T \mathbf{p}_s + \bar{\boldsymbol{\phi}}^T \mathbf{m}_s) dS = 0, \quad (4.1)$$

based on which a set of algebraic equations of motion will be obtained according to the finite element method after the introduction of interpolation functions for the real (\bullet) and virtual ($\bar{\bullet}$) kinematic fields. The external actions are the distributed volume force \mathbf{p}_v , volume moment \mathbf{m}_v , distributed surface force \mathbf{p}_s and surface moment \mathbf{m}_s . The constitutive matrices \mathbf{C}_1 and \mathbf{C}_2 are defined in (2.69) and (2.81), respectively, for a linear-elastic, isotropic centrosymmetric micropolar continuum. Introducing kinematic equations (2.52), (2.54) with the strain and curvature components expressed in the vector form, we obtain

$$\begin{aligned}
& \int_V \left[\left\langle \bar{\mathbf{u}}^T \quad \bar{\phi}^T \right\rangle \begin{bmatrix} \mathbf{D}^T \\ \mathbf{I}_\phi^T \end{bmatrix} \mathbf{C}_1 \begin{bmatrix} \mathbf{D} & \mathbf{I}_\phi \end{bmatrix} \begin{Bmatrix} \mathbf{u} \\ \phi \end{Bmatrix} + \left\langle \bar{\mathbf{u}}^T \quad \bar{\phi}^T \right\rangle \begin{bmatrix} \mathbf{0}^T \\ \mathbf{D}^T \end{bmatrix} \mathbf{C}_2 \begin{bmatrix} \mathbf{0} & \mathbf{D} \end{bmatrix} \begin{Bmatrix} \mathbf{u} \\ \phi \end{Bmatrix} \right] dV \\
& + \int_V \left(\left\langle \bar{\mathbf{u}}^T \quad \bar{\phi}^T \right\rangle \begin{bmatrix} \rho \mathbf{I} & \mathbf{0} \\ \mathbf{0} & \mathbf{J} \end{bmatrix} \begin{Bmatrix} \ddot{\mathbf{u}} \\ \ddot{\phi} \end{Bmatrix} \right) dV - \int_V \left(\left\langle \bar{\mathbf{u}}^T \quad \bar{\phi}^T \right\rangle \begin{Bmatrix} \mathbf{p}_v \\ \mathbf{m}_v \end{Bmatrix} \right) dV \quad (4.2)
\end{aligned}$$

$$- \int_S \left(\left\langle \bar{\mathbf{u}}^T \quad \bar{\phi}^T \right\rangle \begin{Bmatrix} \mathbf{p}_s \\ \mathbf{m}_s \end{Bmatrix} \right) dS = 0, \quad (4.3)$$

where $\mathbf{0}$ and \mathbf{I} are the 3×3 zero and identity sub-matrices, the matrix of differential operators is

$$\mathbf{D}^T = \begin{bmatrix} \frac{\partial}{\partial x_1} & \frac{\partial}{\partial x_2} & \frac{\partial}{\partial x_3} & 0 & 0 & 0 & 0 & 0 & 0 \\ 0 & 0 & 0 & \frac{\partial}{\partial x_1} & \frac{\partial}{\partial x_2} & \frac{\partial}{\partial x_3} & 0 & 0 & 0 \\ 0 & 0 & 0 & 0 & 0 & 0 & \frac{\partial}{\partial x_1} & \frac{\partial}{\partial x_2} & \frac{\partial}{\partial x_3} \end{bmatrix}, \quad (4.4)$$

and

$$\mathbf{I}_\phi^T = \begin{bmatrix} 0 & 0 & 0 & 0 & 0 & 1 & 0 & -1 & 0 \\ 0 & 0 & -1 & 0 & 0 & 0 & 1 & 0 & 0 \\ 0 & 1 & 0 & -1 & 0 & 0 & 0 & 0 & 0 \end{bmatrix} \quad (4.5)$$

represents a permutation matrix, while \mathbf{J} is tensor of a diagonal material microinertia density defined in Chapter 2.

To obtain the numerical solution of a problem, the kinematic fields have to be approximated using a chosen interpolation, and here we introduce the previously presented enhanced fixed-pole interpolation $\mathbf{u}^h(x_1) = \sum_{i=1}^m N_i(x_1) \left(\rho_i - \frac{1}{k} \hat{\mathbf{r}}_o^h \phi \right)$ for approximating the displacement field $\mathbf{u}^h = \mathbf{N}_u \mathbf{p}^e$ and virtual displacement field $\bar{\mathbf{u}}^h = \mathbf{N}_u \bar{\mathbf{p}}^e$, where the matrix of interpolation functions over an element is

$$\mathbf{N}_u = \begin{bmatrix} \mathbf{N}_1 & \mathbf{0} & \dots & \mathbf{N}_m & \mathbf{0} \end{bmatrix} - \frac{1}{k} \hat{\mathbf{r}}_o \begin{bmatrix} \mathbf{0} & \mathbf{N}_1 & \dots & \mathbf{0} & \mathbf{N}_m \end{bmatrix}, \quad (4.6)$$

with the spatial position vector $\mathbf{r}_o = \sum_{i=1}^m N_i \mathbf{r}_{o,i}$. The sub-matrices \mathbf{N}_i of Lagrangian polynomials of order $k - 1$ are defined as $\mathbf{N}_i = N_i \mathbf{I}$ for $i = 1, \dots, m$, where $m = k^3$ stands for the total number of nodes of each 3D finite element, while k represents the number of node along

the each coordinate axis. The real and virtual microrotation fields have been interpolated by Lagrangian polynomials as $\phi^h = \mathbf{N}_\phi \mathbf{p}^e$ and $\bar{\phi}^h = \mathbf{N}_\phi \bar{\mathbf{p}}^e$ with $\mathbf{N}_\phi = \begin{bmatrix} \mathbf{0} & \mathbf{N}_1 & \dots & \mathbf{0} & \mathbf{N}_m \end{bmatrix}$. The weak formulation of a 3D finite element is now defined with \mathbf{p}^e and $\bar{\mathbf{p}}^e$ as non-standard real and virtual nodal degrees of freedom of an element with arbitrary chosen number of nodes m

$$\mathbf{p}^e = \left\langle \mathbf{p}_1^T \quad \mathbf{p}_2^T \quad \dots \quad \mathbf{p}_m^T \right\rangle^{eT}, \quad \bar{\mathbf{p}}^e = \left\langle \bar{\mathbf{p}}_1^T \quad \bar{\mathbf{p}}_2^T \quad \dots \quad \bar{\mathbf{p}}_m^T \right\rangle^{eT}, \quad (4.7)$$

with $\mathbf{p}_i^T = \left\langle \rho_{1i} \quad \rho_{2i} \quad \rho_{3i} \quad \phi_{1i} \quad \phi_{2i} \quad \phi_{3i} \right\rangle^T$, $\bar{\mathbf{p}}_i^T = \left\langle \bar{\rho}_{1i} \quad \bar{\rho}_{2i} \quad \bar{\rho}_{3i} \quad \bar{\phi}_{1i} \quad \bar{\phi}_{2i} \quad \bar{\phi}_{3i} \right\rangle^T$, for $i = 1, \dots, m$. The equation of motion of a 3D micropolar finite element mesh thus can be obtained as

$$\begin{aligned} & \sum_{e=1}^{n_{el}} \bar{\mathbf{p}}^{eT} \left[\int_V \left[\left(\mathbf{B}_\rho^T - \frac{1}{k} \mathbf{B}_R^T + \left(\frac{k-1}{k} \right) \mathbf{B}_{I\phi}^T \right) \mathbf{C}_1 \left(\mathbf{B}_\rho - \frac{1}{k} \mathbf{B}_R + \left(\frac{k-1}{k} \right) \mathbf{B}_{I\phi} \right) \right. \right. \\ & \quad \left. \left. + \left(\mathbf{N}_\phi^T \mathbf{D}^T \right) \mathbf{C}_2 \left(\mathbf{D} \mathbf{N}_\phi \right) \right] dV \mathbf{p}^e + \int_V \begin{bmatrix} \rho \mathbf{N}_u^T \mathbf{N}_u & \mathbf{0} \\ \mathbf{0} & \mathbf{N}_\phi^T \mathbf{J} \mathbf{N}_\phi \end{bmatrix} dV \ddot{\mathbf{p}}^e - \\ & \quad \left. \int_V \left(\begin{bmatrix} \mathbf{N}_u^T \\ \mathbf{N}_\phi^T \end{bmatrix} \right)^T \begin{Bmatrix} \mathbf{p}_v \\ \mathbf{m}_v \end{Bmatrix} \right) dV - \int_S \left(\begin{bmatrix} \mathbf{N}_u^T \\ \mathbf{N}_\phi^T \end{bmatrix} \right)^T \begin{Bmatrix} \mathbf{p}_s \\ \mathbf{m}_s \end{Bmatrix} \right) dS \right] = 0 \end{aligned} \quad (4.8)$$

that is

$$\sum_{e=1}^{n_{el}} \bar{\mathbf{p}}^{eT} (\mathbf{K}^e \mathbf{p}^e + \mathbf{M}^e \ddot{\mathbf{p}}^e - \mathbf{f}^e) = 0 \quad (4.9)$$

where \mathbf{K}^e , \mathbf{M}^e and \mathbf{f}^e are the element stiffness and mass matrix and external force vector of an element e , for $e = 1, \dots, n_{el}$, where n_{el} is the total number of elements in a mesh and \mathbb{A} is the finite-element assembly operator. The \mathbf{B} matrices in (4.8) are $\mathbf{B}_\rho = \begin{bmatrix} \mathbf{B}_{\rho 1} & \mathbf{0} & \dots & \mathbf{B}_{\rho m} & \mathbf{0} \end{bmatrix}$, $\mathbf{B}_R = \begin{bmatrix} \mathbf{0} & \mathbf{B}_{R1} & \dots & \mathbf{0} & \mathbf{B}_{Rm} \end{bmatrix}$, $\mathbf{B}_{I\phi} = \begin{bmatrix} \mathbf{0} & \mathbf{B}_{I\phi 1} & \dots & \mathbf{0} & \mathbf{B}_{I\phi m} \end{bmatrix}$, where $\mathbf{0}$ is a 9×3 zero matrix and the sub-matrices in \mathbf{B}_ρ , \mathbf{B}_R and $\mathbf{B}_{I\phi}$ are

$$\mathbf{B}_{\rho i} = \begin{bmatrix} \frac{\partial N_i}{\partial x_1} & 0 & 0 \\ \frac{\partial N_i}{\partial x_2} & 0 & 0 \\ \frac{\partial N_i}{\partial x_3} & 0 & 0 \\ 0 & \frac{\partial N_i}{\partial x_1} & 0 \\ 0 & \frac{\partial N_i}{\partial x_2} & 0 \\ 0 & \frac{\partial N_i}{\partial x_3} & 0 \\ 0 & 0 & \frac{\partial N_i}{\partial x_1} \\ 0 & 0 & \frac{\partial N_i}{\partial x_2} \\ 0 & 0 & \frac{\partial N_i}{\partial x_3} \end{bmatrix}, \quad \mathbf{B}_{Ri} = \begin{bmatrix} 0 & -r_{x_3} \frac{\partial N_i}{\partial x_1} & r_{x_2} \frac{\partial N_i}{\partial x_1} \\ 0 & -r_{x_3} \frac{\partial N_i}{\partial y} & r_{x_2} \frac{\partial N_i}{\partial x_2} \\ 0 & -r_{x_3} \frac{\partial N_i}{\partial x_3} & r_{x_2} \frac{\partial N_i}{\partial x_3} \\ r_{x_3} \frac{\partial N_i}{\partial x_1} & 0 & -r_{x_1} \frac{\partial N_i}{\partial x_1} \\ r_{x_3} \frac{\partial N_i}{\partial x_2} & 0 & -r_{x_1} \frac{\partial N_i}{\partial x_2} \\ r_{x_3} \frac{\partial N_i}{\partial x_3} & 0 & -r_{x_1} \frac{\partial N_i}{\partial x_3} \\ -r_{x_2} \frac{\partial N_i}{\partial x_1} & r_{x_1} \frac{\partial N_i}{\partial x_1} & 0 \\ -r_{x_2} \frac{\partial N_i}{\partial x_2} & r_{x_1} \frac{\partial N_i}{\partial x_2} & 0 \\ -r_{x_2} \frac{\partial N_i}{\partial x_3} & r_{x_1} \frac{\partial N_i}{\partial x_3} & 0 \end{bmatrix}, \quad \mathbf{B}_{I\phi i} = \begin{bmatrix} 0 & 0 & 0 \\ 0 & 0 & N_i \\ 0 & -N_i & 0 \\ 0 & 0 & -N_i \\ 0 & 0 & 0 \\ N_i & 0 & 0 \\ 0 & N_i & 0 \\ -N_i & 0 & 0 \\ 0 & 0 & 0 \end{bmatrix}. \quad (4.10)$$

4.1.2 Hexahedral finite element with eight nodes

Unlike, for example, the couple-stress theory [21], which requires C^1 continuity (the continuity of the first derivatives) between adjacent finite elements, in the numerical analysis of the micropolar theory the fulfilment of C^0 continuity (the continuity of the function) is sufficient. Therefore, it is generally possible to apply linear Lagrangian interpolation for the interpolation of displacement and rotation fields. An isoparametric hexahedral finite element with 8 nodes and six degrees of freedom per node i has been chosen here for the discretisation of the 3D micropolar continuum (Figure 4.1) using the enhanced fixed-pole interpolation (which satisfies C^0 continuity) for the displacement field and the Lagrangian interpolation for the rotational field.

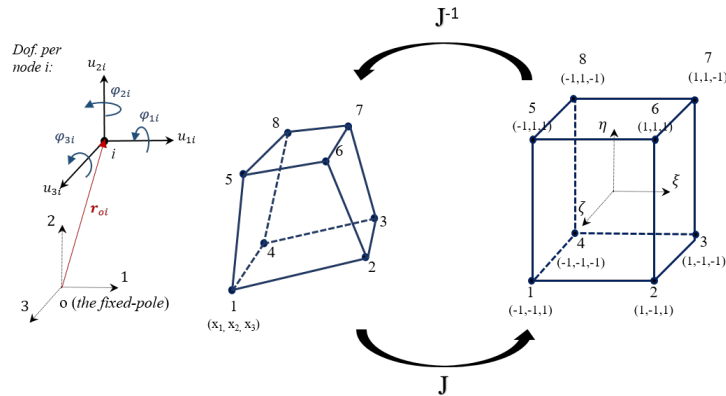


Figure 4.1: Hexahedral finite element with eight nodes - the relation between natural and global coordinates (according to [119])

Since the Cartesian global coordinate system is not always suitable for describing finite elements, a natural coordinate system is introduced. It is a system of local dimensionless natural coordinates (ξ, η, ζ) which take numerical values assumed to be between -1 and +1, and they are independent of the element's size. The term isoparametric means that the same interpolation functions are used to define the element geometry and kinematic fields. The mapping between the natural and the global coordinate system is defined as [89] $\mathbf{x}^h = \sum_{i=1}^8 N_i(\xi, \eta, \zeta) \mathbf{x}_i^e$, where $\mathbf{x}_i^e = \left\langle x_{1i}^e \quad x_{2i}^e \quad x_{3i}^e \right\rangle^T$ and $x_{1i}^e, x_{2i}^e, x_{3i}^e$ are the i^{th} node coordinates of an element. The components of the position vectors are also interpolated by the same Lagrangian polynomials $\mathbf{r}^h = \sum_{i=1}^8 N_i(\xi, \eta, \zeta) \mathbf{r}_i^e$ with $\mathbf{r}_i^e = \left\langle r_{1i}^e \quad r_{2i}^e \quad r_{3i}^e \right\rangle^T$ and

$$N_i(\xi, \eta, \zeta) = \frac{1}{8}[(1 + \xi_i \xi)(1 + \eta_i \eta)(1 + \zeta_i \zeta)], \quad (4.11)$$

$$\xi_i = \pm 1, \quad \eta_i = \pm 1, \quad \zeta_i = \pm 1$$

for node $i = 1, \dots, 8$

After introducing the chosen interpolation into (4.8) we can compute the element mass and stiffness matrix and the load vector. A numerical integration procedure is applied where an integral function that calculates both matrices and the load vector appear in the following form [89]

$$\int_V f(x_1, x_2, x_3) dV = \int_{-1}^{+1} \int_{-1}^{+1} \int_{-1}^{+1} f(\xi, \eta, \zeta) \det \mathbf{J} d\xi d\eta d\zeta \approx \sum_{i,j,k} w_{ijk} f(\xi_i, \eta_j, \zeta_k) \det \mathbf{J} \quad (4.12)$$

where w_{ijk} are the weight coefficients, $f(\xi_i, \eta_j, \zeta_k)$ are the functions to be integrated evaluated at the integration points, and for a regular prismatic 3D finite element of volume V the Jacobian determinant is a constant and equal to $\det \mathbf{J} = \frac{V}{8}$. We need eight integration points for this brick finite element with the chosen interpolation, for full Gaussian integration. The value of the natural coordinates of the Gaussian points $i=1\dots 8$ are $\xi_i = \pm \frac{1}{\sqrt{3}}, \eta_i = \pm \frac{1}{\sqrt{3}}, \zeta_i = \pm \frac{1}{\sqrt{3}}$ where the sign depends on the position of the point in an octant [89], with the weight coefficient $w = 1$. In terms of the standard degrees of freedom $\mathbf{p}_s^e = \left\langle \mathbf{p}_{s1}^T \quad \dots \quad \mathbf{p}_{sm}^T \right\rangle^{eT}$, with $\mathbf{p}_{si}^T = \left\langle u_{1i} \quad u_{2i} \quad u_{3i} \quad \phi_{1i} \quad \phi_{2i} \quad \phi_{3i} \right\rangle^T$ approximated weak form (4.9) may be written as

$$\bar{\mathbf{p}}_s^T (\mathbf{K}_s \mathbf{p}_s + \mathbf{M}_s \ddot{\mathbf{p}}_s - \mathbf{f}_s) = 0 \quad \text{for arbitrary } \bar{\mathbf{p}}_s \quad \Rightarrow \quad \mathbf{K}_s \mathbf{p}_s + \mathbf{M}_s \ddot{\mathbf{p}}_s = \mathbf{f}_s. \quad (4.13)$$

with $\mathbf{M}_s = \mathbb{A}_{e=1}^{n_{el}} \mathbf{M}_s^e$, $\mathbf{K}_s = \mathbb{A}_{e=1}^{n_{el}} \mathbf{K}_s^e$ and $\mathbf{f}_s = \mathbb{A}_{e=1}^{n_{el}} \mathbf{f}_s^e$, where $\mathbf{K}_s^e = \mathbf{R}_o^e \mathbf{K}^e \mathbf{R}_o^{eT}$ and $\mathbf{M}_s^e = \mathbf{R}_o^e \mathbf{M}^e \mathbf{R}_o^{eT}$ where \mathbf{R}_o^e follows from $\mathbf{u}_i = \boldsymbol{\rho}_i - \frac{1}{n} \hat{\mathbf{r}}_{o,i} \phi_i$ as

$$\mathbf{R}_o^e = \begin{bmatrix} \mathbf{I} & \mathbf{0} & \cdots & \mathbf{0} & \mathbf{0} \\ -\frac{1}{k} \hat{\mathbf{r}}_{o1} & \mathbf{I} & \cdots & \mathbf{0} & \mathbf{0} \\ \vdots & \vdots & \ddots & \vdots & \vdots \\ \mathbf{0} & \mathbf{0} & \cdots & \mathbf{I} & \mathbf{0} \\ \mathbf{0} & \mathbf{0} & \cdots & -\frac{1}{k} \hat{\mathbf{r}}_{om} & \mathbf{I} \end{bmatrix}. \quad (4.14)$$

4.1.3 Numerical examples

The newly developed isoparametric hexahedral micropolar finite element with 8 nodes (called *Hex8EFP*) has been implemented in *FEAP* (Finite Element Analysis Programme [127]) written in Fortran, a compiled imperative programming language. An own written Python script has also been used for pre- and post-processing of the input and output data, as well as *ParaView*, an open-source application for visualisation. The convergence of the proposed finite element has been evaluated by performing a set of patch tests derived specifically for micropolar finite elements (for details see [34], [40]). A numerical analysis of two boundary value problems with a known analytical solution [60] has been also performed, as well as the natural frequency analysis for a couple of representative problems involving different boundary conditions. All results are compared with the numerical results using the conventional Lagrangian element (*Hex8L*).

4.1.3.1 Force patch test

In this patch test, we check whether the proposed elements can reproduce the constant stress condition, regardless of the number of elements used. The test has been performed on a cantilever beam subjected to an axial tensile load $p_s = 10 \text{ N/m}^2$ acting on the free-end face of the beam (Figure 4.2). The external surface load has been applied as shown in (4.8), and the values of the nodal forces and the additional nodal moments have been obtained as a result of integration over the surface on which the load acts. The chosen geometrical properties of the beam are the same as in [40]: $L = 10.0 \text{ m}$, $h = 2.0 \text{ m}$ and $b = 1.0 \text{ m}$, while the chosen material properties are $\mu = 1000 \text{ N/m}^2$, $\lambda = 1000 \text{ N/m}^2$, $\nu = 500 \text{ N/m}^2$, $\alpha = 20 \text{ N}$, $\beta = 20 \text{ N}$, $\gamma = 20 \text{ N}$. On the left-hand side of the beam, all displacements in the x_1 -axis direction are fixed so that $u_1(0, x_2, x_3) = 0$, while $u_2(0, 0, x_3) = 0$ and $u_3(0, 0, 0) = 0$ for $x_2 \in [0, h]$, $x_3 \in [0, b]$.

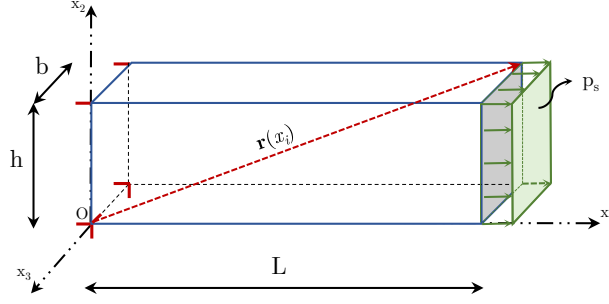


Figure 4.2: Cantilever beam subject to the pure tension.

The patch test is performed on a single-element mesh and a $2 \times 2 \times 2$ mesh. The obtained numerical solutions for both FE meshes provide all stress and couple-stress components equal to zero, except for the axial stress σ_{11} , which is equal to p_s , while the obtained axial displacement at the free end of the beam is equal to the analytical solution $u_x(L, x_2, x_3) = \frac{p_s L}{E}$ with the highest computer accuracy. Thus, the criterion of reproduction of the uniaxial stress state is satisfied.

Remark 2 It is important to point out that the external body and surface loads need to be applied in accordance with the chosen interpolation as shown in equation (4.8) resulting with the additional nodal moment forces. Correspondingly, the finite element Hex8EFP provides the analytical solution without the need to use the Petrov-Galerking method as in [41].

4.1.3.2 Displacement patch tests

In general, satisfaction of a patch test ensures the convergence of the finite elements used in the numerical analysis of a real problem. Three separate patch tests for a micropolar finite element formulation were proposed by Providas and Kattis [34]. Their tests were developed for 2D problems, and one of the possible generalisations from 2D to 3D is given in [40], which will be also analysed here. Let us consider a prismatic domain defined by length $L = 0.24 \text{ m}$, height $h = 0.12 \text{ m}$ and width $b = 0.06 \text{ m}$. The considered domain is discretised using 7 disordered hexahedral finite elements *Hex8EFP* as shown in Figure 4.3, where the coordinates of the internal nodes are defined as $P_9 = (0.04, 0.02, 0.02)$, $P_{10} = (0.18, 0.03, 0.02)$, $P_{11} = (0.018, 0.03, 0.04)$, $P_{12} = (0.04, 0.02, 0.04)$, $P_{13} = (0.08, 0.08, 0.02)$, $P_{14} = (0.16, 0.08, 0.02)$, $P_{15} = (0.16, 0.08, 0.04)$ and $P_{16} = (0.08, 0.08, 0.04)$. The material properties are kept as in the previous force patch test.

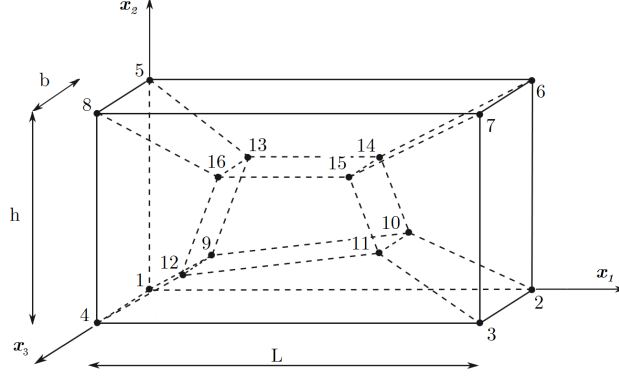


Figure 4.3: Distorted finite element mesh for the displacement patch tests (following [41]).

The first test represents a standard patch test for the finite elements in the classical theory of elasticity providing constant symmetric stress and strain fields. Linearly varying displacements and constant microrotation have been imposed at the external nodes as

$$\begin{aligned}
 u_1 &= 10^{-3}(x_1 + 0.5 \cdot x_2 + x_3), & u_2 &= 10^{-3}(x_1 + x_2 + 0.5 \cdot x_3), \\
 u_3 &= 10^{-3}(0.5 \cdot x_1 + x_2 + x_3), & \phi_1 &= \phi_2 = \phi_3 = 0.25 \cdot 10^{-3},
 \end{aligned} \tag{4.15}$$

without any applied external load. For this boundary conditions, the analytical solutions reads

$$\begin{aligned}
 \sigma_{11} = \sigma_{22} = \sigma_{33} &= 5.0, & \sigma_{12} = \sigma_{21} = \sigma_{13} = \sigma_{31} = \sigma_{32} = \sigma_{23} &= 1.5, \\
 \epsilon_{11} = \epsilon_{22} = \epsilon_{33} &= 10^{-3}, & \epsilon_{12} = \epsilon_{21} = \epsilon_{13} = \epsilon_{31} = \epsilon_{32} = \epsilon_{23} &= 0.75 \cdot 10^{-3},
 \end{aligned} \tag{4.16}$$

where all the couple-stress and curvature components are equal to zero.

The second test represents the state of constant non-symmetric stress and strain, where in addition to the first patch test, the constant microrotations are now given as $\phi_1 = \phi_2 = \phi_3 = 0.75 \cdot 10^{-3}$ and the constant body moments $m_{v1} = m_{v2} = m_{v3} = 1.0$ are provided in order to return the desired constant stress and strain fields. These boundary conditions and volume loading lead to the following analytical solutions for the stress and strain components:

$$\begin{aligned}
 \sigma_{11} = \sigma_{22} = \sigma_{33} &= 5.0, & \sigma_{13} = \sigma_{21} = \sigma_{31} &= 1.0, \\
 \sigma_{31} = \sigma_{12} = \sigma_{23} &= 2.0, & \epsilon_{11} = \epsilon_{22} = \epsilon_{33} &= 10^{-3}, \\
 \epsilon_{13} = \epsilon_{21} = \epsilon_{32} &= 0.25 \cdot 10^{-3}, & \epsilon_{31} = \epsilon_{12} = \epsilon_{23} &= 1.25 \cdot 10^{-3}.
 \end{aligned} \tag{4.17}$$

where all the couple-stress and curvature components are equal to zero.

In the *third test*, in addition to linearly varying displacements as in the first two tests, the microrotation $\phi_1 = \phi_2 = \phi_3 = 10^{-3}[0.25 + (x_1 - x_2 - x_3)]$, the body moment $m_{v1} = m_{v2} = m_{v3} = 2(x_1 - x_2 - x_3)$, and the constant body force $p_{v1} = 0.0$, $p_{v2} = 2.0$ $p_{v3} = -2.0$ are given, which leads to the following analytical solution:

$$\begin{aligned}
\sigma_{11} = \sigma_{22} = \sigma_{33} &= 5.0, & \sigma_{13} = \sigma_{21} = \sigma_{32} &= 1.5 - (x_1 - x_2 - x_3), \\
\sigma_{31} = \sigma_{12} = \sigma_{23} &= 1.5 + (x_1 - x_2 - x_3), & \epsilon_{11} = \epsilon_{22} = \epsilon_{33} &= 10^{-3}, \\
\epsilon_{13} = \epsilon_{21} = \epsilon_{32} &= 10^{-3}(0.75 - (x_1 - x_2 - x_3)), & \epsilon_{31} = \epsilon_{12} = \epsilon_{23} &= 10^{-3}(0.75 + (x_1 - x_2 - x_3)), \\
\mu_{11} = 0.02, & \mu_{22} = \mu_{33} = -0.06, & \mu_{12} = \mu_{13} = \mu_{23} = \mu_{32} &= -0.04, & \mu_{21} = \mu_{31} &= 0.04, \\
\kappa_{11} = \kappa_{12} = \kappa_{31} &= 10^{-3}, & \kappa_{22} = \kappa_{33} = \kappa_{12} = \kappa_{13} = \kappa_{23} = \kappa_{32} &= -10^{-3}.
\end{aligned} \tag{4.18}$$

Satisfaction of a patch test such as this one, in which stress distribution is not constant, is not considered to be necessary for convergence [89] and, for this reason, this test is treated as a higher-order patch test [40], similar to a pure bending test.

For the first two tests, the proposed finite element *Hex8EFP* provides the exact solution but for the third patch test it indeed does not reproduce the exact results. Table 4.1 shows the displacement components in all three directions and the microrotation around the x_1 -axis at the point P_9 as well as the stress and couple-stress components at the point with coordinates (0.07536, 0.03435, 0.024227). As argued above *Hex8EFP* is still convergent. Interestingly, the ordinary Lagrangian element *Hex8L* passes this test, but the proposed element *Hex8EFP* will perform better in the more demanding tests to be considered next.

Table 4.1: Numerical results for third displacement patch test: displacements/microrotation at P_9 , stress/couple stress at (0.07536, 0.03435, 0.02423).

	$u_1 \cdot 10^5$	$u_2 \cdot 10^5$	$u_3 \cdot 10^5$	$\phi_1 \cdot 10^4$	σ_{11}	σ_{13}	μ_{11}	μ_{12}
Exact solution	7.000	7.000	6.000	2.500	5.000	1.483	0.020	-0.040
Hex8EFP	6.9143	6.5613	6.5362	2.5016	4.965	1.482	0.0199	-0.0402

4.1.3.3 Pure bending test

Analytical solutions for two boundary value problems in terms of measurable surface tractions and displacements have been derived by Gauthier and Jahsman [60]. The first problem involves an elastic rectangular plate of length L , width b and height h subjected to pure bending by

end moments M around the coordinate axis x_3 , with lateral boundary conditions preventing anticlastic distortion and turning the problem into a pure cylindrical plane-strain bending of a rectangular micropolar beam. This means that $u_1(x_1, x_2)$, $u_2(x_1, x_2)$ and $\phi_3(x_1, x_2)$ are the only allowable displacement and microrotation components. In contrast to the classical theory of elasticity, where the concentrated moment M can only be generated by applying a linearly varying normal surface traction load $p_s = \frac{2 \cdot x_2}{h} p_0$ [128], Gauthier and Jahsman showed that for the pure bending of the micropolar continuum, the moment M must be generated by both the linearly varying surface load p_s and a constant surface moment m_s , i.e. $M = b \int_{-\frac{h}{2}}^{\frac{h}{2}} (x_2 \cdot p_s + m_s) dx_2$ which have to be defined as

$$p_s = \sigma_{11} = -\frac{1}{1 + (1 - n)\delta} \frac{M}{W} \frac{2x_2}{h}, \quad (4.19)$$

$$m_s = \mu_{31} = \frac{(1 - n)\delta}{1 + (1 - n)\delta} \frac{M}{A}, \quad (4.20)$$

with the cross-section area $A = bh$, the resistance moment about the neutral axis x_3 $W = \frac{bh^2}{6}$ and $\delta = 24(l_b/h)^2$. The state of pure bending is thus achieved only for a precisely determined ratio of m_s and p_s which depends on the micropolar material properties (for details see [42]), given as

$$\frac{m_s}{p_0} = \frac{1}{h} \frac{(\lambda + 2\mu)(\beta + \gamma)}{2\mu\lambda + \mu} \equiv \frac{h}{6}(1 - n)\delta. \quad (4.21)$$

The analytical solutions for displacement and microrotation fields are

$$\begin{aligned} u_1 &= -\frac{1}{1 + (1 - n)\delta} \frac{Mx_1x_2}{bD}, & u_2 &= \frac{1}{2} \frac{1}{1 + (1 - n)\delta} \frac{M}{bD} \left(x_1^2 + \frac{n}{1 - n} x_2^2\right) \\ \phi_3 &= \frac{1}{1 + (1 - n)\delta} \frac{Mx_1}{bD}, \end{aligned} \quad (4.22)$$

where $D = \frac{Eh^3}{12(1 - n^2)}$ represents the flexural rigidity. Due to the symmetry of the problem, only a half of the structure may be considered in the numerical analysis, which can be modelled as a cantilever beam of length $\frac{l}{2} = 10$ m, height $h = 2$ m, and thickness $b = 1$ m, with the following boundary conditions: $u_1(0, x_2, x_3) = u_2(0, 0, x_3) = u_3(x_1, x_2, x_3) = \phi_1(0, x_2, x_3) = \phi_2(0, x_2, x_3) = \phi_3(0, x_2, x_3) = 0$ (Figure 4.4). The beam is discretised using the proposed elements *Hex8EFP* and, for comparison, the numerical solutions have also been obtained by the standard Lagrangian elements *Hex8L* [40]. The resulting bending moment $M = 20$ Nm has

been applied through linearly varying surface loading and a constant surface moment loading in the defined proportion (4.21), at the free edge of the beam.

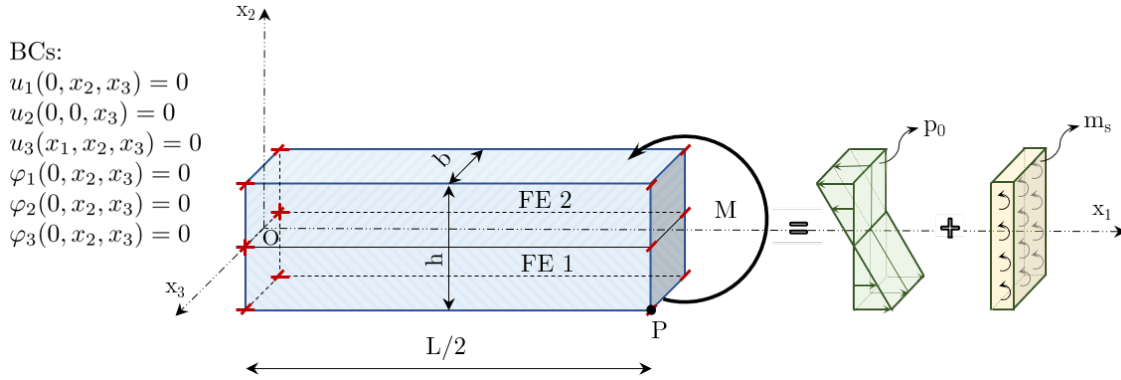


Figure 4.4: Discretised micropolar beam subjected to pure bending.

It is important to emphasise that the external surface loads and moments have been applied strictly in accordance with the chosen interpolation functions (4.8) which avoids the need to use the computationally more demanding Petrov-Galerkin approach as used in [41]. All geometrical and material properties, as well as the value of the resultant moment, are taken as in [40], i.e the engineering material parameters are $E = 1500N/m^2$ and $n = 0.25$ which give the Lamé constants $\lambda = 600N/m^2$ and $\mu = 600N/m^2$. In order to investigate the influence of the increase in bending stiffness due to the increase in the value of the characteristic length for bending (the *size-effect*) on the proposed element's accuracy, numerical solutions are provided for different values of the characteristic length $l_b = \frac{1}{2}\sqrt{\frac{\beta+\gamma}{G}}$, i.e for $l_b \in [0.0, 1.8]$. The microstructure of the material is neglected when $l_b = 0$ (classical continuum), with the concentrated moment generated only by the surface loading traction. As the ratio between the characteristic length for bending and the height of the beam increases the effective stiffness grows, as it does with decrease in the Poisson's ratio. The remaining additional micropolar engineering material parameters are in this problem inconsequential and can be chosen arbitrarily. Here they are taken as $N = 0.5$, $\Phi = 0$ and $l_t = 0.1$.

The problem is solved using a very rare mesh containing only two hexahedral finite elements *Hex8L* and *Hex8EFP* across the height of the beam. Table 4.2 shows the analytical solutions (*A*) and the numerical results (*N*) for the displacement u_2 and the microrotation ϕ_3 at the point $P(\frac{L}{2}, -\frac{h}{2}, \frac{b}{2})$, and for the stress σ_{11} , at the Gauss point with the co-ordinates (7.88675, 0.211325, 0.788675).

Table 4.2: Differences between analytical solutions and numerical results using *Hex8L* and *Hex8EFP*.

Element	$\frac{l_b}{h}$	Displacement u_2			Microrotation ϕ_3			Stress σ_{xx}		
		A	N	Error [%]	A	N	Error [%]	A	N	Error [%]
Hex8L	0.0	0.94063	0.06910	92.65	0.18750	0.01262	93.27	23.66030	1.96844	91.68
Hex8EFP			0.91212	3.03		0.18182	3.03		23.99300	1.41
Hex8L	0.05	0.90012	0.06892	92.34	0.17943	0.01269	92.93	22.64140	1.95033	91.39
Hex8EFP			0.87402	2.88		0.17426	2.88		22.99500	1.56
Hex8L	0.15	0.66948	0.06740	89.93	0.13345	0.01296	90.29	21.35230	1.83451	91.41
Hex8EFP			0.65566	2.06		0.13071	2.05		17.24470	19.24
Hex8L	0.3	0.35902	0.06203	82.72	0.07157	0.01261	82.38	11.45040	1.59974	86.03
Hex8EFP			0.35518	1.07		0.07082	1.05		9.34061	18.43
Hex8L	0.6	0.12575	0.04624	63.23	0.02507	0.00977	61.02	3.16310	1.14357	63.85
Hex8EFP			0.12527	0.38		0.02498	0.36		3.29403	4.14
Hex8L	0.9	0.06037	0.03224	46.59	0.01204	0.00691	42.63	1.51860	0.79036	47.95
Hex8EFP			0.06025	0.20		0.01202	0.21		1.58433	4.33

Convergence curves on the control size of the normalised vertical displacements at point P for both types of elements have been compared in Figure 4.5 for $l_b = 0.1$ and Figure 4.6 for $l_b = 1.8$, where the enhanced fixed-pole interpolation certainly shows a much better convergence towards the exact solutions.

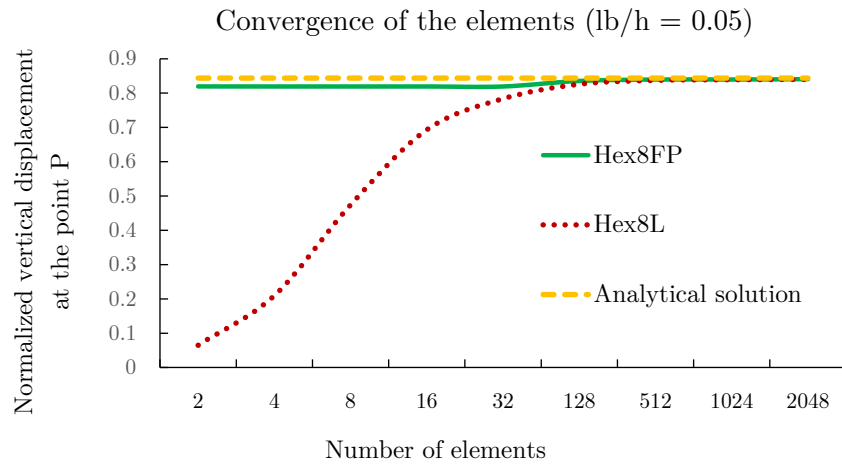


Figure 4.5: Convergence curves of *Hex8EFP* and *Hex8LI* elements for normalized vertical displacement u_2 when $l_b = 0.1$.

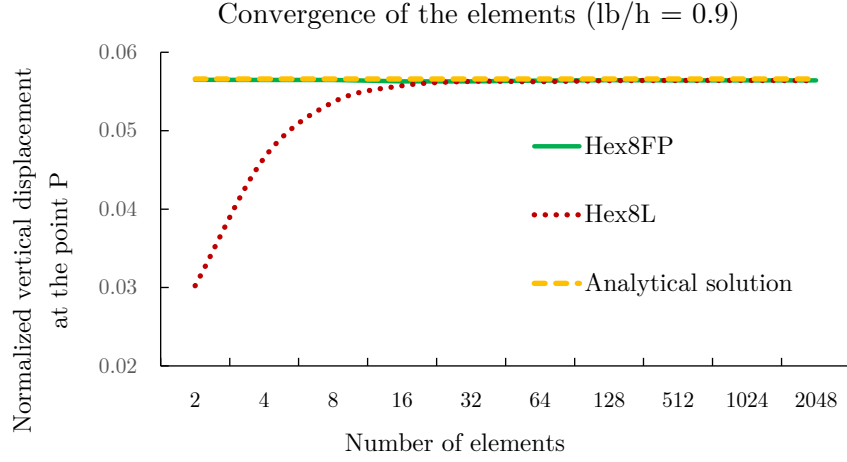


Figure 4.6: Convergence curves of *Hex8EFP* and *Hex8LI* elements for normalized vertical displacement u_2 when $l_b = 1.8$.

Considerable improvement in numerical results has been observed by applying the finite elements *Hex8EFP* instead of the standard Lagrangian elements *Hex8L* which give poor results. Table 4.2 also shows that more accurate numerical solutions are obtained for larger values of the characteristic length for bending (which also increases the stiffness). An even better performance was noted in [40] using the finite elements with incompatible modes, but this is achieved at the expense of additional numerical overhead as these elements contain additional internal degrees of freedom.

4.1.3.4 Torsion test on a solid cylinder

The second boundary-value problem considered is a cylinder of height c and radius a subjected to pure torsion (Figure 4.7a). The analytical solution in the cylindrical coordinate system (r, θ, x) for stresses, displacements, and microrotations has been provided by Gauthier and Jahsman [60] for the resultant torque T acting on the edge surfaces of the cylinder ($x = 0$ and $x = c$). As in the pure bending test, they showed that in the micropolar theory pure torsion can be achieved only if the external surface torque T is generated by a tangential traction $p_{s\theta}$ and an axial moment traction m_{sx} acting on the edge surfaces as follows

$$T = \int_A (r p_{s\theta} + m_{sx}) dA, \quad (4.23)$$

where $A = r^2\pi$ is the cross-section area of the cylinder, and where surface normal and moment tractions are described by micropolar material parameters and modified Bessel functions of the

first kind I_n of order n as

$$\sigma_{\theta x} = p_{s\theta} = \mu C_1 r + 2\nu C_9 I_1(pr), \quad \mu_{xx} = m_{sx} = \alpha p C_9 I_0(pr) + 2\beta C_1, \quad (4.24)$$

with

$$p = \sqrt{\frac{4\nu}{\alpha + 2\beta}}, \quad C_1 = 2C_9 \left(\frac{\alpha + 2\beta}{2\beta} p I_0(pa) - \frac{1}{a} I_1(pa) \right),$$

$$C_9 = \frac{T}{2\pi a^2} \left[\left(\frac{\mu a^2}{4\beta} + 1.5 \right) (\alpha + 2\beta) p I_0(pa) - \left(\frac{\mu a^2}{4\beta} + 2 \right) \frac{2\beta}{a} I_1(pa) \right]^{-1}. \quad (4.25)$$

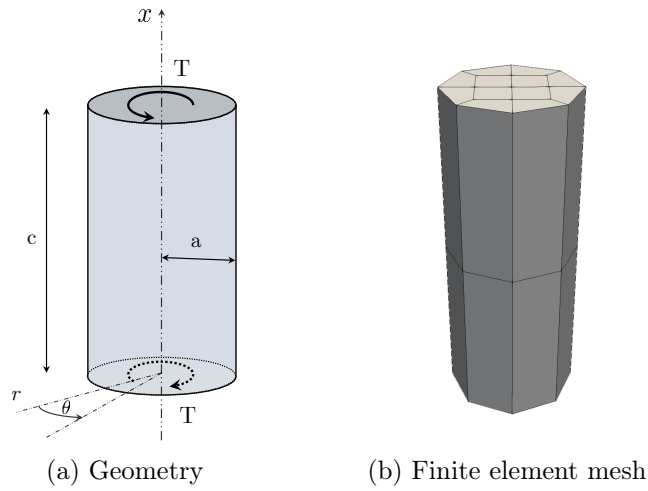


Figure 4.7: Solid circular cylinder under torsion.

Bessel functions are functions that result from the solution of Bessel equations, that is second-order linear differential equations. In situations where standard Bessel functions cannot adequately describe the solution, modified Bessel functions are applied as their variant [129].

All the fields are independent of the angle θ , where the displacement and rotation fields are obtained as

$$u_{\theta} = C_1 r x, \quad \phi_r = -\frac{C_1 r}{2} + C_9 I_1(pr), \quad \phi_x = C_1 x, \quad (4.26)$$

as described in detail in [40, 60]. A numerical analysis of the observed problem has been carried out, where all degrees of freedom are restricted at the bottom surface of the cylinder ($x = 0$). The material and geometrical characteristics have been taken from [40] as $a = 0.2\text{mm}$, $c = 1\text{mm}$, $\mu = 10\,500\text{N/mm}^2$, $\lambda = 157\,500\text{N/mm}^2$, $\nu = 3\,500\text{N/mm}^2$, $\alpha = 0\text{N}$, $\beta = 105\text{N}$, $\gamma = -105\text{N}$, based on which the corresponding engineering material parameters can be calculated. Since

parameter α is chosen to be zero, the moment surface loading m_{sx} becomes constant, while the tangential surface loading $p_{s\theta}$ is generally a non-linear function.

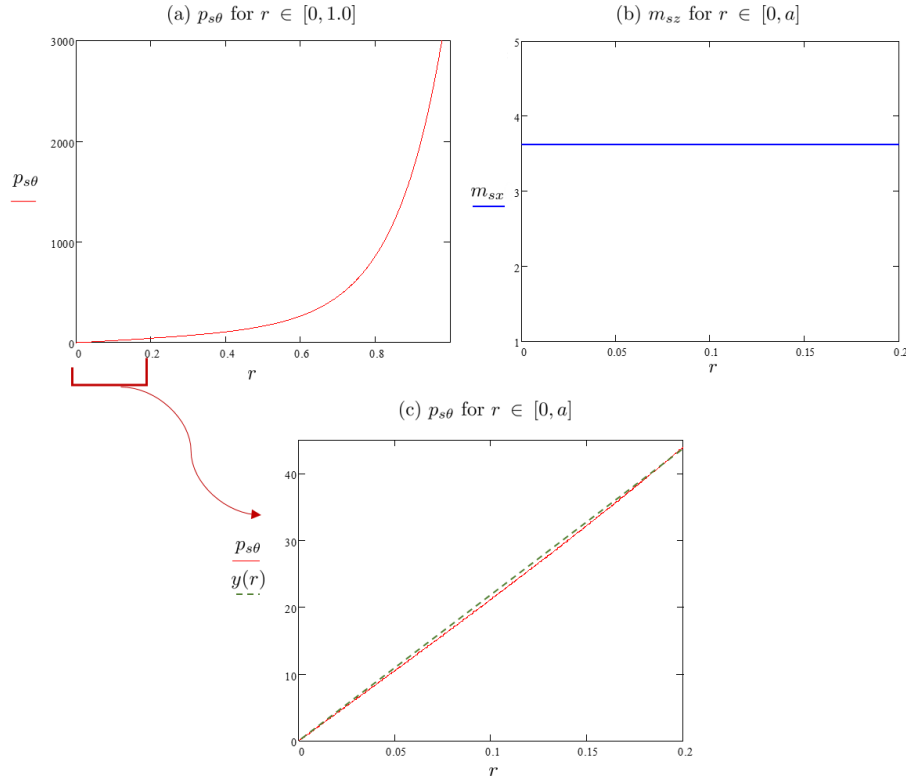


Figure 4.8: Graphs of external load distribution

If we look at the graph 4.8a of the $p_{s\theta}$ function, for a sufficiently small radius of the cylinder we can assume that the function is almost linear, and the value of the radius we have chosen belongs to this domain of linearity. The green line on the Figure 4.8c represents a linear function and we can see that it could be sufficient approximation of $p_{s\theta}$ function for that range. Thus, the resultant torque $T = 1 \text{ Nmm}$ in the finite-element model is distributed by a linearly varying surface traction with boundary values for $p_{s\theta}(0, \theta, c) = 0.0 \text{ N/mm}^2$, $p_{s\theta}(r, \theta, c) = 43.93044 \text{ N/mm}^2$, and a constant moment surface traction $m_{sx} = 3.63683 \text{ Nmm/mm}^2$. The solid cylinder has been discretised as an axisymmetric mesh of the proposed hexahedral finite elements *Hex8EFP*, and the Lagrangian finite elements *Hex8L*. It has been shown in [40] that the numerical solution using the Lagrange finite elements is in good agreement with the analytical solutions, even for the sparsest mesh of 24 finite elements (Figure 4.7b), and very similar to the solution obtained by the incompatible mode elements. In Table 4.3 we show that comparable results are obtained using *Hex8EFP*, too.

Table 4.3: Comparison between analytical and numerical results at $(a, 0, c)$ for the cylinder subjected to the torque using hexahedral finite elements with the enhanced fixed-pole and Lagrangian interpolation.

Element	$\phi_x \cdot 10^2$			$\phi_r \cdot 10^4$			$u_\theta \cdot 10^3$		
	A	N	Error [%]	A	N	Error [%]	A	N	Error [%]
Hex8L	1.7318	1.7378	0.35	-6.5151	-6.3600	2.38	3.4636	3.4779	0.41
Hex8EFP		1.7382	0.37		-6.3894	1.93		3.4779	0.41

The numerical solutions for the displacement $u_\theta(a, 0, c)$ and the microrotation $\phi_x(a, 0, c)$ have been analysed in the cases of five different ratios of the characteristic length for the torsion l_t and the radius r of the cylinder (Figure 4.9) in order to capture the *size-effect*. Indeed, as the l_b value increases, the micropolar torsional rigidity also grows and can be up to seven times higher than the classical torsional stiffness [60]. The numerical results are more accurate in the case of the higher values of l_b .

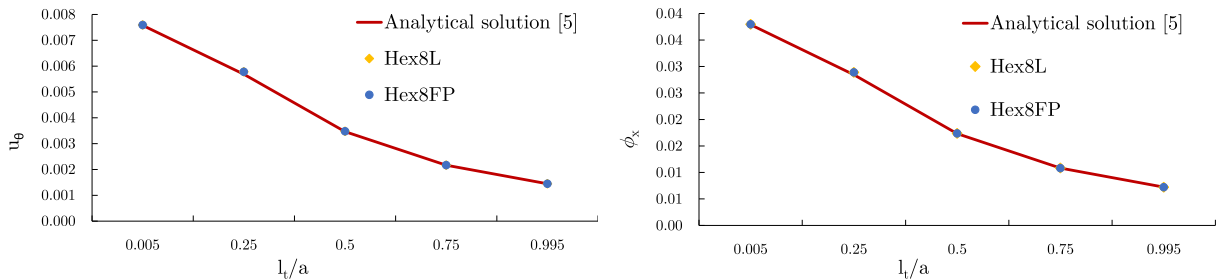


Figure 4.9: Comparison of numerical solutions for displacement u_θ and microrotation φ_{x_3} at node $(a, 0, c)$ with respect to l_b/a .

4.1.3.5 Vibration response of 3D micropolar square plates

A free vibration analysis of a 3D square plate with edge-length $L = 33.0$ mm and height $h = 3.3$ mm has been conducted. The plate has been subjected to two types of boundary conditions: (i) CCCC - a fully clamped plate, and (ii) CFFF - a cantilever plate, where C and F stand for clamped and free ends, respectively. The same plate, but with a central circular hole of radius $R = 0.3 \cdot L$ has been also analysed: (iii) CCCC - fully clamped plate with the hole and (iv) CFFF - cantilever plate with the hole. The plates are discretised using a regular mesh of the proposed hexahedral micropolar finite elements *Hex8EFP* and the Lagrangian elements *Hex8L* as well as the elements *Hex8OFP*, in which the original fixed-pole interpolation ($k = 1$) is used. Figure

4.10 shows schematic representations of the discretisation of the chosen plate geometry using a mesh of 1600 and 3200 elements for the full plate and plate with the circular hole respectively.

To validate the newly developed finite elements, the numerical results of the first three natural frequencies of (i) have been compared with the results presented in [48] which were obtained by a very dense mesh with the use of tetrahedral finite elements of the second order, which are here taken to represent the reference solutions. Furthermore, the first three eigenfrequency values for (iii) have been read from the graph in [48] and compared to the numerical results obtained with a very dense mesh of 256000 Hex8L elements, which yielded approximately equal results. For accuracy, the reference solution is the one obtained using Hex8L elements (Table 4.4). The geometric and material characteristics are defined as in [48]: $G = 104$ MPa, $n = 0.44$, $N = 0.04$, $l_b = 0.33$ mm, $l_t = 0.62$ mm, $\Psi = 1.5$, $\rho = 2000$ kg/m³, $j = 5 \cdot 10^{-5}$ m², $J = \rho j = 10^{-1}$ kg/m, that is $\mathbf{J} = J\mathbf{I}$, while the micropolar elasticity constants (2.85). After we have established that our newly presented finite elements converge to the solutions from [48], we have additionally considered the same plates but with CFFF boundary conditions (ii) and (iv), where the reference solutions have been obtained by FEM for a mesh with 25000 (ii) and 43264 (iv) *Hex8L* elements (Table 4.4).

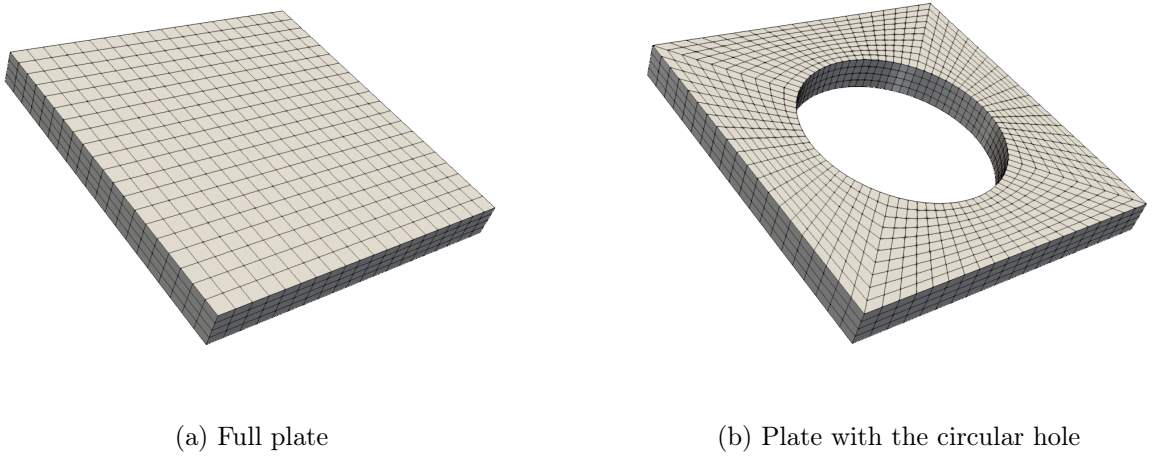


Figure 4.10: Schematic representation of the discretisation 3D micropolar plates.

Table 4.4: Reference solutions of the first three natural frequencies (f_1 , f_2 and f_3) of all four considered plate types.

Square plate type	f_1 [kHz]	f_2 [kHz]	f_3 [kHz]	FE number	Used FE
Full CCCC plate (i) [48]	14.2795	18.4830	18.4830	9000	2 nd order LI tetrah.
Full CFFF plate (ii)	2.0226	3.9761	7.8912	20000	1 st order LI hex.
CCCC plate with a circular hole (iii)	16.5992	17.5233	17.5233	25600	1 st order LI hex.
CFFF plate with a circular hole (iv)	1.6728	3.2666	6.6409	43264	1 st order LI hex.

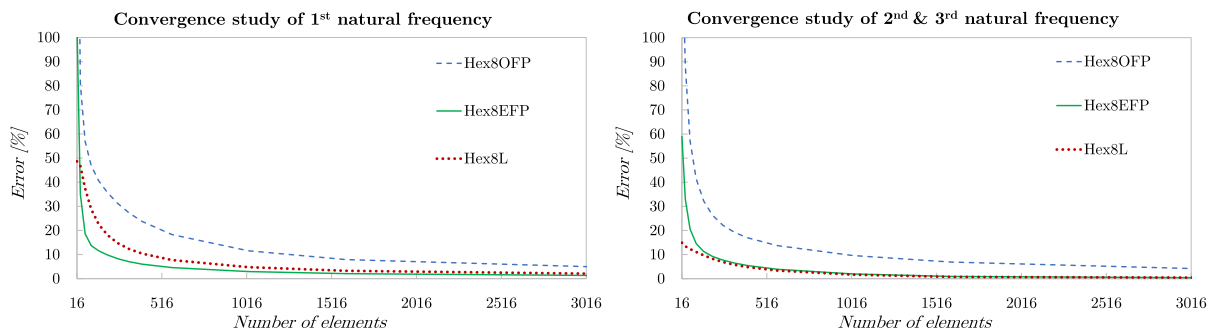


Figure 4.11: Convergence study of first three natural frequencies of CCCC plate (*i*)

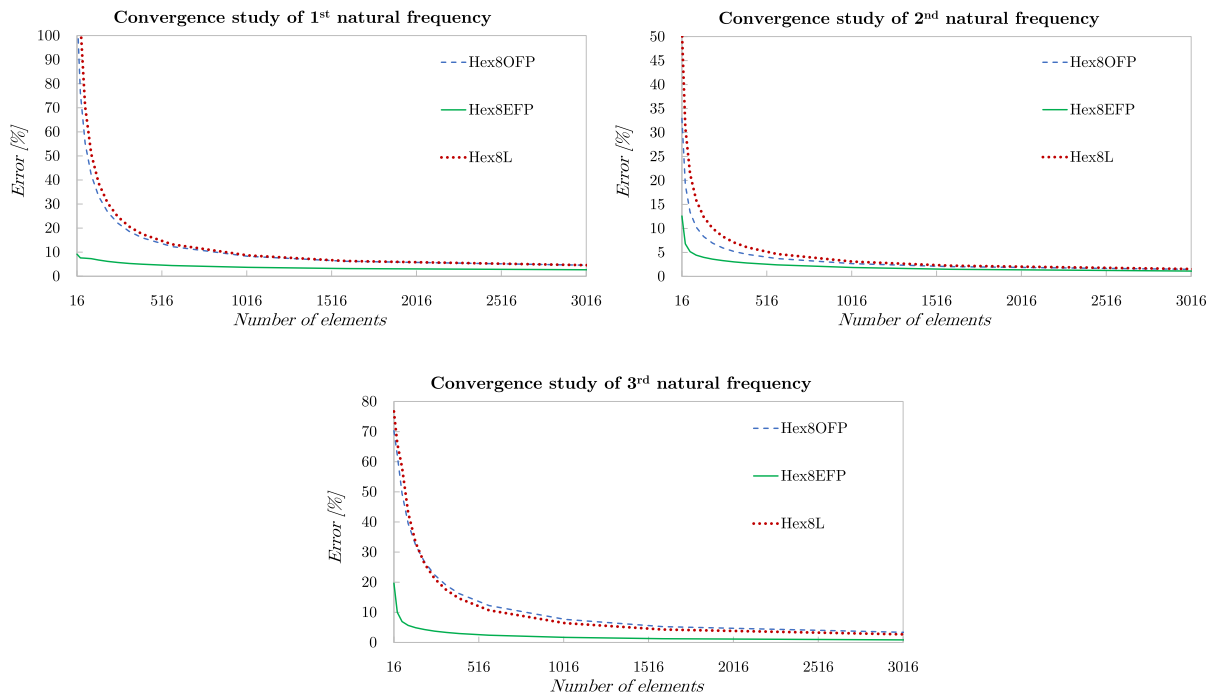


Figure 4.12: Convergence study of first three natural frequencies of CFFF plate (*ii*)

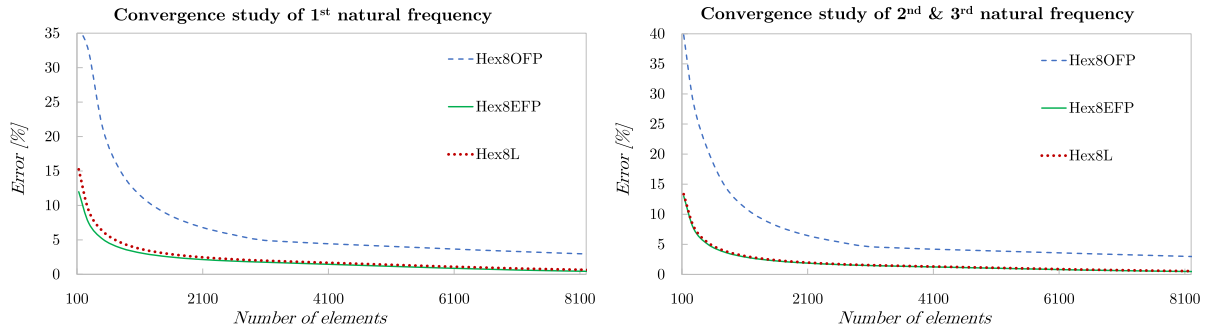


Figure 4.13: Convergence study of first three natural frequencies of CCCC plate with the circular hole (*iii*)

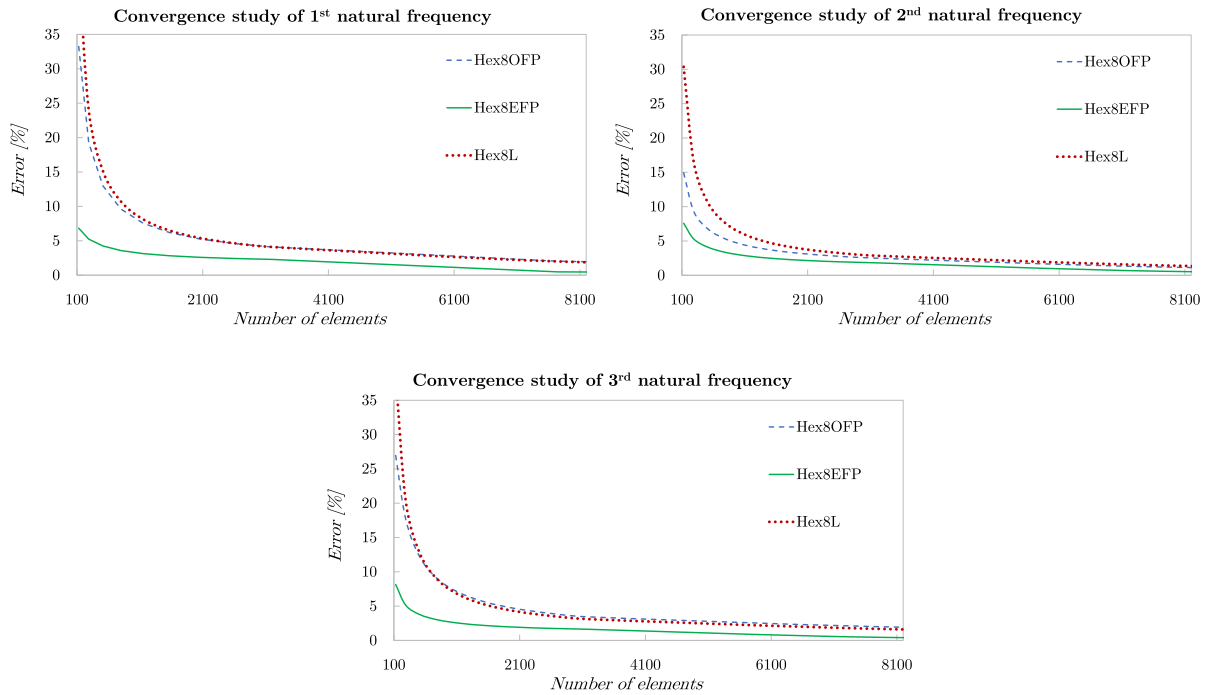


Figure 4.14: Convergence study of first three natural frequencies of CFFF plate with the circular hole (*iv*)

The results in Figures 4.11-4.14 largely show superior performance of the proposed elements against the elements with either Lagrangian or the original fixed-pole interpolation, the only exception being $2^{nd}/3^{rd}$ natural frequency for the CCCC plate (Figure 4.11), where *Hex8L* give better results, but only for the very coarse meshes. The best performance of *Hex8EFP* is observed in the first natural frequencies for the plates (*i*), (*ii*) and (*iv*), and in the second and third natural frequencies for the plates (*ii*) and (*iv*). For the plate (*iii*), the results of *Hex8EFP* and *Hex8L* are pretty close. However, the performance of *Hex8OFP* is the poorest and is not recommended for use.

4.2 Analysis of 2D micropolar continuum

4.2.1 Integral form of equations of motion

In order to develop a micropolar membrane finite element, the governing differential equations have been reduced from 3D to 2D continuum as shown in Chapter 2. The integral (weak) formulation, that follows from D’Alambert’s principle (4.1), is thus also reduced for the plane-strain condition. In this case there are only three degrees of freedom, i.e. two displacement (u_1, u_2) and one in-plane microrotation ϕ_3 , which represents a drilling (micro)rotation. Again, for approximation of both, the displacement field $\mathbf{u}^h = \mathbf{N}_u \mathbf{p}^e$ and the virtual displacement field $\bar{\mathbf{u}}^h = \mathbf{N}_u \bar{\mathbf{p}}^e$, the same enhanced fixed-pole interpolation is used (Bubnov-Galerkin approach), where the matrix of interpolation functions over an element is

$$\mathbf{N}_u = \left[\mathbf{N}_1 \quad \mathbf{0} \quad \dots \quad \mathbf{N}_m \quad \mathbf{0} \right] - \frac{1}{k} \hat{\mathbf{r}}_o \left[\mathbf{0} \quad \mathbf{N}_1 \quad \dots \quad \mathbf{0} \quad \mathbf{N}_m \right], \quad (4.27)$$

with the position vector $\mathbf{r}_o = \sum_{i=1}^m N_i \mathbf{r}_{o,i}$. The sub-matrices \mathbf{N}_i of the Lagrangian polynomials of order $k - 1$ are given as $\mathbf{N}_i = N_i \mathbf{I}$ for $i = 1, \dots, m$, where $m = k^2$ stands for the total number of nodes of each 2D finite element, while k represents the number of nodes along the element’s side. The microrotation and virtual microrotation fields have been interpolated by standard Lagrangian polynomials as $\phi^h = \mathbf{N}_\phi \mathbf{p}^e$ and $\bar{\phi}^h = \mathbf{N}_\phi \bar{\mathbf{p}}^e$ with $\mathbf{N}_\phi = \left[0 \quad N_1 \quad \dots \quad 0 \quad N_m \right]$. By introducing the chosen shape functions for the unknown fields, the equation of motion of a 2D micropolar finite element mesh with a non-standard real \mathbf{p}^e and virtual $\bar{\mathbf{p}}^e$ nodal degrees of freedom of an element with arbitrary chosen number of nodes m

$$\mathbf{p}^e = \left\langle \mathbf{p}_1^T \quad \mathbf{p}_2^T \quad \dots \quad \mathbf{p}_m^T \right\rangle^{eT}, \quad \bar{\mathbf{p}}^e = \left\langle \bar{\mathbf{p}}_1^T \quad \bar{\mathbf{p}}_2^T \quad \dots \quad \bar{\mathbf{p}}_m^T \right\rangle^{eT}, \quad (4.28)$$

with $\mathbf{p}_i^T = \left\langle \rho_{1i} \quad \rho_{2i} \quad \phi_{3i} \right\rangle^T$, $\bar{\mathbf{p}}_i^T = \left\langle \bar{\rho}_{1i} \quad \bar{\rho}_{2i} \quad \bar{\phi}_{3i} \right\rangle^T$, for $i = 1, \dots, m$, can thus be obtained as

$$\begin{aligned}
& \sum_{e=1}^{n_{el}} \bar{\mathbf{p}}^{eT} \left[\int_S \left[\left(\mathbf{B}_\rho^T - \frac{1}{k} \mathbf{B}_R^T + \left(\frac{k-1}{k} \right) \mathbf{B}_{I\phi}^T \right) \mathbf{C}_1 \left(\mathbf{B}_\rho - \frac{1}{k} \mathbf{B}_R + \left(\frac{k-1}{k} \right) \mathbf{B}_{I\phi} \right) \right. \right. \\
& \quad \left. \left. + \left(\mathbf{N}_\phi^T \mathbf{D}^T \right) \mathbf{C}_2 \left(\mathbf{D} \mathbf{N}_\phi \right) \right] dSt \mathbf{p}^e + \int_S \begin{bmatrix} \rho \mathbf{N}_u^T \mathbf{N}_u & \mathbf{0} \\ \mathbf{0} & \mathbf{N}_\phi^T \rho j \mathbf{N}_\phi \end{bmatrix} dSt \bar{\mathbf{p}}^e - \right. \\
& \quad \left. \int_S \left(\begin{bmatrix} \mathbf{N}_u^T \\ \mathbf{N}_\phi^T \end{bmatrix}^T \begin{Bmatrix} \mathbf{p}_v \\ \mathbf{m}_v \end{Bmatrix} \right) dSt - \int_S \left(\begin{bmatrix} \mathbf{N}_u^T \\ \mathbf{N}_\phi^T \end{bmatrix}^T \begin{Bmatrix} \mathbf{p}_s \\ \mathbf{m}_s \end{Bmatrix} \right) dS \right] = 0, \quad (4.29)
\end{aligned}$$

that is,

$$\sum_{e=1}^{n_{el}} \bar{\mathbf{p}}^{eT} (\mathbf{K}^e \mathbf{p}^e + \mathbf{M}^e \ddot{\mathbf{p}}^e - \mathbf{f}^e) = 0, \quad (4.30)$$

where \mathbf{K}^e , \mathbf{M}^e and \mathbf{f}^e are the element stiffness and mass matrix and external force vector of an element e , for $e = 1, \dots, n_{el}$, where n_{el} is the total number of elements in a mesh, t stands for the thickness of the finite element and \mathbb{A} is the finite-element assembly operator. The \mathbf{B} matrices of mutual dependence of the strains in the element with unknown degrees of freedom in the node in (4.30) are $\mathbf{B}_\rho = \begin{bmatrix} \mathbf{B}_{\rho 1} & \mathbf{0} & \dots & \mathbf{B}_{\rho m} & \mathbf{0} \end{bmatrix}$, $\mathbf{B}_R = \begin{bmatrix} \mathbf{0} & \mathbf{0} & \mathbf{B}_{R1} & \dots & \mathbf{0} & \mathbf{0} & \mathbf{B}_{Rm} \end{bmatrix}$, $\mathbf{B}_{I\phi} = \begin{bmatrix} \mathbf{0} & \mathbf{0} & \mathbf{B}_{I\phi 1} & \dots & \mathbf{0} & \mathbf{0} & \mathbf{B}_{I\phi m} \end{bmatrix}$, where $\mathbf{0}$ is a zero vector, while the sub-matrices in \mathbf{B}_ρ , \mathbf{B}_R and $\mathbf{B}_{I\phi}$ are

$$\mathbf{B}_{\rho i} = \begin{bmatrix} \frac{\partial N_i}{\partial x_1} & 0 \\ \frac{\partial N_i}{\partial x_2} & 0 \\ 0 & \frac{\partial N_i}{\partial x_1} \\ 0 & \frac{\partial N_i}{\partial x_2} \end{bmatrix}, \quad \mathbf{B}_{Ri} = \begin{bmatrix} \mathbf{r}_{x2i} \frac{\partial N_i}{\partial x_1} \\ \mathbf{r}_{x2i} \frac{\partial N_i}{\partial x_2} \\ -\mathbf{r}_{x1i} \frac{\partial N_i}{\partial x_1} \\ -\mathbf{r}_{x1i} \frac{\partial N_i}{\partial x_2} \end{bmatrix}, \quad \mathbf{B}_{I\phi i} = \begin{bmatrix} 0 \\ N_i \\ -N_i \\ 0 \end{bmatrix}, \quad (4.31)$$

while the matrix of differential operators \mathbf{D} given in (4.4) is also reduced for the 2D analysis. Again, it is important to note that the external loads should be determined according to the chosen interpolation functions when satisfying the finite element equilibrium equation. In other words, the external moments should be defined with the respect to the fixed-pole exactly as it has been shown in (4.29).

Remark 3 In [41], where a new quadrilateral Q_4 finite element with linked interpolation is presented, it is explicitly pointed out that it is necessary to apply the Petrov-Galerkin method, that

is, use different interpolations for test and trial functions in order to satisfy the convergence conditions. However, if the external load vector is interpolated correctly, the equilibrium of the finite element is reached without the application of the Petrov-Galerkin method.

4.2.2 Quadrilateral micropolar FE with four and nine nodes

For discretisation of the 2D micropolar continuum, quadrilateral finite elements with 4 and 9 nodes with three degrees of freedom per node have been chosen, where the proposed enhanced fixed-pole interpolation is used to interpolate the displacement field and Lagrangian interpolation for the rotational field. The mapping between the natural and global coordinate system is defined as [89] $\mathbf{x}^h = \sum_{i=1}^m N_i(\xi, \eta) \mathbf{x}_i^e$, where $\mathbf{x}_i^e = \begin{pmatrix} x_{1i}^e & x_{2i}^e \end{pmatrix}^T$ and x_{1i}^e, x_{2i}^e are the i^{th} node coordinates of an element. Figure 4.15 shows the numeration of nodes of both finite elements ($Q4$ and $Q9$) in the natural coordinate system. The Lagrangian polynomials for the quadrilateral element with four nodes $m = 4$ ($Q4$) are

$$N_i(\xi, \eta) = \frac{1}{4}[(1 + \xi_i \xi)(1 + \eta_i \eta)], \quad \text{for } i = 1, \dots, 4, \quad \text{where } \xi_i = \pm 1, \quad \eta_i = \pm 1,$$

Lagrangian polynomials for the quadrilateral element with nine nodes ($Q9$) are given as [89]

- Corner nodes:

$$N_i(\xi, \eta) = \frac{1}{4} \xi \eta (\xi + \xi_i)(\eta + \eta_i), \quad \text{for } i=1, \dots, 4, \quad \text{where } \xi_i = \pm 1, \quad \eta_i = \pm 1$$

- Mid-side nodes:

$$N_{i+4}(\xi, \eta) = \frac{1}{2} \eta (1 - \xi^2) (\eta + \eta_{i+4}), \quad \text{for } i=1,3, \quad \text{where } \xi_5 = \xi_7 = 0, \eta_5 = -1, \eta_7 = 1$$

$$N_{i+4}(\xi, \eta) = \frac{1}{2} \xi (\xi + \xi_{i+4}) (1 - \eta^2), \quad \text{for } i=2,4, \quad \text{where } \xi_6 = 1, \xi_8 = -1, \eta_6 = \eta_8 = 0$$

- Middle node:

$$N_9 = (1 - \xi^2) (1 - \eta^2).$$

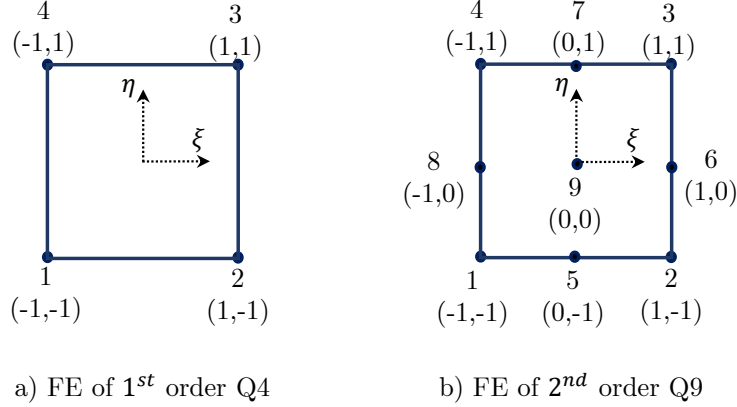


Figure 4.15: Quadrilateral finite elements with four and nine nodes in the natural coordinate system

The numerical integration has been used, while the set of basic algebraic equations for the whole system of elements, as well as the transfer of non-standard degrees of freedom to standard ones, have been obtained in an analogous manner to that shown earlier for the 3D analysis.

4.2.3 Numerical examples

A numerical analysis on a set of patch tests (one force patch test and three displacement patch tests [34]) has been performed to validate the newly presented micropolar 2D finite element *Q4EFP* which has been implemented into *FEAP* [127]. These numerical examples have been previously introduced in detail in the 3D micropolar continuum analysis and they are reduced for the planar analysis here. As mentioned earlier, the finite elements with the enhanced fixed-pole interpolation for the standard degrees of freedom ultimately yield the same stiffness matrix as the one with the linked interpolation. Therefore, the numerical results of these patch tests are the same as in [41], and there is no need to present them in detail here, but a few important notes are brought to the light.

On the other hand, the application of such a finite element formulation for the dynamic analysis of a planar micropolar continuum is not yet known. Therefore, a more detailed vibrational analysis is carried out here through four numerical examples.

4.2.3.1 Force patch tests

A force patch test has been performed on a planar cantilever subjected to a pure uniaxial distributed loading $p = 10N/m^2$. All geometrical (with the only dimension in the out-of-plane direction) and material properties are the same as in the equivalent force patch test for 3D

analysis, with the note that the parameter α does not manifest itself in the 2D analysis. The analytical results of all components of the stress and couple-stress tensors are equal to zero, except for the axial stress, which is equal to p . The finite elements $Q4EFP$ and $Q9EFP$ provide the analytical solutions only with the appropriate interpolation of the applied surface load as shown on the right side of (4.29). We note again that it is not necessary to use the Petrov-Galerking method, in contrast to the approach presented in [41].

4.2.3.2 Three displacement patch tests [34]

Providas and Kattis presented three separate patch tests for a complete validation of the micropolar finite element formulation, originally for 2D analysis. The patch tests have been performed on a rectangular domain discretised by five distorted finite elements, where displacements and microrotations are restricted in the external nodes (for details see [34,41]). The used material parameters are the same as those defined in the force patch test example.

The first test represents the state of constant symmetric stress and strain. Linearly varying displacements $u_1 = 10^{-3}(x_1 + 0.5 \cdot x_2)$ and $u_2 = 10^{-3}(x_1 + x_2)$ and constant microrotation $\phi_3 = 0.25 \cdot 10^{-3}$ have been imposed at the external nodes without any applied external load.

The second test represents the condition of constant non-symmetric stress and strain, where in contrast to the first test, the value of the constant microrotation is now $\phi_3 = 0.75 \cdot 10^{-3}$ and the constant body moment $m_{v3} = 1$ is also required.

Third test represents the state of constant curvature, where in addition to the linearly changing displacements applied in the outer nodes, as at the first two tests, the value of the microrotation $\phi_3 = 10^{-3}[0.25 + (x_1 - x_2)]$, the body moment $m_{v3} = 2(x_1 - x_2)$, and the constant body force $p_{vx1} = p_{vx2} = 1.0$ are applied. For the first two tests, the finite elements $Q4EFP$ and $Q9EFP$ satisfy the required criteria, while the elements for the high-order third patch test do not reproduce the exact results, but a relatively good agreement is obtained as in [41]. However, since our presented element can reproduce any state of constant stress, we can say that the element satisfies the convergence criterion.

4.2.3.3 Vibration analysis

A free vibration analysis on different numerical examples has been conducted:

- (i) Planar cantilever beam (CF) of length $L = 3.3$ mm and height $h = 0.165$ mm,

- (ii) Planar beam clamped on both sides (CC) with the same geometrical properties as in (i),
- (iii) Cantilever square plate with a central circular hole (CF) with edge-length $L = 3.3$ mm and radius of the hole $r = 0.33$ mm,
- (iv) Fully clamped circular plate of radius $R = 1.65$ mm with a central circular hole $r = 0.33$ mm,

while the thickness in all examples is taken as unity. The material properties are as in [47]: $G = 104$ MPa, $n = 0.44$, $N = 0.04$, $l_b = 0.33$ mm, $l_t = 0.62$ mm, $\Psi = 1.5$, $\rho = 2000$ kg/m³, $j = 5 \cdot 10^{-5}$ m², $J = \rho j = 10^{-1}$ kg/m, while their relation to the micropolar elasticity constants is described in (2.85). Schematic presentations of the geometries and FE discretisations of the square and circular plate with a hole in the middle are shown in Figure 4.16.

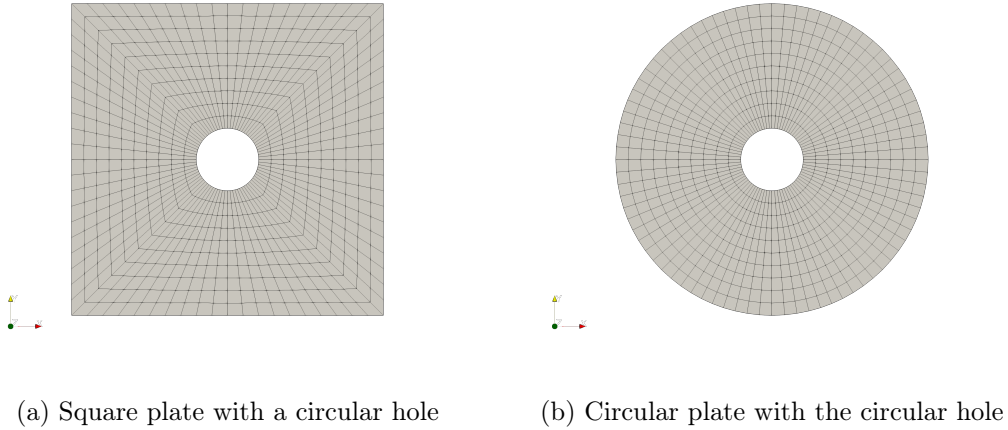


Figure 4.16: Schematic representation of discretisation in numerical example (iii) and (iv) with a mesh of 10x10 elements per each quadrant.

The present quadrilateral micropolar FE with four nodes $Q4EFP$ and also with nine nodes $Q9EFP$ have been used to discretise those geometries. The coefficient k appearing in the enhanced fixed-pole interpolation stands for the number of nodes along the element edge, i.e. $k = 2$ for $Q4EFP$ and $k = 3$ for $Q9EFP$. The numerical results have been also obtained using the original fixed-pole interpolation (elements $Q4OFP$ and $Q9OFP$ have $k = 1$) and the standard Lagrangian interpolation LI (elements $Q4LI$, $Q9LI$). Full numerical integration has been used, and the obtained convergence curves of the first three natural frequencies are shown in Figures 4.17 - 4.20. The reference solutions have been computed from FEM on very dense meshes, where the Lagrangian elements with 9 nodes have been used. The reference solutions for (i) and (iv) coincide with the numerical results from [47], which verifies the accuracy of the model, and based

on this we investigate the additional numerical examples (ii) and (iii) with different boundary conditions. The reference solutions for the first three natural frequencies for each numerical example can be found in the Table 4.5.

Table 4.5: Reference solutions for the first three natural frequencies (f_1 , f_2 and f_3) of all four considered numerical example.

Example	f_1 [kHz]	f_2 [kHz]	f_3 [kHz]
CF beam (i) [48]	1.59481	4.76076	7.61669
CC beam (ii)	3.75830	6.45379	9.73899
Square plate (iii) [48]	2.43085	3.96779	5.16320
Circular plate (iv) [48]	5.68080	7.54525	7.54525

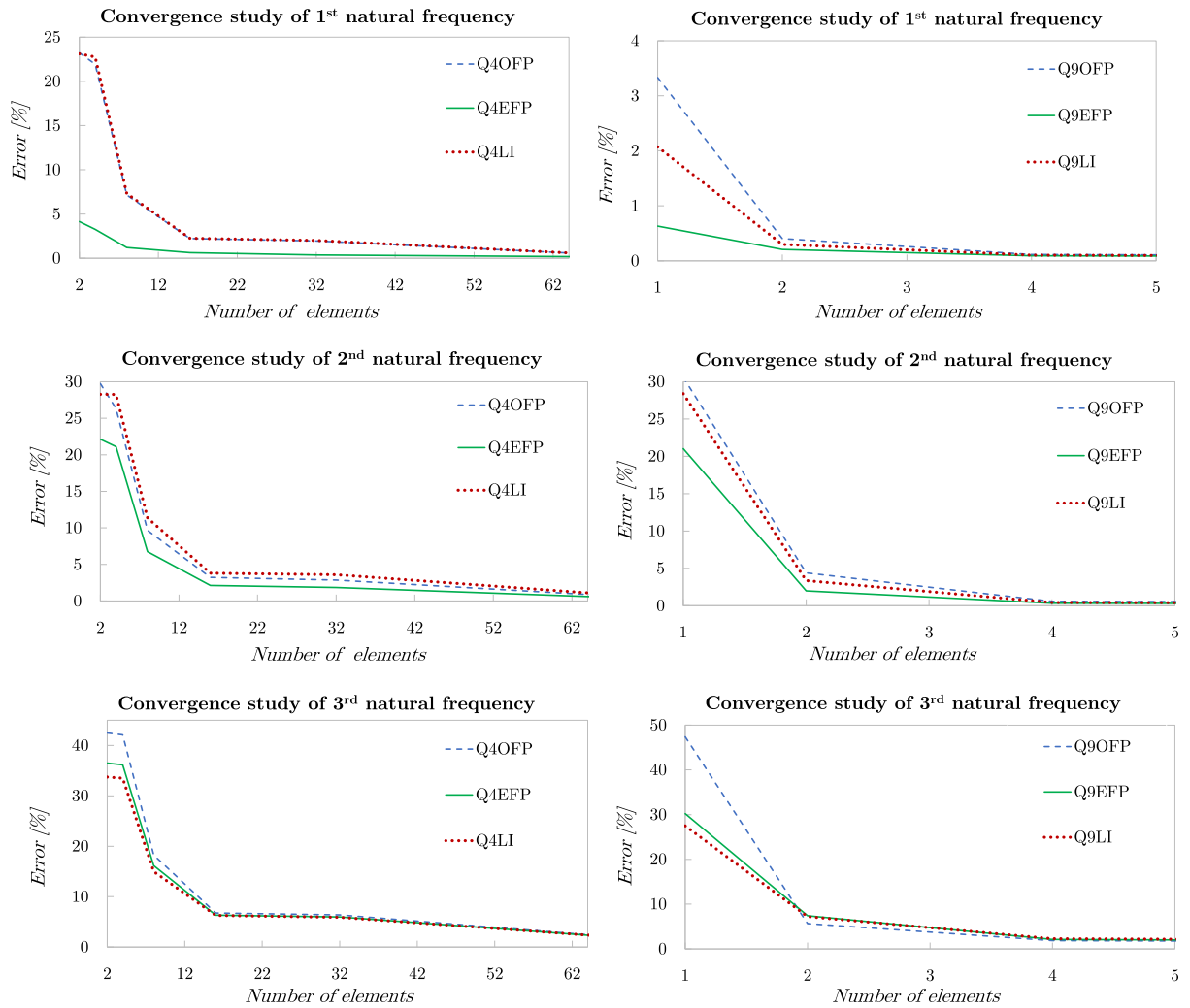


Figure 4.17: Convergence study of the first three natural frequencies for the cantilever beam (i): Q4 elements on the left, Q9 elements on the right.

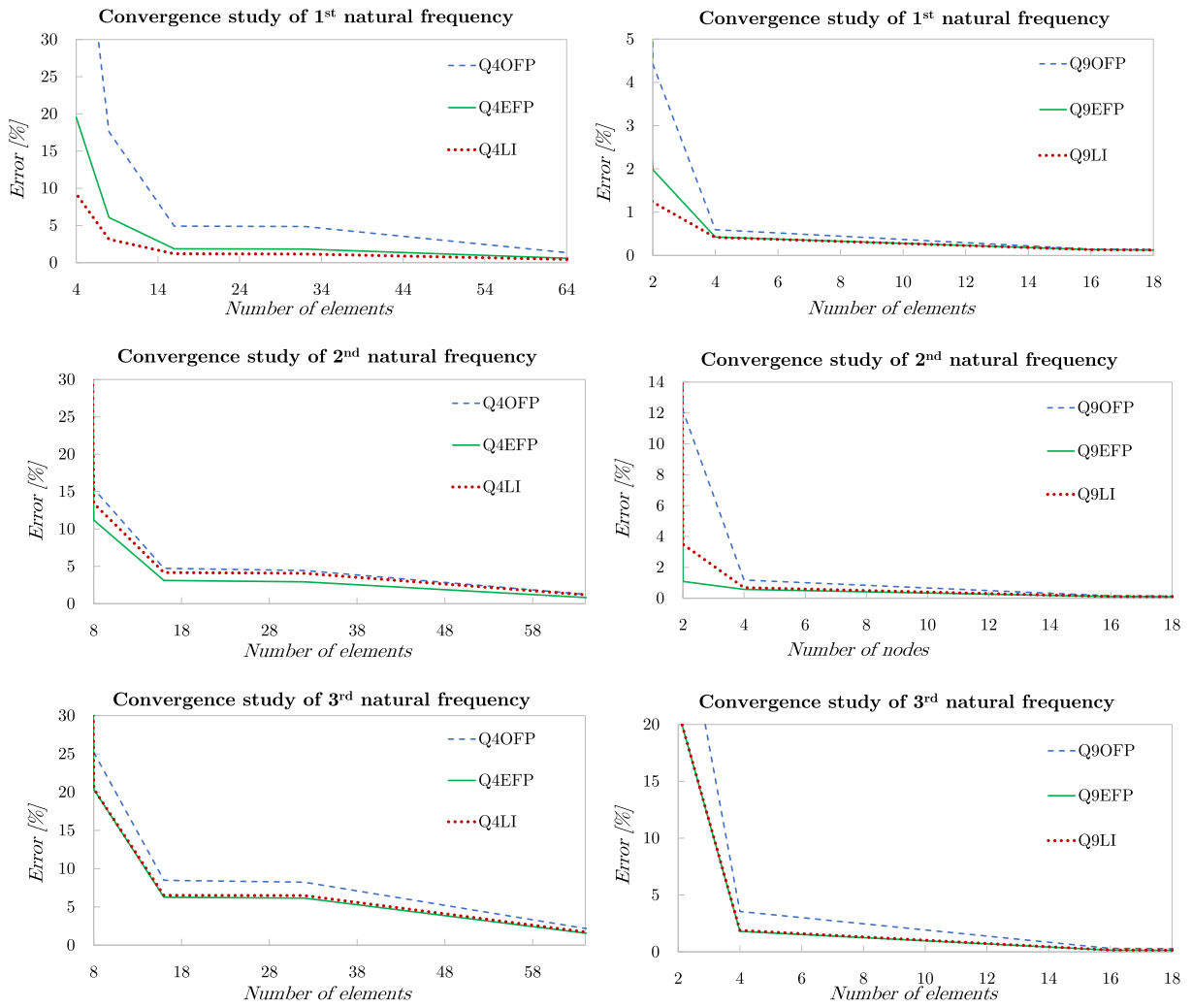


Figure 4.18: Convergence study of the first three natural frequencies for the fully clamped (ii): Q4 elements on the left side, Q9 elements on the right side.

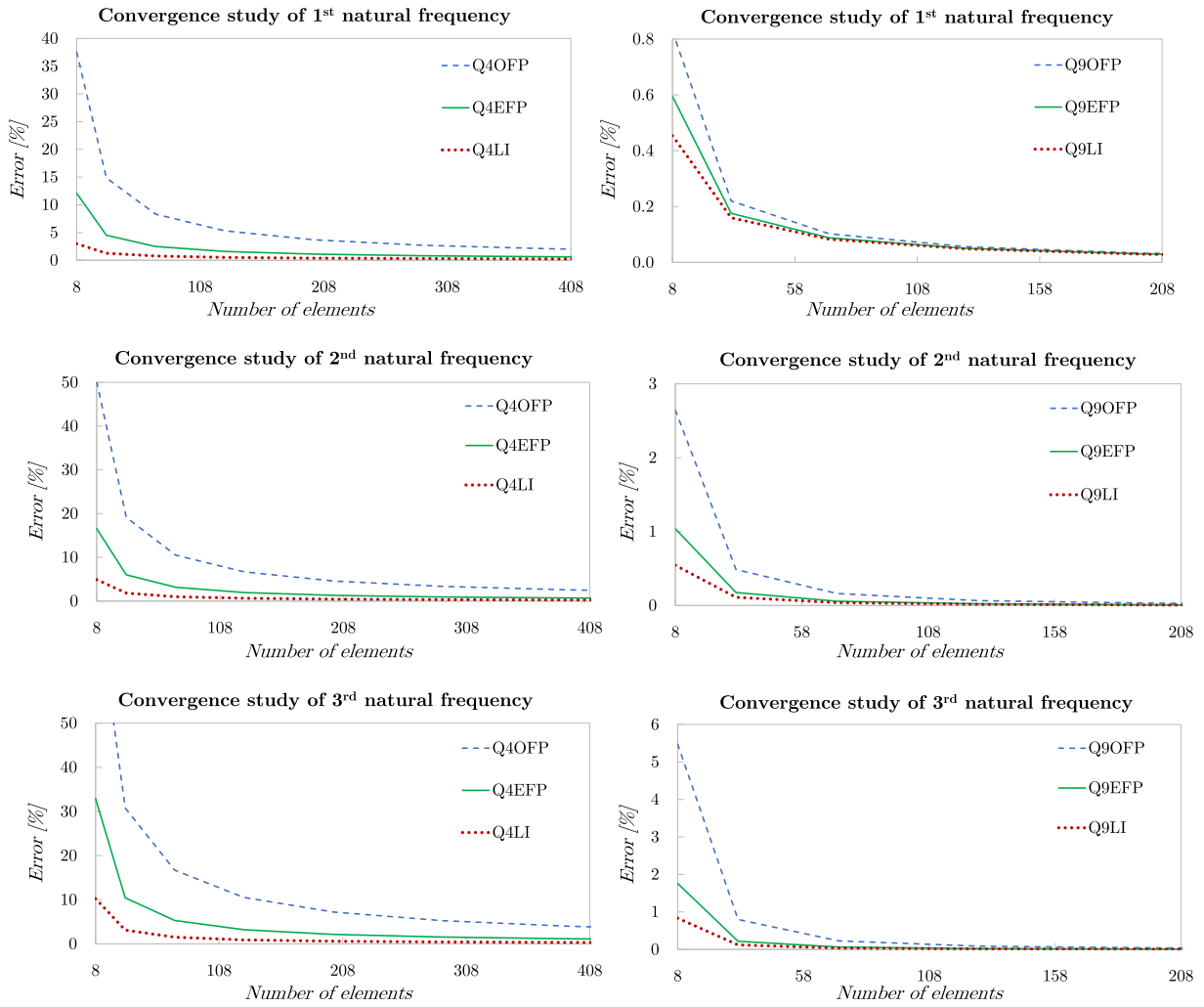


Figure 4.19: Convergence study of the first three natural frequencies for the cantilever square plate with a circular hole (iii): Q4 elements on the left side, Q9 elements on the right side.

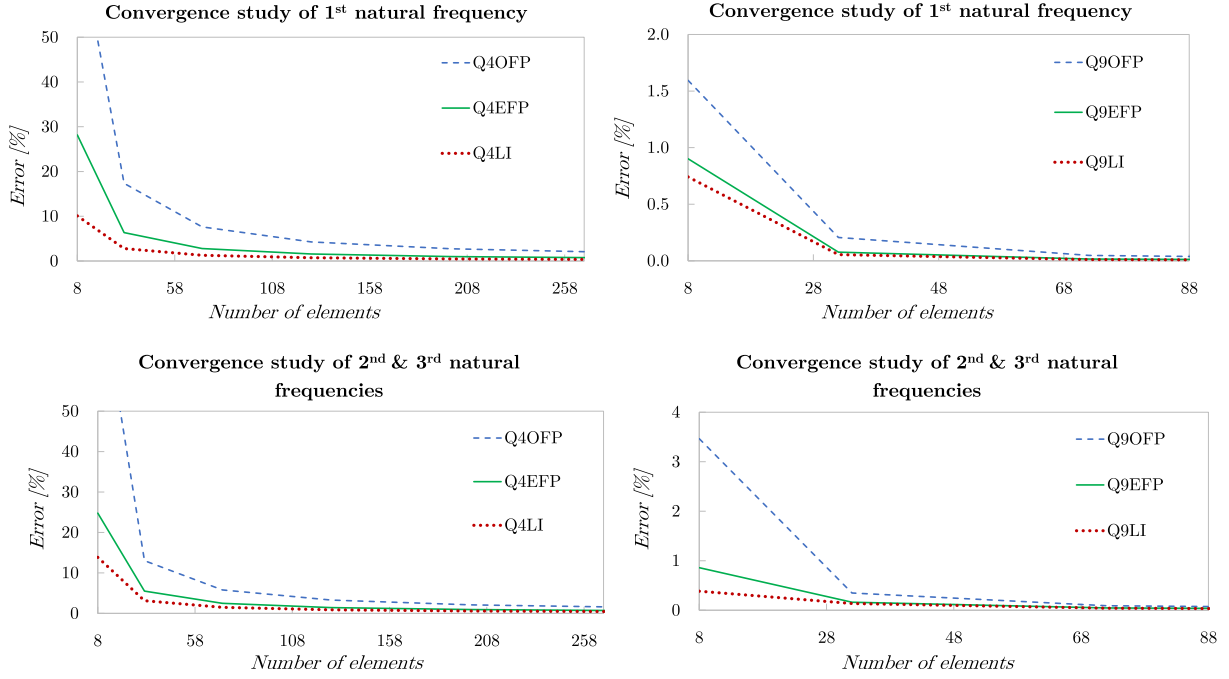


Figure 4.20: Convergence study of the first three natural frequencies for the circular plate with a circular hole (iv): Q4 elements on the left, Q9 elements on the right.

The convergence study of the first two natural frequencies of the planar beam (i) and (ii) clearly shows the efficiency of the elements $Q4$ and $Q9$ where the enhanced fixed-pole interpolation has been used. At the higher frequencies (shown here only for the third frequency, but the same has been observed for the fourth and fifth frequency as well) all three curves seem to match quite closely.

For the cases of the square and circular plate with a circular hole, we have somewhat unexpected results indicating that the Lagrangian interpolation provides the most accurate description for the first three modes for coarse meshes. For the mesh with only eight elements, the maximum error difference between the numerical results computed using $Q4LI$ and $Q4EFP$ elements for the first three eigenfrequencies is 22.65% for numerical example (iii) in the 3rd mode and 18.08% for (iv) in the 1st mode, while the maximum difference between $Q9LI$ and $Q9EFP$ elements is 0.93% for the 3rd mode of (iii) and 0.47% for the 2nd mode of (iv). However, these differences are significantly reduced as the finite element mesh becomes denser.

In contrast to the Timoshenko beam, the OFP interpolation does not improve of the results. Moreover, in all cases it gives either the same or worse results than the Lagrangian elements, which leads us to the same conclusion as before, i.e. that this type of interpolation should not be recommended for application in a micropolar continuum.

4.3 Conclusion

In this Chapter we have presented a new formulation of 3D finite elements of arbitrary order based on micropolar theory where the enhanced fixed-pole interpolation has been used. The newly presented eight-node hexahedral finite element has been tested through four standard patch tests, where the element has shown the ability to reproduce the constant stress condition. Two additional benchmark problems have been also analysed, comparing the numerical solutions with those obtained by the standard Lagrangian finite elements. It has been shown that the enhanced fixed-pole interpolation provides faster convergence to the analytical solutions, especially for the pure bending test.

The formulation has been reduced to the 2D micropolar continuum, which leads as to the same formulation as presented in [41], where the linked interpolation is used to interpolate the displacement field, while the virtual displacements are interpolated by the Lagrangian polynomials. Here, the Bubnov-Galerkin approach has been applied and it has been shown that such formulation passes the set of patch tests. Motivated by the good properties of the presented formulation in the linear static analysis, as well as in the dynamic analysis of beams, the fixed-pole approach has been also applied to the vibration analysis of the micropolar continuum.

The conducted numerical examples within the 3D micropolar continuum analysis clearly show the improvement, for the first two modes of the planar beam under the two considered boundary conditions. In the case of the 2D square and circular plate with a hole, it has been demonstrated that Lagrangian elements describe the first three modes for a very coarse mesh slightly better. But, for the next two to three increment steps of mesh refinement, the *Q4EFP* and *Q9EFP* elements provide nearly correct solutions.

Based on the presented results, the elements with the enhanced fixed-pole interpolation are sufficiently reliable and efficient for employing them in the inverse static analysis for the identification of micropolar material parameters. A comprehensive procedure for this will be outlined in the forthcoming chapters.

Chapter 5

Virtual experiments on perforated specimens

”A scientist in his laboratory is not a mere technician: he is also a child confronting natural phenomena that impress him as though they were fairy tales.”

Marie Curie

A reliable methodology for determining micropolar material parameters is crucial for its broader use. However, despite many investigations carried out, which have contributed significantly to its development [11,60] (see Section 1.4), it is still not uniquely established, even for the simplest possible (linear-elastic, isotropic and centrosymmetric) micropolar continuum described by six independent constants (see Section 2.4.1).

Building upon Gauthier’s pure bending problem [60] and inspired by the work of Beveridge et al. [130], our research group in the framework of *FIMCOS* project has suggested a simple methodology for capturing the characteristic length for bending of aluminium specimens with an artificially created internal structure of a regular pattern [71]. Instead of subjecting these specimens to the three-point bending (3PB) (as in [130]), the research group subjected them to four-point bending (4PB). In this way, the area of pure bending could be monitored, and for this purpose, strain gauges were used by attaching them on the top and bottom edges of the specimens at several characteristic positions. Furthermore, in contrast to the displacement measurement (as in [130]), the strain measurements in the pure bending area are not affected by shear deformations from the regions outside the pure bending area. This allowed a clear path for a proper comparison between the experiment and Gauthier’s analytical solution for the strains

of a homogeneous 2D micropolar continuum subjected to pure bending, leading to the proposed methodology for determining the characteristic length for bending and the homogenised Young’s modulus in [71].

Continuing from the previously conducted experimental investigations and the methodology for determining l_b , this Chapter proposes a method for identification of the remaining micropolar material parameter required for the analysis of the planar micropolar continuum – the coupling number N . The methodology for its determination based on a displacement calculation from a numerical virtual experiment is presented in Section 5.1. A comparison between the obtained value of the coupling number, as well as the reliability and accuracy of the methodology used for this purpose, with the alternative protocol proposed in the literature [130] is carried out in Section 5.2.

5.1 Capturing coupling number N – displacement calculation

5.1.1 Description of modelled specimens

To establish a methodology for capturing the coupling number N , we begin with a FE model of aluminium specimens for which the value of l_b was determined based on the laboratory experiments and with a help of Gauthier’s analytical solution. The geometry of the specimens and their internal structure were manufactured according to [130]. The internal structure of the specimens is artificially produced by drilling circular holes in a regular pattern within an aluminium alloy matrix. The geometry of the internal structure is defined with a hole radius $r = 3.5$ mm, a vertical pitch $P_2 = 12.7$ mm, and a horizontal pitch $P_1 = 16.0$ mm. Figure 5.1 shows the geometry of the internal structure of the specimens and demonstrates three possible representative cells (among others) outlined by dashed lines. The green line represents a rectangular cell, the blue one is a honeycomb cell and the red one is a triangular cell. To ensure complete isotropy of the specimens, the rectangular unit cell should ideally be square, as for instance demonstrated in [131] (where the authors identified the material parameters for metamaterial beam specimens based on micromorphic theory). In that situation, it would be perfectly correct to compare the experimental results with Gauthier’s analytical solution of an isotropic micropolar beam subjected to pure bending. Here, the specimens are slightly orthotropic, but it is convenient to use the isotropic elasticity as an approximation (as also done in [130], whose results we will use for comparison).

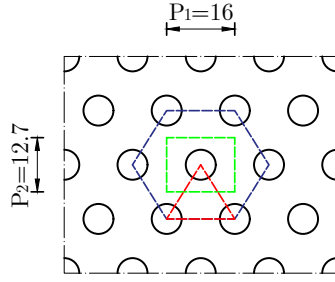


Figure 5.1: The geometry of internal structure for the analysed specimens, following [130].

To capture the *size-effect* anticipated here, four types of specimens have been investigated, distinguished by the number of rows of holes within their matrix. Thus, the specimens with a single row of holes are denoted as B1-*i*, those with two rows are denoted as B2-*i*, and similarly for B3-*i* and B4-*i* (shown in Figure 5.2), where *i* represents the specimen number $i = 1, 2, 3, .$ The dimensions of the beam-like specimens are given in Table 5.1 for each specimen type, where *L* stands for the length of the specimen, *h* for the height, and *w* for the width.

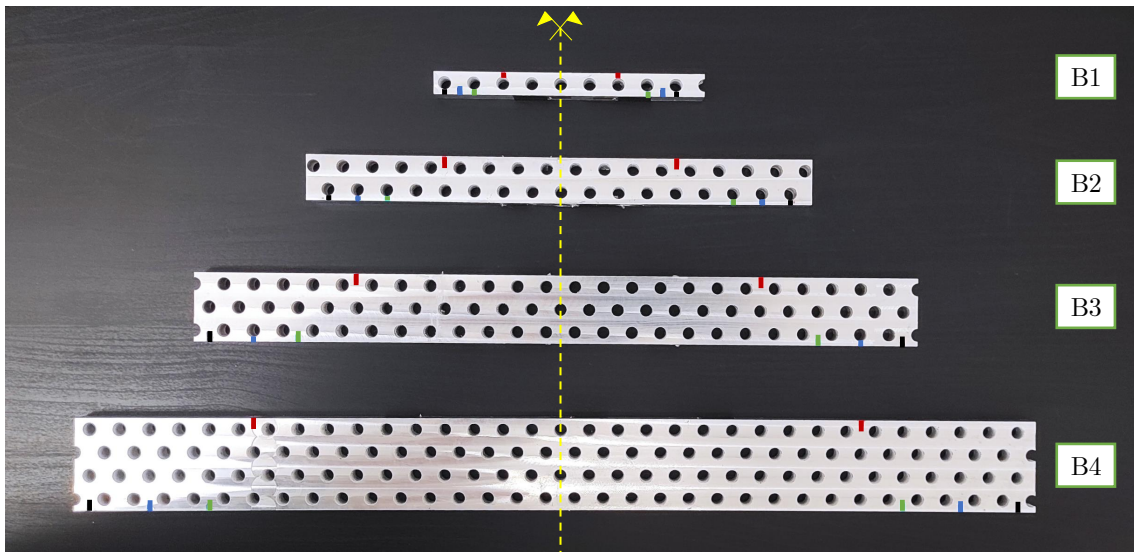


Figure 5.2: Perforated specimens B1-B4 with marked positions of applied forces and supports.

Table 5.1: Dimensions of beam specimens [mm] [130].

Beam	<i>L</i>	<i>h</i>	<i>w</i>
B1	150	12.7	12.7
B2	280	25.4	12.7
B3	400	38.1	12.7
B4	530	50.8	12.7

5.1.2 Set-up

The coupling number is a micropolar material parameter that influences shear stresses and affects the amount of their non-symmetry (see Eq. (2.90)). Therefore, the key to its determination lies in the shear stresses that occur outside the pure bending area in the 4PB test, within the region between an applied concentrated force and its nearest support. The shear in the 4PB does not have any effect on the strain computation in pure bending area, but it has an impact on the displacements. Consequently, the detection of the coupling number is based here on calculated displacements (from a virtual experiment). The 4PB virtual set-up is thus based on [71], but the locations of the concentrated forces and the points of the supports have been selected differently. Additional attention has been directed towards two aspects:

- (i) Symmetry of the specimen geometries does not align with the symmetry of the created internal structure for specimens B1 and B4 (this can be observed in Figure 5.2 if the left and right edges of these specimens are compared). Hence, the symmetry axis of the internal structure is exactly midway between the beam supports and the concentrated forces.
- (ii) The positions of applied forces and the supports are set directly above/below the centre of the nearest hole or above/below the centre of the solid aluminium matrix between two holes, in order to better control the stress distribution. This also applies to the positions where displacements have been measured.

In order to identify the coupling number, three set-up conditions have been considered in which the influence of shear, which is known to affect it, is varied: In the first, the supports are almost at the edge of the specimens (indicated by the black marker on the specimens shown in Figure 5.2), while in the second and third setups the supports approach the centre of the specimens labelled with blue and green markers in Figure 5.2, respectively. Tables 5.2 and 5.3 list the support positions of each specimen type in terms of the value a_i , which represents the distance from the edge of the specimen to the support, and f_i , which is the distance between the two supports, for all three setups $i = 1, 2, 3$ (see Figure 5.3). It is conveniently chosen to keep the $\frac{f_i}{h}$ ratio constant for all specimen types in each individual experimental set-up i , that is $\frac{f_1}{h} = 10.08$, $\frac{f_2}{h} = 8.82$ and $\frac{f_3}{h} = 7.56$.

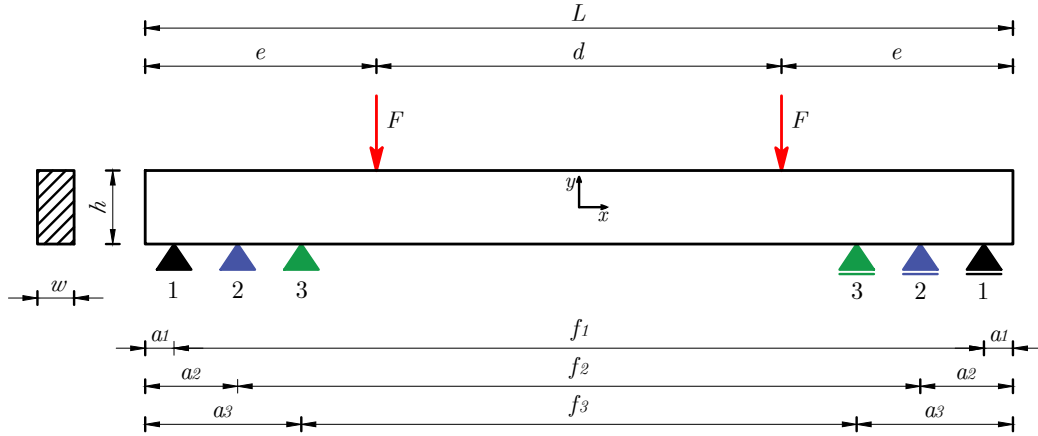


Figure 5.3: Set-up of HMD specimens subjected to the four-point bending.

Table 5.2: Positions of supports for specimens B1 and B4 (the specimens with different symmetry axis of geometry and internal structure) [mm].

Specimen	1 st set-up		2 nd set-up			3 rd set-up			
	a_1 left	a_1 right	f_1	a_2 left	a_2 right	f_2	a_3 left	a_3 right	f_3
B1	6	16	128	14	24	112	22	32	96
B4	8	10	512	40	42	448	72	74	384

Table 5.3: Positions of supports for specimens B2 and B3 [mm].

Specimen	1 st set-up		2 nd set-up		3 rd set-up	
	a_1	f_1	a_2	f_2	a_3	f_3
B2	12	256	28	224	44	192
B3	8	384	32	336	56	288

Each concentrated force F is applied at a distance e from the edge of the specimen, with a spacing d between the two applied forces (Table 5.4 and 5.5). The values of the applied force F on each specimen type (Table 5.4 and 5.5) is taken from [71] where it was computed that will not exceed the elastic limit. The value of the chosen applied force in the virtual experiment is important here because if we manage to establish a methodology for identifying the coupling number based on the displacement calculation, we would extend the identical procedure to laboratory experiments in the future work (where the displacement measurements could be monitored using LVDTs and/or non-contact optical equipments). These laboratory experiments would remain within the linear-elastic area, and their results could be directly compared with

those presented here.

Table 5.4: The values of the maximum applied forces F [kN] on specimens B1 and B4 and the positions of their application [mm].

Specimen	F	e left	e right	d	g left
B1	0.9	38	48	64	38
B4	2.5	96	98	336	136

Table 5.5: The values of the maximum applied forces F [kN] on specimens B2 and B3 and the positions of their application [mm].

Specimen	F	e	d
B2	1.4	76	128
B3	2.0	88	224

5.1.3 Virtual-experiment procedure

The virtual experiments have been conducted to simulate 4PB laboratory tests on specimens, where their internal structure defined in regular pattern has been incorporated into the geometry of the finite element model. The open-source software Gmsh 3.0.5. [132] has been used for modelling the geometry of the specimens and their discretisation with a mesh of quadrilateral finite elements. The exact coordinates of the nodes where the boundary conditions and concentrated forces will be applied have been defined in this step (according to Tables 5.2-5.5). Each specimen has been discretised using a highly dense mesh, and the total number of finite elements for each specimen's model is given in Table 5.6. A visual demonstration of the finite element mesh density is shown in Figure 5.4 for a representative cell.

Table 5.6: The total number of finite elements for each type of model.

Specimen's type model	Number of FE
B1	15 304
B2	41 694
B3	64 000
B4	93 678

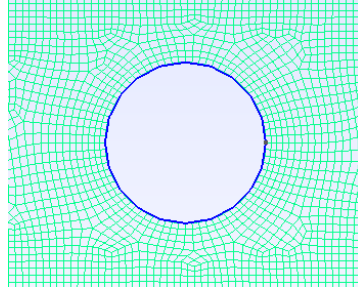


Figure 5.4: The schematic representation of finite element mesh density for a unit cell.

An own-developed short Python code has been used to adjust the mesh input data for FEAP programme [127]. The concentrated forces and the boundary conditions (for simply supported beam) have been defined in the corresponding nodes at the top and bottom edge of the model, respectively. The constitutive description for this planar model has been defined as a plane-stress state. However, it is worth noting that in the laboratory conducted experiments, the applied load jacks prevented anti-clastic curvature in the cross-section of the specimens, which to a very small extent represents the plane-strain condition. The material parameters for the aluminium matrix have been introduced as $E = 72.4$ GPa and $\nu = 0.3$. The numerical analysis has been then performed using classical quadrilateral finite elements (originally integrated in FEAP). Due to the irregular node number ordering stemming from the mesh generator in the Gmsh programme, and the large number of finite elements in the model, the command *OPTIMIZE* in FEAP has been additionally used to optimize the number ordering of the unknowns [127]. This significantly reduced the time required to solve the algebraic system of equations, resulting in a significant reduction in the numerical computational time from one hour (on average) to only a few minutes. The numerical results for the vertical displacement fields of models B1-B4 have been plotted using the open-source software ParaView 5.0.1., which are shown in Figures 5.5-5.8.

Note: The heterogeneous material of the HMD specimens (which consists of an aluminium alloy matrix and voids, i.e. air) has a clearly visible internal structure at the macroscopic level, defined by a controlled pattern. Such a geometry of the internal structure can be easily integrated within a classical FE model (to perform virtual experiments). However, it could become more complicated if these voids are randomly arranged. In such a case, the specimen could be scanned optically, and the geometry of the inner structure could be defined computationally, which could then be incorporated into the FE model. Additionally, if this random internal structure gets smaller up to the micro-scale (e.g. for bones), implementing such a methodology for verification of the classical FE model with experimental results is a big challenge.

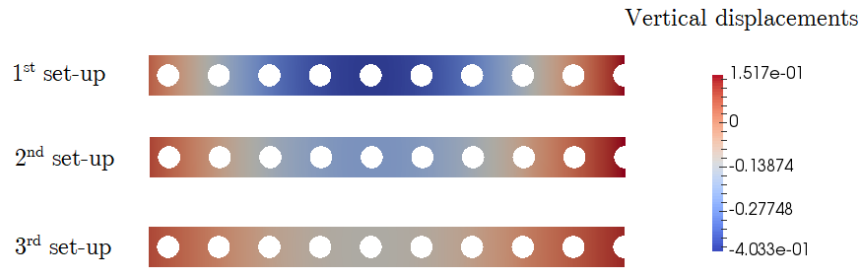


Figure 5.5: Plotted numerical results for vertical displacement field of B1 model [mm].

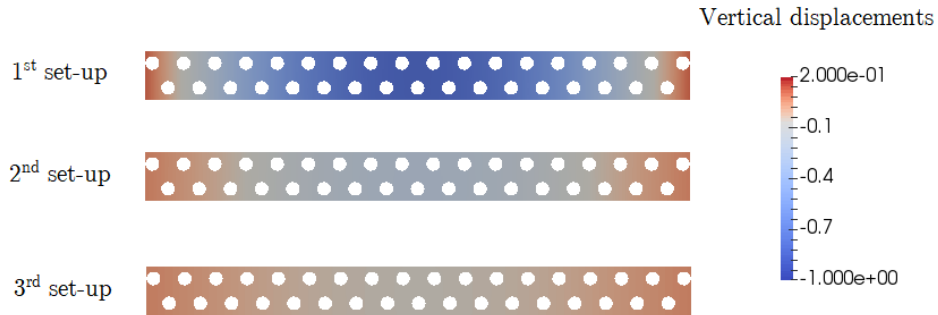


Figure 5.6: Plotted numerical results for vertical displacement field of B2 model [mm].

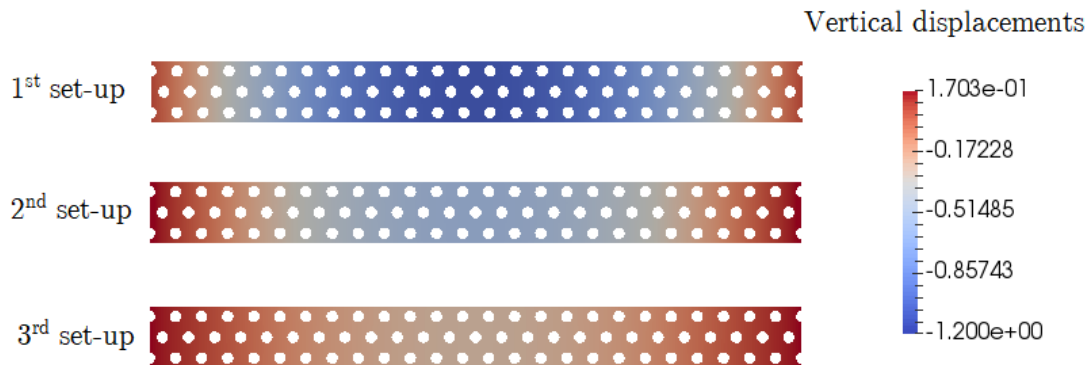


Figure 5.7: Plotted numerical results for vertical displacement field of B3 model [mm].

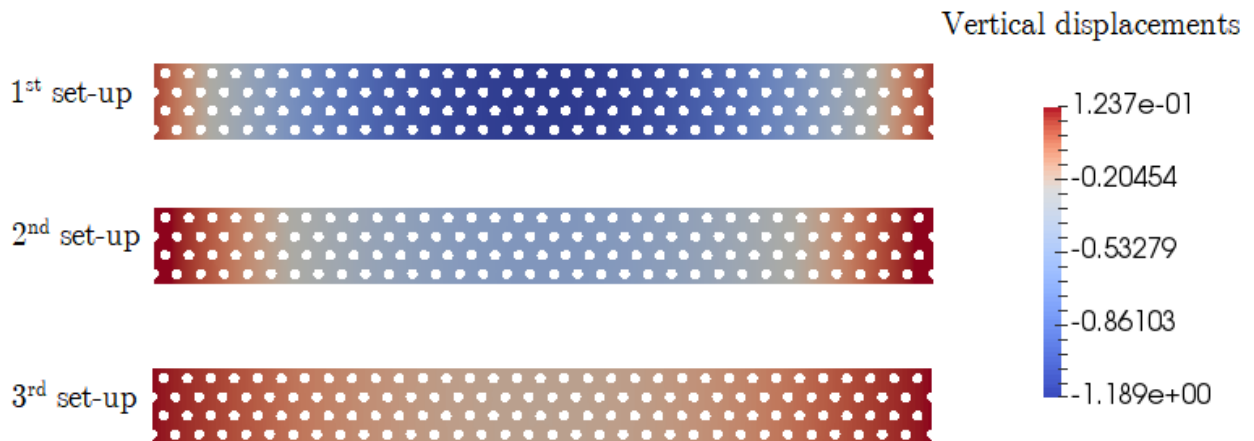


Figure 5.8: Plotted numerical results for vertical displacement field of B4 model [mm].

5.1.4 Inverse numerical analysis

The specimens can also be modelled without voids as a homogenised micropolar continuum, with captured influence of the internal structure on their behaviour through micropolar constitutive equations. For the plane-stress analysis the model requires the values of four material parameters (see Eq. (2.90)), three of which are already known from [71] for these specimens: $E = 42.37$ GPa as a homogenised Young's modulus, $l_b = 2.45$ mm, and $n = 0.3$, while the coupling number is still unknown point and needs to be determined. The geometry of all specimen types (without voids) is discretised again in the FEAP programme, but now with a regular dense mesh of newly developed quadrilateral micropolar finite elements $Q4EFP$. The boundary conditions, the values of the applied concentrated forces and their application points are the same as in the virtual experiment. Through an iterative process, we seek the value of the coupling number that gives the identical numerical results of the vertical displacements in the homogenised micropolar model as the results from the virtual experiment on modelled specimens using the classical FE, shown in Table 5.7 for the considered profiles. Of course, it is necessary to obtain a unique value of N for all types of the models and different setups. In order to properly compare the displacement results of the classical model with the homogenised model, all vertical displacements along several characteristic profiles P of each specimen type (defined in Figure 5.9) have been considered. These profiles are located approximately at the mid-span of the models (sufficiently far away from the locations of the concentrated forces/reactions) to ensure that the displacement values are not affected by local effects. The considered profiles have a thickness of 0.25 mm and all displacements at the nodes within each profile are averaged.

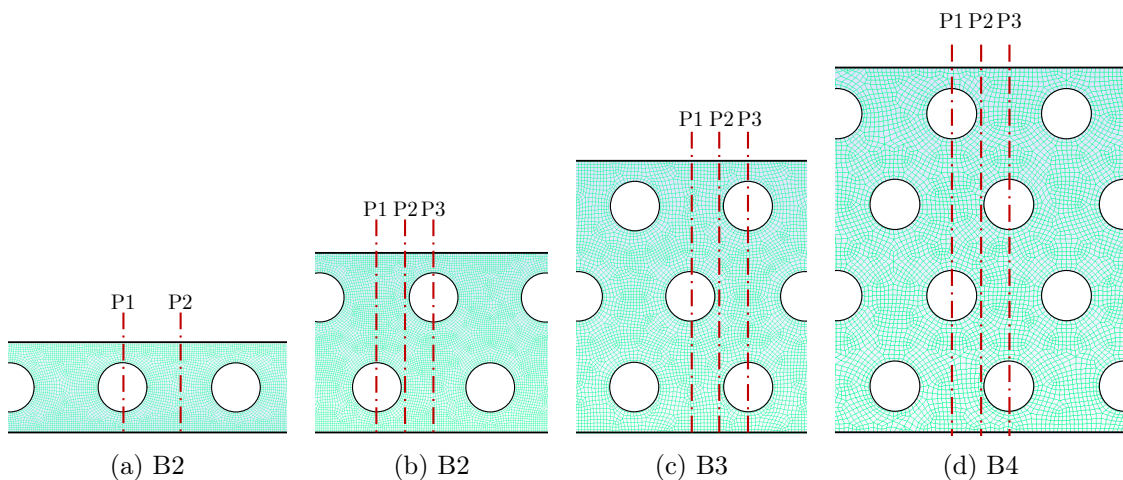


Figure 5.9: Characteristic profiles P for calculating the average displacements.

The coupling number has been captured by an inverse analysis for each considered profile of all four model types, which provides the average results for the displacements of the homogenised model identical to those listed in Table 5.7 and obtained by the virtual experiment (model based on the classical theory of elasticity). Subsequently, the average value of the coupling number for all the model types has been determined for each individual experimental set-up, which is shown in Table 5.8. It is interesting to note that the value of the coupling number is higher when the specimen size decreases and it is also higher for a smaller $\frac{f}{h}$ ratio, that is, as the shear becomes more pronounced compared to the bending. However, keep in mind that this is a material parameter that should not depend on the boundary conditions or the applied loads, i.e. that it is a constant.

Based on the obtained values of the coupling number, we see a large deviation between different set-ups and different model types, which indicates its sensitivity. As the shear becomes more pronounced in comparison to the bending (3^{rd} set-up), the coupling number becomes more prominent and the dispersion becomes somewhat milder. In order to find a constant of that material parameter, a linear regression of average values of N has been performed.

Table 5.7: The average values of the vertical displacements computed from the virtual experiments on classical models B1-B4 for each characteristic profile.

		Average values of vertical displacements [mm]		
Model type	Profile	1 st set-up	2 nd set-up	3 rd set-up
B1	P1 (middle)	-0.40242	-0.23968	-0.12459
	P2	-0.39749	-0.23601	-0.12195
B2	P1 (middle)	-0.83777	-0.49799	-0.25548
	P2	-0.83706	-0.49746	-0.25513
	P3	-0.83427	-0.49537	-0.25374
B3	P1 (middle)	-1.10536	-0.61262	-0.26978
	P2	-1.10513	-0.61246	-0.26968
	P3	-1.10372	-0.61148	-0.26912
B4	P1 (middle)	-1.18764	-0.59556	-0.19927
	P2	-1.18758	-0.59553	-0.19924
	P3	-1.18653	-0.59487	-0.19894

Table 5.8: Determined values for the coupling number and its average for each set-up.

Set-up	$\frac{f}{h}$	Model type	$1/h^2$	Obtained N	Average value of N
1 st	10.08	B1	0.0062	0.0850	0.041
		B2	0.0016	0.0418	
		B3	0.0007	0.0216	
		B4	0.0004	0.0145	
2 nd	8.82	B1	0.0062	0.0950	0.047
		B2	0.0016	0.0471	
		B3	0.0007	0.0230	
		B4	0.0004	0.0228	
3 rd	7.56	B1	0.0062	0.0960	0.053
		B2	0.0016	0.0602	
		B3	0.0007	0.0280	
		B4	0.0004	0.0285	

Observing the extending situation when the shear becomes more and more pronounced, when $\frac{f}{h} \rightarrow 0$, we obtain the calculated coupling number $\mathbf{N=0.091}$, which represents the material constant of the internal structure (Figure 5.10).

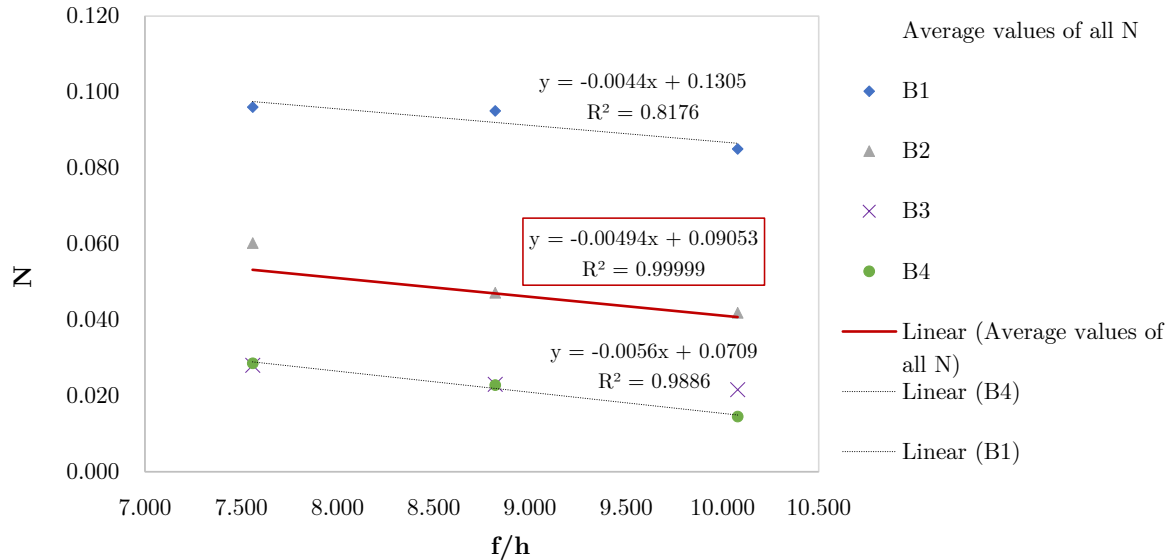


Figure 5.10: Coupling number obtained from the inverse analysis based on the virtual experiment, and their linear regression.

Moreover, the B1 models show the highest dispersion of the calculated N values for each

individual experimental setup from the average. If we consider Figure 5.2, we can see that the positions of the applied concentrated forces on B1 are relatively close to the considered displacement profiles, which makes us wonder if local influences also play a role in this. The considered profile P2 of model B1 also differs from the profile P2 of the other model types (see Figure 5.9).

5.2 Discussion

In order to assess the reliability of the proposed methodology and the accuracy of the obtained coupling number, we rely on a comparison with a somewhat different approach of [39], which inspired this research. Let me first briefly describe their procedure for determining the coupling number [39]:

1. The analysis was based on the virtual experiment on the models simulating perforated specimens with an aluminium matrix with material properties of $E = 70.0$ GPa and $\nu = 0.3$ and with the same beam and internal structure geometries as ours. The simulation of 3PB was conducted, and to compute the stiffness, the applied force was divided by the average value of all calculated vertical displacements at the nodes located at the mid-profile.
2. In the second step, they considered the specimens as a homogenised linear and isotropic micropolar model discretised by micropolar finite elements based on the control volume formulation [133]. As input, they used the values of the Poisson ratio for aluminium, the characteristic length for bending and the homogenised Young's modulus, where the last two parameters were obtained from the 3PB laboratory experiments and the analytical solution. The remaining required micropolar material parameter N is identified by inverse analysis in a slightly more automated manner than shown here. They provided a code that fully automatically searched for the value of N that gave the same stiffness of the micropolar model as obtained from the virtual experiment. In their code, they started from the setup of the model with the smallest ratio $\frac{f}{h} = 5.04$ and obtained the value of the coupling number $N = 0.112$ for this situation, which had the biggest possible coefficient of determination $R^2 = 0.93$ for all four specimen types B1-B4. However, when they applied the same parameters to the other experimental considered setups, they obtained much larger deviations in the stiffness values of their homogenised model and the virtual experiment. In Figure 14 in their work [39], it can be seen for the largest range that even

with the highest possible value, the desired stiffness cannot be achieved.

3. This encouraged them to update the previously obtained values of the homogenised elastic modulus and the characteristic length for bending through a parameter that depended on these two parameters, while the value $N = 0.112$ was fixed. In this way, they obtained the final parameters: the homogenised elastic bending modulus $E^* = 39$ GPa, $l_b^* = 10.14$, which corresponds to $E = 42.86$ and $l_b = \frac{l_b^*}{\sqrt{24(1-n)}} = 2.47$. These values were in very good agreement with those obtained in [71], i.e. $E = 42.37$ GPa and $l_b = 2.45$ (for a detailed comparison and explanation of the two notations used in the micropolar community for the characteristic length l_b^* and l_b see [71]).

Considering that they obtained micropolar material parameters close to those in [71] for $N = 0.112$, it has been expected that the obtained N here should also be approximately the same as theirs. However, the obtained value is $N = 0.091$, and this difference of 18.75% seems quite significant.

However, we should bear in mind that Figure 5.10 shows some deviation between the average values of the coupling number between the two boundary model types. On the other hand there is also a note in [39]: "For the $\frac{f}{h} = 10.08$ case it is interesting to note that reducing N significantly from 0.9 to 0.112 results in a reduction in stiffness of less than 10% for the smallest sample. The influence of N on the size-effect is less significant and the distinction between the micropolar and couple stress cases is less pronounced.", which is the likely reason why they chose $N = 0.112$ from the first iteration and carried it over to the second iteration, where they fixed the other two material parameters that play a more significant role. In order to perform a preliminary test on specimen B4 for all three experimental setups, it has been investigated how much the change of N affects the difference between the results of the homogenised model and the virtual experiment. For the case of $N = 0.112$, there is a very small average difference of 0.2%. At least in two characteristic profiles we have been considered here, and these profiles are not located at the place where a concentrated force is applied, which could locally affect the displacements in nearby points of this profile, as in [39].

However, based on obtained results we conclude that in future work it would be better to conduct the identification of the coupling number according to the virtual experiment based on pure shear problem.

Chapter 6

Experimental investigation of plates with circular hole under tension

”An experiment is a question which science poses to Nature and a measurement is the recording of Nature’s answer.”

Max Planck

The Meaning and Limits of Exact Science (1949.)

The conducted investigation and results presented in this Chapter are also shown in: [134] Grbac, L., Jelenić, G., Čeh N., "Axially loaded strip with circular hole – assessment of predictive capacity of micropolar continuum theory", submitted to Journal of Mechanics of Materials and Structures, 2023.

Discontinuities in shape and size are a common appearance in structural elements or individual parts of mechanical systems (such as gears or cylinders). In such cases, the stress values and their distribution along the cross-section in the vicinity of areas where the cross-sectional geometry changes due to notches, cut-outs, or locations where a concentrated force acts, differ significantly from the stress distribution that occurs in a cross-section without discontinuities. This localised occurrence of higher stress values is called stress concentration and is quantified by *the stress concentration factor*. The stress concentration factor is defined as the ratio between the maximum stress at the edge of the discontinuity and the average (nominal) stress value [30]. It is of great importance for engineers to accurately calculate the value of stress concentration because cracks can occur and propagate at these locations, which could ultimately lead to the

collapse of the structure if it is not properly designed. Therefore, it is not surprising that engineers have been analysing the stress concentrations stemming from various causes for more than a century (comprehensive research on stress and strain concentration factors in many cases can be found in [30]).

This part of the thesis is specifically focused on the simplest example: a stress and strain distribution around a circular hole in a homogeneous plate subjected to uniaxial tension. In the first part of this Chapter, we shed light on observations from previous research in the literature, revealing the gap between experimental results and solutions based on the classical theory, even in linear analysis. These discrepancies motivate us to investigate whether the classical theory of elasticity can accurately describe the studied problem in Section 6.2, which describes the experimental campaign, and in Section 6.3, which provides numerical results based on the classical theory and their comparison with the experimental results. In Section 6.4, we embark on a quest for a more accurate theoretical prediction, where the micropolar theory is employed as a candidate theory in parametric and inverse numerical analysis aimed at providing suitable micropolar parameters that give the numerical results which should correspond to those obtained experimentally. The final assessment of the micropolar theory's predictive capacity for the considered problem is provided in Section 6.5.

6.1 Motivation: Why is stress concentration factor based on classical theory doubtful?

The problem of stress concentration (increase in a nominal stress) near a circular hole in a symmetric uniaxially loaded elastic plate is very well-studied theoretically (see e.g. [30, 128, 135–140] and the references therein), numerically (e.g. [141–144]) and experimentally (e.g. [145–152]) with additional results considering a set of holes of different shape and possibly forming different patterns also available in the literature [153–157]. Focussing on the problem involving a single circular hole in a symmetric isotropic elastic plate, the complexity of a theoretical solution varies significantly depending on whether we consider a plate of infinite width [128, 135] (the Kirsch solution, after [135]) or a plate of finite width (strip) [136, 139] (the Howland solution, after [136]). The extent of additional work in moving from the former approach to the latter is critically assessed in [138]. Naturally, the ratio between the hole diameter and the plate width ($\frac{d}{w}$) affects the solution only in the latter approach, while providing the well-known constant

value of the stress-concentration factor of three [128, 135] for the plate of infinite width.

In an experimental setting, however, we are bound to work with specimens of finite dimensions and, to obtain a precise experimental validation of a theoretical prediction, the simpler (Kirsch's) result for an infinitely wide plate may be impractical, especially for narrow specimens with a relatively large $\frac{d}{w}$ ratio. This is shown by Toubal et al. [149], who performed experiments on a composite material (carbon/epoxy). During the experimentally performed non-contact measurement using the electronic speckle pattern interferometer (ESPI), the obtained stress-concentration factor was compared with the analytical solution for an infinite anisotropic plate with a hole [137] and the obtained results were significantly smaller than those predicted theoretically. The authors actually attributed this discrepancy to the precision of the measurement, but it is also clear that the analytical solution for an infinite plate used [137] may not have been too appropriate for their samples with a relatively high $\frac{d}{w}$ ratio of 0.3.

The first experimental investigations began in 1912 [145], immediately followed by [158, 159], after which Howland derived his analytical solution [136]. Wahl et al. [146] turned to the experimental validation of Howland's solution in their work where the extrapolation method to the photoelastic analysis of bakelite specimens with a circular hole subjected to uniaxial tension was applied. The obtained results of the stress concentration factor at the edge of the hole, which depend on the ratio of the hole diameter to the width of the plate d/w , were compared with both, the experimental results available until then [145, 158, 159], and Howland's analytical solution. Their results roughly correspond to Howland's analytical solution, while other known experimental results show much larger deviations. In his technical note for NACA (National Advisory Committee for Aeronautics, the ancestor of NASA) Griffith reported about conducting an experiment on five different aluminium strip specimens 2.31 mm thick with a circular hole in tension [148]. He investigated the strain and stress concentration around the hole in both elastic and plastic behaviour, where the strain gauges were used for strain measurements. In the case of elastic behaviour, the experimentally obtained stress concentration factor was on average only 0.7% higher than the theoretical (Howland's) assumption, while a larger deviation was observed along the transverse profile across the cross section cut through the middle of the hole. During plastic deformation, it was demonstrated that stress concentration at the hole's edge decreased, while the strain concentration increased significantly compared to the elastic behaviour. Durelli and Sciammarella [147] compared the results in the elastic part of their analysis with Griffith's

experimental results [148] and with Howland's analytical solution. For strain measurement of an aluminium strip with a circular hole, the Moiré method was used [160]. This technique involves comparing the grid pattern (i.e. changes in the grid's alignment) on the sample before and after applying load to assess deformations [161]. The experimentally determined values of the stress-concentration factor were several percent lower than Howland's, and in addition it was shown that the axial stress profile across the specimen through the hole visibly departs from the analytical solution in the region modestly away from the edge of the hole.

Aradhye and Kulkarni investigated the influence of the number and size of the holes on the stress concentration factor [154]. For this purpose, they conducted an experiment on isotropic (mild steel) and orthotropic specimens (composite material with carbon fibres) subjected to uniaxial tensile loading. For each type of specimen, a case with one, two or three holes was considered. The strains were monitored with strain gauges and from these results the maximum stresses, and consequently the stress concentration factors, were determined. Comparing the experimental results with the numerical model, it was found that the experimental results are always lower than the numerical ones, and that appropriate matching occurs only for orthotropic plates with two and three holes and partial agreement for isotropic plates with the same number of holes. The largest error occurs for both types of single-hole plates, which is to be expected considering that increasing the number of adjacent holes in a regular grid reduces the inhomogeneity of the plate. Interestingly, the largest error occurs in the case of an isotropic plate with one hole, where the experimental values of the stress concentration factor of all tested cases of chosen d/w ratios are on average 40% lower than the numerical results. However, it has been observed that there is a lack of explanation of the methodology used to compare the numerical and experimental results of the stress concentration values, especially considering that one strain gauge was used to measure the transverse strain across the transverse mid-section of the specimen, and another strain-gauge was used to measure the longitudinal strain along the longitudinal profile. It is worth noting that these strain gauges are not positioned directly at the edge of the hole, and that their measuring area is even larger than the hole itself.

If we, for a moment, step beyond the framework of the stress concentration analysis around a circular hole and consider, for example, a rectangular cut-out, the difference between theoretical predictions and experiments is also noticeable. This is demonstrated in [153], where an experiment is conducted on an isotropic (metal) plate with a rectangular hole, also in the context of linear-elastic behaviour. The authors point out the challenges in determining stress concentra-

tion factors based on strain-gauge measurements, with an exact quote: "Nevertheless, it is very hard (almost impossible) to "catch" stress concentration by means of classical measuring devices (strain gauges, inductive sensors) where a large gradient exists. . . " [153], and therefore they used an optical measuring system with 3D cameras for the displacement field measurements. They also concluded that the experimentally determined values of the stress concentration factor are about 6% lower than the numerical and analytical results [162].

The conducted experiments from the literature thus largely provide (i) slightly lower stress values at the edge of the hole and (ii) different stress profile up to a certain distance from the hole than those predicted theoretically. These discrepancies provide the main motivation for the present research, which is focussed on answering the following three important questions: (i) Can we confirm that the classical theory of elasticity cannot describe the considered problem well enough, (ii) can we provide a better theoretical prediction by assuming an alternative (non-classical) continuum theory, and (iii) what is the exact procedure for determining the unknown material parameters? Here, we are specifically looking for a possible solution to this problem in the framework of the so-called micropolar (Cosserat) continuum theory [15], with the aim of providing an evidence-based assessment of the suitability of this particular theory to provide the solution which passes experimental validation.

In the present context, due to the existence of additional micropolar parameters (in particular, the coupling number and the characteristic length for bending), we are testing whether it is possible to better capture the behaviour of the problem under consideration using this theory. Analytical micro-polar solutions for the present problem in fact exist [27, 35], but to the best of our knowledge only for the case of the infinitely wide plate. The discrepancy between experimental results and solutions based on the classical theory for the problems involving stress concentrations due to holes or cracks has already been noted in the literature [10, 11, 13]. This was especially highlighted by W. Nowacki: "*However, in many cases essential differences have been observed between theory and experiment; this fact refers first of all to the states of stress in which there occur large stress gradients. As an example of such a state let us mention the stress concentration in the vicinity of holes, or near notches and cracks.*" [10], and by another pioneer of the micropolar theory R. Lakes: "*The predictions of elasticity theory agree with experiment for most engineering materials under most circumstances. Discrepancies have been reported in the literature between theory and experiment in fatigue properties of coarse-grained materials in*

regions of large strain gradient." [13]. The micropolar theory has been mentioned as a *possible* better description of the phenomenon [163], but this hypothesis has not yet been tested, most likely due to the challenges in monitoring the experiment in the region of large strain gradients and due to the lack of reliable methods for determining micropolar material parameters. Hence, we propose **a complete methodology** involving parametric and inverse numerical analysis tuned to provide the numerical results for strains corresponding to those obtained from the strain-gauge measurements for specimens with different $\frac{d}{w}$ ratio.

6.2 Experimental testing

6.2.1 Specimen description

A set of experimental tests on specimens made of a widely used aluminium extrusion alloy EN-AW 6060 t66 has been performed in order to provide the analysis described. The geometrical characteristics of the rectangular specimens are $L = 300$ mm (length), $w = 60$ mm (width) and $t = 7$ mm (thickness), as shown in Figure 6.1a. In order to investigate the influence of the hole size, the experiment has been performed on three different types of the specimens having different dimensions of the circular hole drilled in the centre (Figure 6.1b). According to the hole diameter size $d = 10, 15$ and 20 mm, each specimen has been denoted as PH10- i , PH15- i and PH20- i , where PH stands for "plate with a hole" and $i = 1, 2, 3$ denotes the specimen number (three specimens for each specimen type).

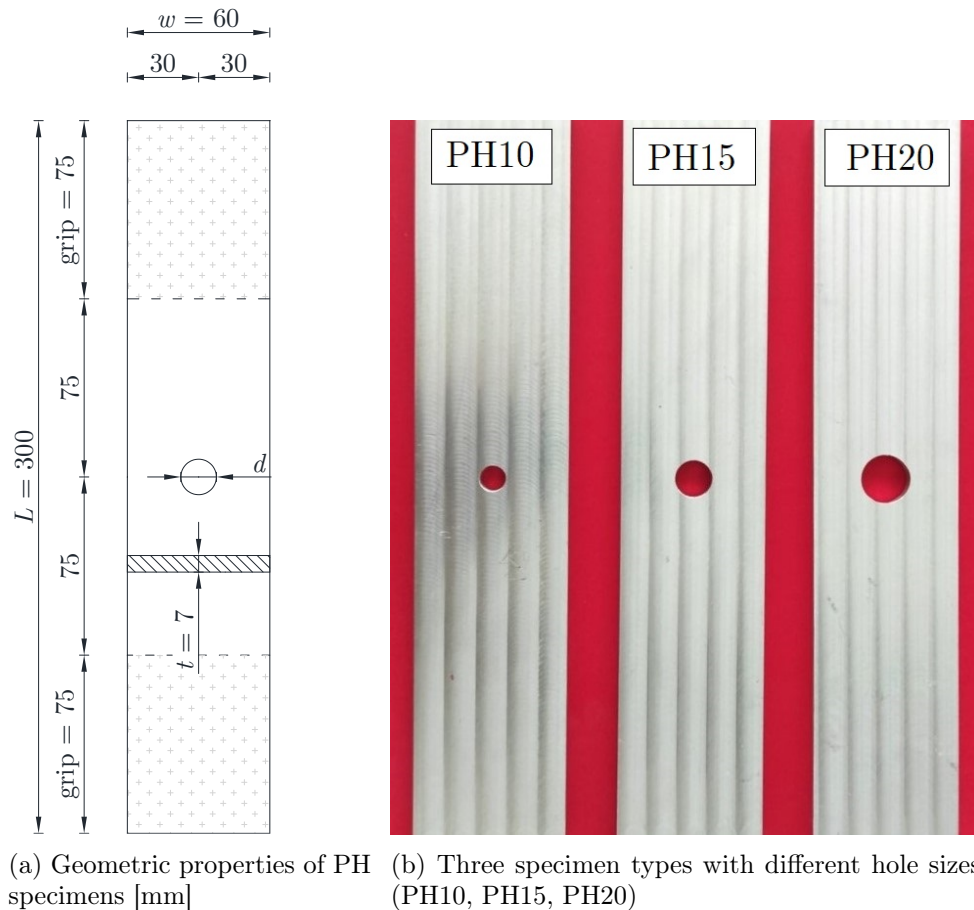


Figure 6.1: PH Specimens.

Three additional solid control samples of a dog-bone shape (labelled as TS7-1, TS7-2, TS7-3) have been tested to determine the mechanical properties of the specimen material. As in

the PH specimens, the rectangular cross-sectional shape and the thickness $t = 7$ mm of the control samples have been chosen. The control samples have been designed in accordance with European Standard for Tensile Testing of Metallic Materials at Room Temperature EN ISO 6892-1 [164], where the recommendations for the method and the design of specimens thicker than 3 mm are given in Annex D. In addition, their design took into account the technical constraints of the tensile machine, such as the minimum "grip to grip" distance and the required area of the specimen edge entering the machine jaws. Three samples have been prepared for each specimen type, which are shown in Figure 6.2. The experiments have been performed on a universal tension-compression testing machine Zwick/Roell Z600, in the Structures Laboratory of the Faculty of Civil Engineering, University of Rijeka [165]. The tensile testing machine is vertically divided by a movable cross head, and it consists of two working chambers: the upper chamber with hydraulic jaws, and the lower chamber with either pneumatic or hydraulic. All specimens have been tested using the testXpert II programme [166]. To determine the mechanical properties of the control specimens, a standard uniaxial tensile test according to EN ISO 6892-1, A1 method has been performed, where the strain rate 0.00025 1/s has been applied using extensometers until the yield point has been reached. After reaching the yield point, the strain rate increases up to 0.0067 1/s, where the displacements have been controlled by the movable cross head.



Figure 6.2: Test specimens (TS) for determination of material properties.

Figure 6.3 shows the stress-strain curves of the tested specimens and it also shows the corresponding Ramberg-Osgood's material law, which is often used to define a three-parameter model

relationship between stress and strain for such an aluminium material [167]. A slightly curved elastic part of the stress-strain curve is characteristic of this model, but in our tests the elastic behaviour exhibits complete linearity. For the purpose of this research, the elastic part of the stress-strain diagram will thus be considered as exactly linear.

The following average values of the test results thus have been obtained: tensile strength $f_u = 209.85$ MPa, offset yield strength $f_{y,0.2} = 175.34$ MPa, $f_y = 165.06$ MPa, Young's modulus $E = 67050.55$ MPa, and Poisson's ratio $\nu = 0.3$.

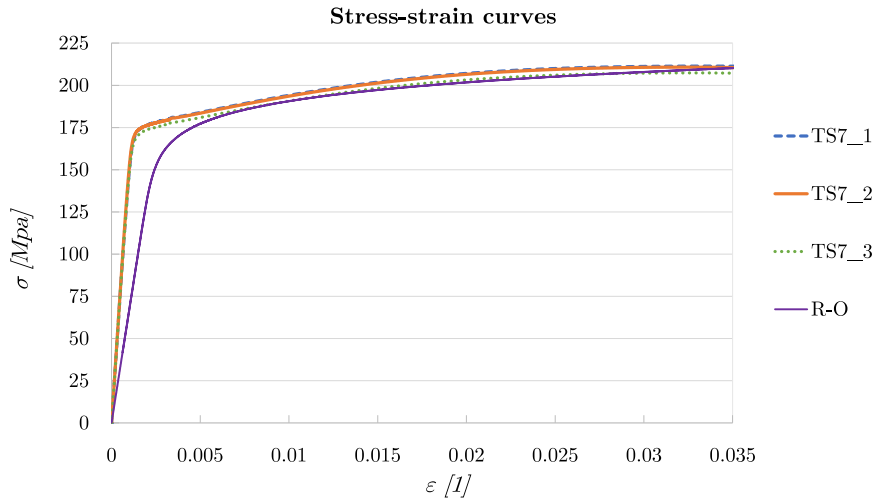


Figure 6.3: Stress-strain curves for tested TS7- i specimens and according to Ramberg-Osgood relationship.

6.2.2 Preparation for strain measurements

Two types of strain gauges have been attached to each specimen, inside and near the hole, to measure the longitudinal strains. For this, the electrical-resistance strain gauges with the smallest possible measurement areas have been chosen. The first type is HBM K-CLY9x-1.5/120 [168], a configurable, pre-wired linear strain gauge with 1.5×2.0 mm² measurement area and 120 Ω resistance, which is placed inside the hole (Figure 6.4a). The second strain-gauge type used is HBM 1-LY5x-3/120 [168], a narrow strain gauge with the wire lead at each end of the grid, which is placed on the outer surface of the specimen near the edge of the hole (Figure 6.4b). Its measuring surface is 3.0×0.4 mm² and its resistance 120 Ω . Before gluing the strain gauges, each specimen must be thoroughly cleaned of all dirt and grease. The strain gauges have been placed at the positions as shown in Figure 6.5. Depending on the position, each strain gauge is labelled with the following designations: LI (left inside), RI (right inside), LO (left outside) and RO (right outside).

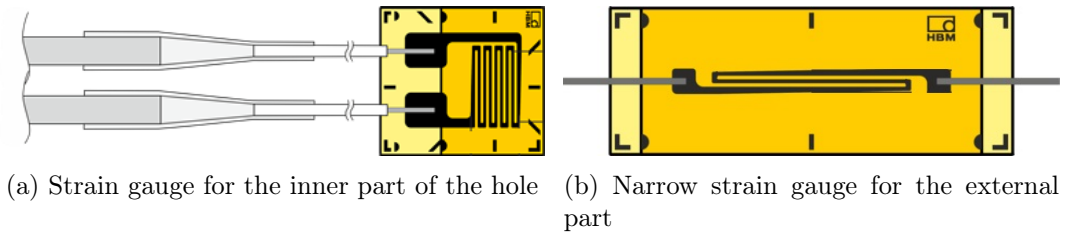


Figure 6.4: Used strain gauges from the manufacturer’s catalogue [168].

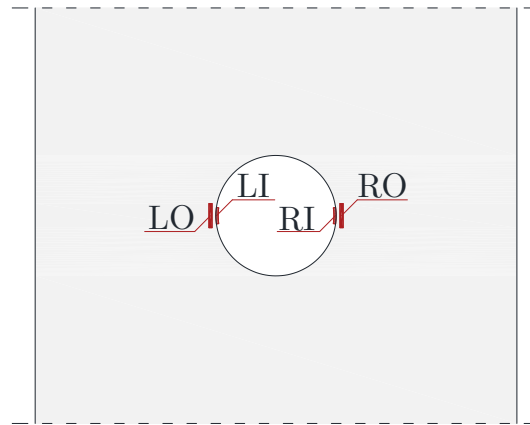


Figure 6.5: Strain-gauge positions (LI, RI - type K-CLY9x-1.5/120 placed inside the hole; LO, RO - type 1-LY5x-3/120 placed near the hole on the face of the specimen).

The internal strain gauges (LI, RI) are attached to the specimens with a fast-curing glue for experimental testing HBM X60 [168], which consists of two components (powder and liquid) that are mixed just before use. A pair of tweezers and an adhesive tape help with the gluing process. This type of strain gauge is pre-wired, and the wires have been simply connected to the adapters containing Wheatstone circuits in a quarter-bridge type I setting, from which the measured signal is passed to the acquisition unit connected to a PC terminal. The strain gauges LO, RO have been attached to the specimen using a cold-curing superglue for experimental testing HBM Z70 [168]. Furthermore, the strain gauges LO, RO have wire leads on each end and HBM LS7 external terminals [168] have been used to solder them to the wires connected to the adapters (Figure 6.6a). Some areas around the strain gauges are additionally protected with an insulating duct tape so that the leads do not touch the (metal) specimen (Figure 6.6b). The strain gauges have been calibrated immediately before the test starts. Then the strain gauge measurement data is recorded using NI Signal Express software [169] and analysed once the test has been completed.

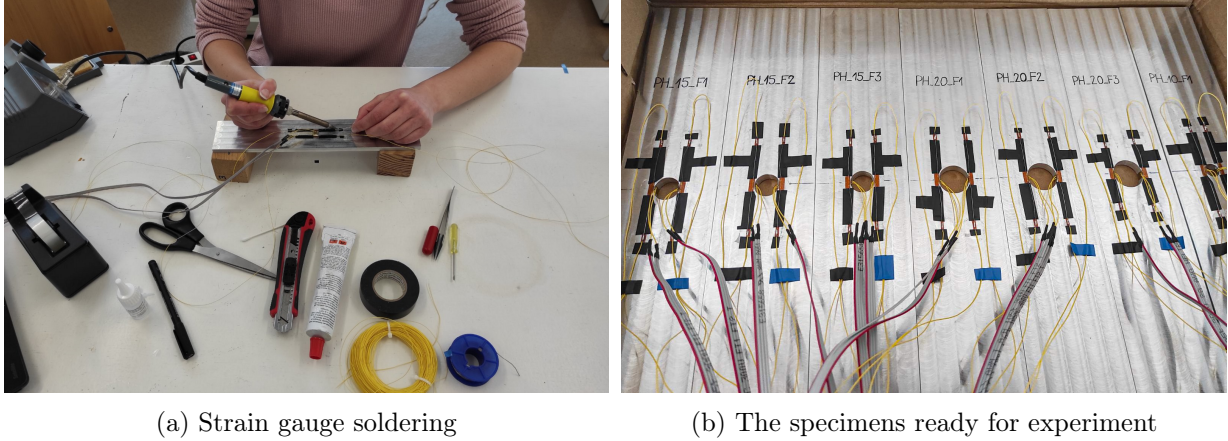


Figure 6.6: Preparation for strain measuring.

High strain gradients arose in the area around the hole during the tensile test. For this reason, the installation of the external strain gauges (LO, RO) has been performed as accurately as possible to ensure that they are equidistant from the edge of the hole. However, small deviations from the exact positions occurred during installation. The actual distances between the edge of the hole and the inner edge of the strain gauges have been measured using a high-accuracy digital caliper after installation, and are shown in Table 6.1.

Table 6.1: Measured distances between the inner edge of each external strain gauge and the edge of the hole [mm].

Sample	Strain gauge		Average distance for each specimen type
	LO	RO	
PH10-1	0.663	0.657	
PH10-2	0.615	0.550	0.662
PH10-3	0.680	0.650	
PH15-1	0.681	0.670	
PH15-2	0.675	0.620	0.661
PH15-3	0.645	0.677	
PH20-1	0.543	0.659	
PH20-2	0.627	0.610	0.605
PH20-3	0.650	0.540	

6.2.3 Experimental setup

All nine specimens prepared in this way have been subjected to uniaxial tension using Zwick/Roell Z600 tensile testing machine (Figure 6.7). The largest possible value of the force has been applied

in order to achieve the greatest precision of the measured data, while at the same remain in the zone of linear elasticity. A maximum force $F = 20$ kN has been chosen for all three types of specimens to ensure $F < \frac{f_y \cdot A_{net}}{K_{tn}}$, where A_{net} is net cross-sectional area for the specimen with the largest hole PH20, and K_{tn} is the stress concentration factor at the edge of the hole obtained from the analytical solution [136]. The experiments consist of three phases: 1st phase in which the jaws grip the sample (the pressure of the jaws on the ends of the sample is 9 MPa), and when the tensile force is zero, 2nd phase is preloading of the sample up to 500 N (for 30 seconds), and 3rd phase is a slow-rate uniaxial stretching of the sample. The tensile force has been applied under displacement control of a constant speed 0.2 mm/min to the maximum force F . Low strain rate (0.0033 1/s) experiments provided practically the same material properties of tested aluminium solid control samples TS7-*i* [170].

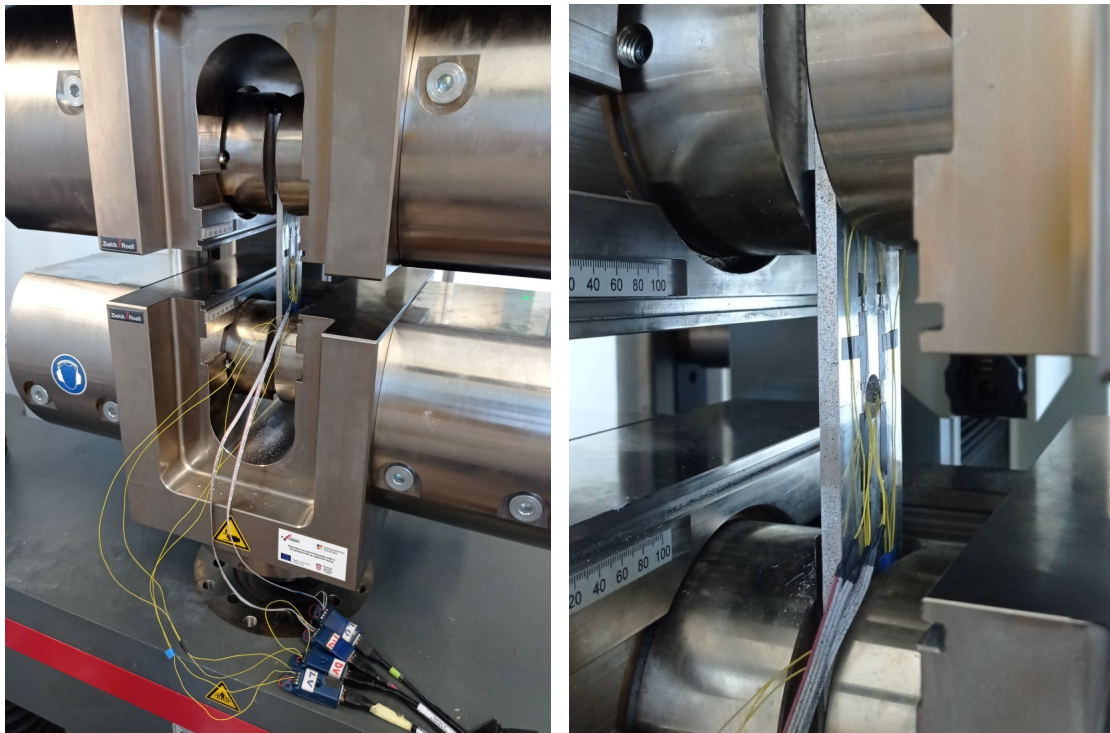


Figure 6.7: Experiment - a specimen subjected to uniaxial tension.

6.2.4 Data collection

The strains measured at the monitored positions in time are shown in Figures 6.8-6.10. The internal strain gauges show higher strains than the external ones, as expected. The specimen is preloaded with low forces during the first 30 seconds, hence the initial part of the measured strain curve is not properly linear. Due to the symmetry of the considered problem, the strains on the left and those on the right should coincide. However, the measurements do not entirely

confirm this expectation. The fundamental reason for this may be found in the actual distance of the outer strain gauges from the edge of the hole, or perhaps the correct placement of the inner strain gauges at the point of the hole nearest to the longitudinal edge of the specimen. That this is really so for the outer strain gauges (LO, RO) may be seen by comparing the distances of the individual strain gauges from Table 6.1 with the corresponding measured strain results in Figures 6.8-6.10, where it can be observed that the discrepancies between the strains measured by LO and RO are the largest in PH10-2, PH20-1 and PH20-3, where their respective distances from the edge of the hole are scattered the most. For this reason, only the results of the strain gauges whose distance in Table 6.1 do not deviate too much from the average value of 0.65 mm are considered for further comparison with the numerical results. More precisely, measurements provided by RO in PH10-2 , LO in PH20-1 and RO in PH20-3 are excluded from further analysis.

Table 6.2 shows the obtained strain results at the time t_{max} when the maximum force $F = 20$ kN is reached, where the results provided by the strain gauges mentioned above (RO in PH10-2, LO in PH20-1 and RO in PH20-3) have been printed as bold-face, and are not considered in the computation of the average strain. As expected, the hole size obviously affects the value of the longitudinal strain near the hole (and thus the value of the stress concentration factor), i.e., as the hole size increases, the values of the strain measured also increase.

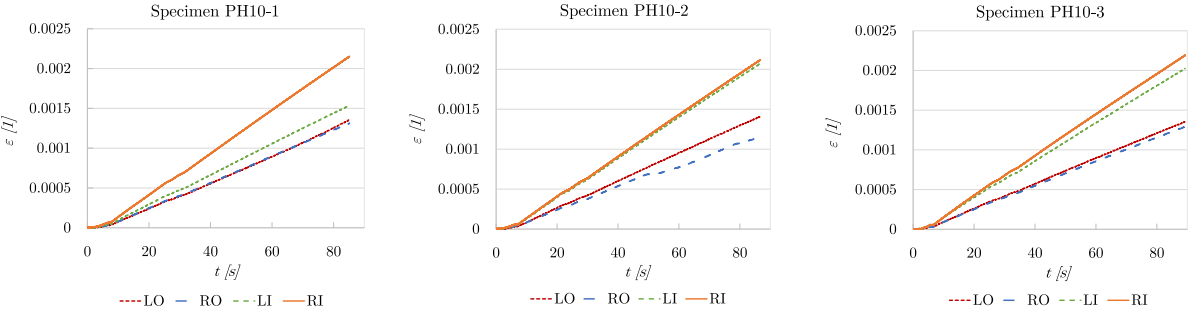


Figure 6.8: Strain measurements for the specimen PH10.

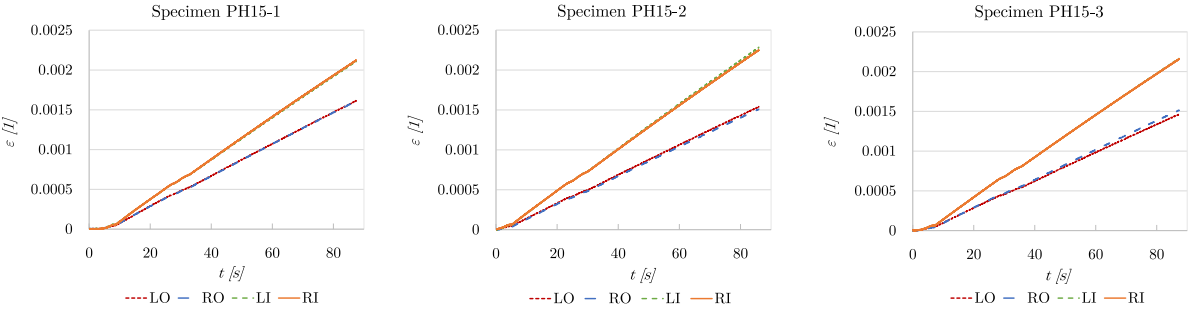


Figure 6.9: Strain measurements for the specimen PH15.

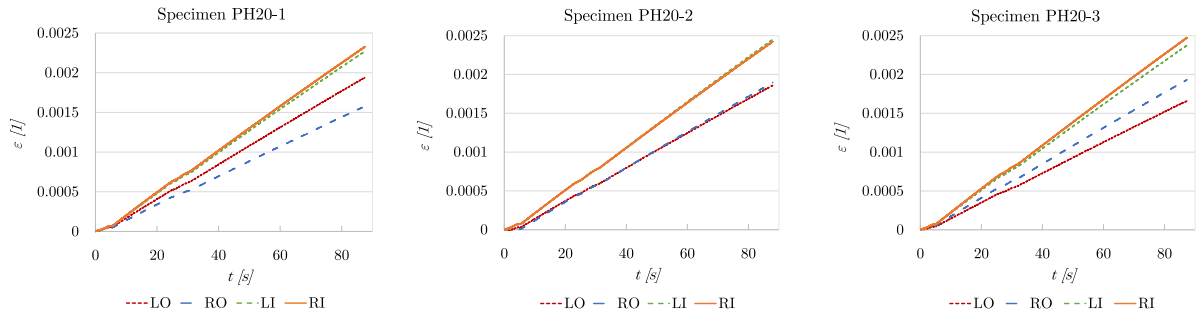


Figure 6.10: Strain measurements for the specimen PH20.

Table 6.2: Experimental measurements obtained by external and internal strain gauges for $F = 20$ kN.

Specimen	Position	ε_x	Average ε_x^*	Position	ε_x	Average ε_x^*
PH10-1	LO	0.00136	0.001347	LI	0.00155	0.00201731
	RO	0.00132		RI	0.00216	
PH10-2	LO	0.00141		LI	0.00207	
	RO	0.00114		RI	0.00211	
PH10-3	LO	0.00135	LI	0.00203		
	RO	0.00130	RI	0.00219		
PH15-1	LO	0.00161	0.001539	LI	0.00211	0.002179
	RO	0.00161		RI	0.00212	
PH15-2	LO	0.00154		LI	0.00228	
	RO	0.00151		RI	0.00225	
PH15-3	LO	0.00146	LI	0.00216		
	RO	0.00151	RI	0.00215		
PH20-1	LO	0.00194	0.001742	LI	0.00227	0.002384
	RO	0.00157		RI	0.00232	
PH20-2	LO	0.00186		LI	0.00245	
	RO	0.00188		RI	0.00242	
PH20-3	LO	0.00166	LI	0.00238		
	RO	0.00193	RI	0.00247		

6.2.5 Control experiment

To ensure the reliability of the obtained measurements, another control experiment on the same specimens under slightly modified conditions has been conducted. The tensile test has been performed in the lower chamber of the tensile testing machine, using pneumatic jaws up to a

maximum force of 10.5 kN (this is also the maximum allowable force for the used jaws), reached by the displacement control rate of 0.15 mm/min. By comparing the average strain-gauge results of each specimen type for both experiments, it has been demonstrated that deviation is less than 0.9%, as shown in Table 6.3.

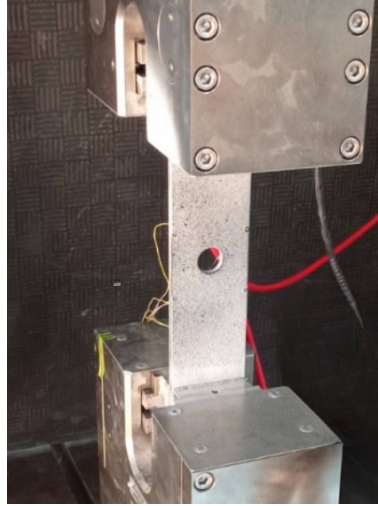


Figure 6.11: Control experiment - specimen subjected to uniaxial tension using pneumatic jaws.

Table 6.3: Experimental measurements from both conducted experiments for $F = 10.5$ kN.

	Average ε_x - external SG		Average ε_x - internal SG	
	Experiment	Control experiment	Experiment	Control experiment
PH10	0.00067	0.00067	0.00110	0.00110
PH15	0.00080	0.00079	0.00113	0.00112
PH20	0.00094	0.00095	0.00125	0.00124

Given that this control experiment has been carried out using jaws that did not obscure the view of the front or back surfaces of the specimens (cf. Figures 6.7 and 6.11), and that they were positioned in the accessible lower chamber of the tensile machine, the additional 2D optical measurements with 64 MP camera have been also performed. Before the experiment, the specimens were first sprayed with white anti-reflective spray, and then with the black spray to achieve a stochastic pattern. The experiment has been recorded at 4K resolution with an original frame rate of 30fps, which has been later reduced to 2fps, in order to reduce the amount of data and simplify processing. During the setup preparation, great care has been taken to ensure that the camera was aligned parallel to the specimen. Each video is post-processed using GOM Aramis Professional 2020 to calculate strain values through the measured displacements, at the exact locations where the external strain gauges were placed on the specimens to carry out a proper

comparison of the results. However, despite the use of various filters (spatial and temporal) to remove noise, it was not possible to obtain sufficiently accurate results. The obtained strains vary for about $\pm 0.025\%$ (which falls within the expected accuracy range of the DIC method [171]), that is too much for our very small linear elastic deformations (for both conducted experiments), which is in the range of $0.067\% - 0.094\%$. This makes the optical results inadequate for proper comparison.

6.3 Numerical investigation based on the classical theory of elasticity

A virtual experiment has been performed as an equivalent to the conducted real experiment. The geometrical and material parameters of the virtual specimens are based on PH specimen's data, where the thickness is $t = 7$ mm and the width is $w = 60$ mm, while the length is considered from grip to grip of the tensile machine so, for the numerical model it is equal to $L' = 150$ mm. Three types of numerical models corresponding to three specimen types with different hole diameters $d = 10, 15$ and 20 mm have been modelled. Given that there are two axes of symmetry, only one quarter of the whole sample model is considered, as shown in Figure 6.12. The elastic modulus $E = 67050.55$ MPa and the Poisson's ratio $\nu = 0.3$ are taken from the previous standardised tests. The finite-element mesh has been defined in the open-source software Gmsh 3.0.5. [132], where a dense mesh of planar quadrilateral finite elements with four nodes has been generated to discretise the model (the total number of finite elements is about 65000). Before the automatic discretisation, additional nodes have been inserted into the model as the boundary points of the external strain-gauge measurement area (1.5×0.4 mm²), located at the measured average distance between the inner edge of the strain gauge and the rim of the hole (Table 6.1), as shown in Figure 6.13 for the PH10 specimen type. After the numerical procedure, the results of the longitudinal strains in all Gauss points within the area of the so-called virtual strain gauge are read, averaged and compared with the experimental results. The circular arc of the hole is discretised using the finite elements whose sides are smaller than 0.15 mm, so we can say that the generated mesh faithfully approximates the geometry of the specimens. The mesh is generated in such a way that the mesh is denser in the area around the hole, and introduced into FEAP (Finite Element Analysis Programme) [127]. The uniformly distributed maximum load $q = \frac{F}{w \cdot t} = 47.62$ N/mm² is applied to the shorter edge of the model. Boundary conditions are defined along the

symmetry lines where the displacements constraints are imposed as shown in Figure 6.12. In the numerical analysis, the problem is considered as a plane-stress condition modelled using a very dense mesh as described composed of standard Lagrange Q4 finite elements. In addition, the results have been compared with a model where higher-order quadrilateral Q9 Lagrangian elements are applied, with the same number of finite elements as in the Q4 element model, both at the strain gauge locations and near the hole. Also, the 3D and 2D numerical models of the PH10 specimen type have been compared. Since there have been no differences in the results, it can be concluded that the simplified 2D model with a high mesh density of Q4 finite elements is sufficiently reliable and has been used for all the analysis in the following.

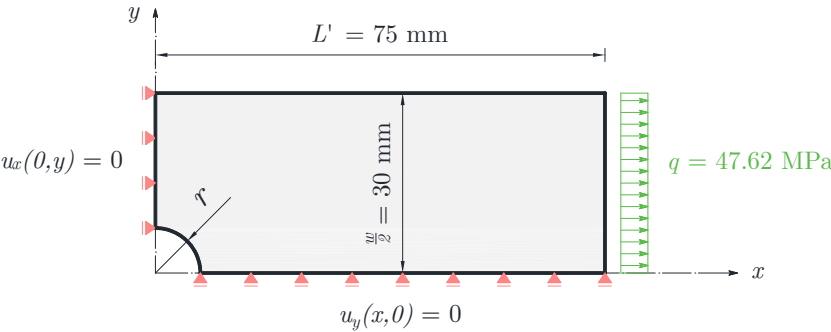


Figure 6.12: Quarter-plate model with a circular hole subjected to uniaxial tension.

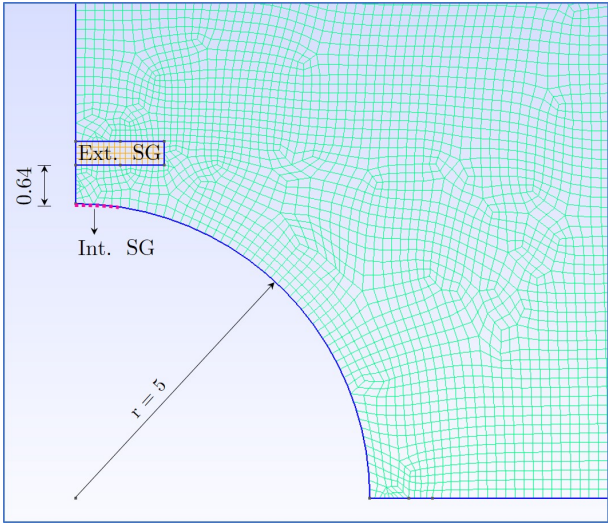


Figure 6.13: Finite element mesh around the hole of PH10 specimen [mm].

The value of the stress concentration factor K_{tn} has been defined as the ratio between the maximum longitudinal stress at the node placed at $(0, r)$ and $q \frac{w}{w-d}$ and compared to Howland's analytical solution [136] for each specimen type ($\frac{d}{w} = 0.667, 0.333, \text{ and } 0.25$) to assess accuracy of the numerical approach. Table 6.4 shows the comparison between the numerical and analytical

results, where it can be observed that the maximum difference between the two results is 0.12%. The numerical model is thus considered to be reliable and is taken for comparison with the experimental results without further recourse to the analytical solution. It is worth mentioning that the stress results in the node at $(0, r)$ are calculated by extrapolation from the corresponding stress at the integration points near the node.

Table 6.4: Comparison between Howland's analytical solution [136] and numerical results (using Q4 and Q9 finite elements) for the stress concentration factor at the edge of the hole.

Sample	$\frac{d}{w}$	K_{tn} [136]	K_{tn} num. Q4	Difference [%]	K_{tn} num. Q9	Difference [%]
PH10	0.167	2.584	2.581	0.11	2.583	0.03
PH15	0.250	2.432	2.429	0.12	2.435	0.11
PH20	0.333	2.314	2.314	0.03	2.311	0.10

Because of the large strain gradient in region near the circular hole, it is very important to carefully interpret the numerical results in order to compare them with the experimental results in a reliable manner. In other words, the strain values near the hole differ from point to point, and as we approach the edge of the hole, these values increase very sharply. For this reason, it is not correct to consider only the strains of the numerical model obtained in the position of the centre of a strain gauge, but account for the entire measurement area. In each strain gauge, there are several longitudinal wires whose electrical resistance changes depending on how much the cross-section decreases under the tensile load of the specimen. The measured strain value of each strain gauge strip represents the average value of the strain measured on the entire measurement area of the strain gauge's surface [168, 172]. For this reason, the average strain value obtained from all the Gauss points within the modelled surface of the "virtual strain gauge" is calculated for a realistic comparison with the experimental results. The same applies to the internal strain gauges, where the average strain values are obtained from all Gauss points closest to the edge of the hole, at the strain gauge measuring grid length of 0.75 mm. The surface and length on which the numerical results for the longitudinal strains at the external strain gauge (Ext. SG) and for the internal strain gauge (Int. SG) have been considered are shown in Figure 6.13 for the PH10 specimen type (the same applies to the remaining two specimen types). Tables 6.5 and 6.6 show the average numerical results obtained in this way and the obtained experimental strain results for all three specimen types from Table 6.2. The numerical model based on the classical theory of elasticity overestimates the influence of the circular hole in that it returns higher values of stresses and strains, which has been confirmed experimentally (see e.g. [147, 154]). Interestingly,

the difference between the numerical prediction and the experimental measurement increases with increase in the ratio $\frac{d}{w}$ for the external strain gauges, but it decreases for the internal strain gauges.

Table 6.5: Comparison between numerical and experimental results at the internal strain gauges.

Sample	Expt. results	Numerical results	Difference	Numerical results	Difference
	(average)	Q4 FE	[%]	Q9 FE	[%]
PH10	0.002017	0.002138	6.00	0.002152	6.65
PH15	0.002179	0.002269	4.12	0.002283	4.77
PH20	0.002384	0.002441	2.36	0.002457	3.03

Table 6.6: Comparison between numerical and experimental results at the external strain gauges.

Sample	Expt. results	Numerical results	Difference	Numerical results	Difference
	(average)	Q4 FE	[%]	Q9 FE	[%]
PH10	0.001347	0.001451	7.73	0.001450	7.68
PH15	0.001539	0.001712	11.23	0.001712	11.23
PH20	0.001742	0.001953	12.08	0.001955	12.19

Tables 6.5 and 6.6 show that even samples made of aluminium alloy (which is considered a homogeneous material) do not behave exactly as the classical (Cauchy's) theory predicts.

6.4 Numerical investigation based on the micropolar theory of elasticity

In practice, obviously, it is very important to be able to predict the real behaviour of structural elements, their parts and joints, and to this end a question as to whether there exists an alternative mechanical theory with better predictive capabilities occurs naturally. In an attempt to answer this question we will here consider the so-called micropolar or Cosserats' theory of elasticity [3].

We will investigate if it is possible to determine the extra material constants present in the theory capable of providing complete agreement between the numerical and experimental results.

6.4.1 Numerical model based on the micropolar theory of elasticity

Previously developed quadrilateral finite elements with four nodes and three degrees of freedom per node (two displacements u_x , u_y and one in-plane microrotation ϕ_z) *Q4EFP* have been used here to simulate a micropolar continuum in a plane stress condition. The displacement-type weak formulation is obtained by means of the principle of virtual work. The microrotation field is interpolated by the standard Lagrangian interpolation, while the displacement field is enhanced by applying the enhanced fixed-pole interpolation (see Chapter 4). The finite elements formulated in this way are introduced into FEAP, thus allowing numerical analysis based on the micropolar theory. With this numerical tool in hand, additional virtual experiments of a strip plate with a circular hole under tension have been carried out, but now using the micropolar theory of elasticity. The previously generated finite element mesh discretising each PH specimen type has been utilised. Along the specimen symmetry lines all the displacements orthogonal to them have been constrained (as shown in Figure 6.12), as have also the microrotations. The values of the Lamé constants are $\lambda = 38683.01$ N/mm² and $\mu = 25788.67$ N/mm² (which are computed from the known Young's modulus and the Poisson's ratio). The identification of the unknown micropolar parameters is a serious challenge, because a reliable procedure for their identification has not been established yet. A comprehensive parametric analysis will be performed next to determine the two unknown micropolar parameters (N and l_b), and then an inverse analysis will be used to find a suitable combination of these two parameters that gives a numerical result consistent with the experimental measurements.

In the utilised procedure, the values of the coupling number $N \in [0.1, 0.99]$ in the intervals

of 0.1 as well as the values for the characteristic length for bending $l_b \in [0, 10]$ in the intervals of 1.0 are considered, giving a total of 110 combinations. The results of the numerical analysis which are monitored are the strains determined at the locations of the "virtual strain gauges", as defined earlier in the numerical tests using the classical theory.

6.4.2 Results of parametric and inverse analyses

The numerical strain results for different values of the micropolar parameters N and l_b for all three specimen types are shown in Figures 6.14-6.16 at the locations of the internal strain gauges, while Figures 6.17-6.19 show the results at the locations of the external strain gauges. In these figures, the strains obtained using the numerical analysis based on the classical theory are represented by the top horizontal line, while the experimental results are represented by the bottom horizontal line. The strain results generally decrease by increasing the values of the micropolar material parameters, N and l_b . The intersection points in Figures 6.14-6.19 represent a family of combinations of parameters N and l_b that lead to the micropolar numerical results consistent with the experimental results for each specimen type at both sampling points (positions of the strain gauges).

The inverse analysis has been performed first for the case of the internal strain gauges, and then for the case of the external strain gauges. Clearly, the following two demands have to be met to confirm the hypothesis that the micropolar continuum theory is capable of predicting the measured results. First, for a chosen set of strain gauges (external or internal) a unique pair of values (N and l_b) provides the measured strains for all specimen types (PH10, PH15, PH20) and, second, the same (N and l_b) provides the correct prediction for the other set of strain gauges. Therefore, for all the six measurements, the experimental results have to be correctly predicted by *a unique pair* of micropolar material parameters (N and l_b).

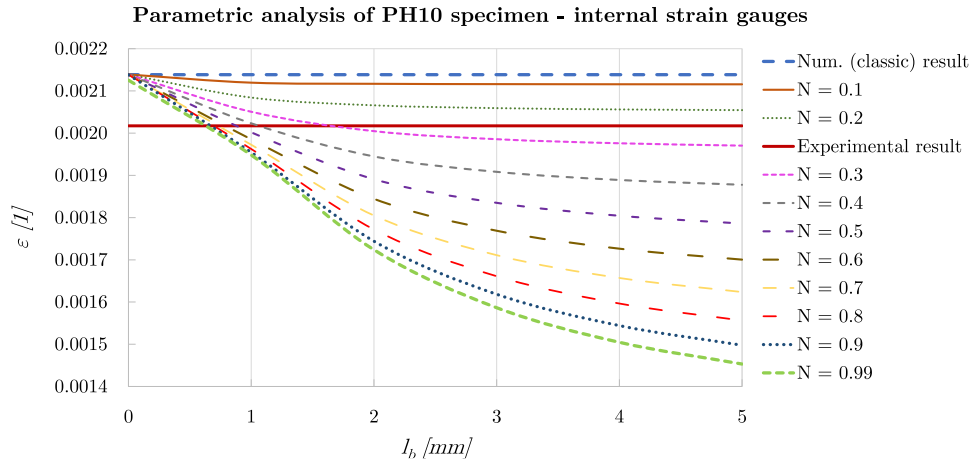


Figure 6.14: Parametric analysis of PH10 sample for internal strain gauges

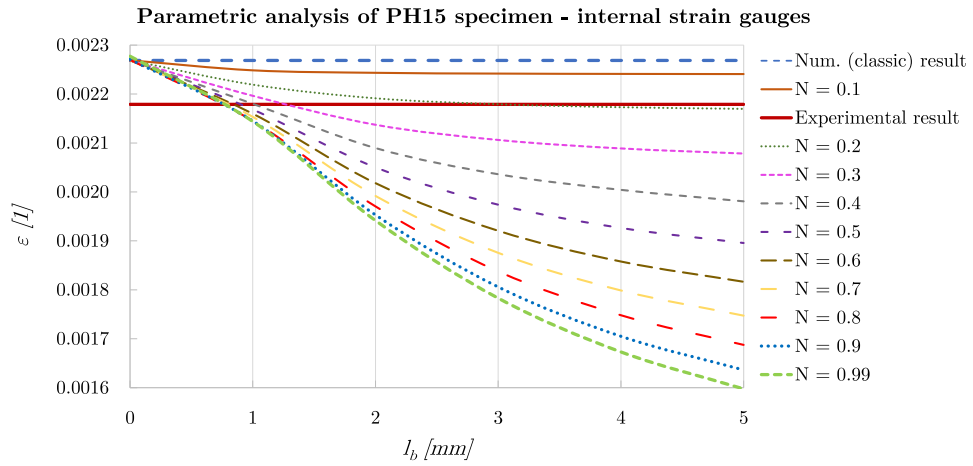


Figure 6.15: Parametric analysis of PH15 sample for internal strain gauges

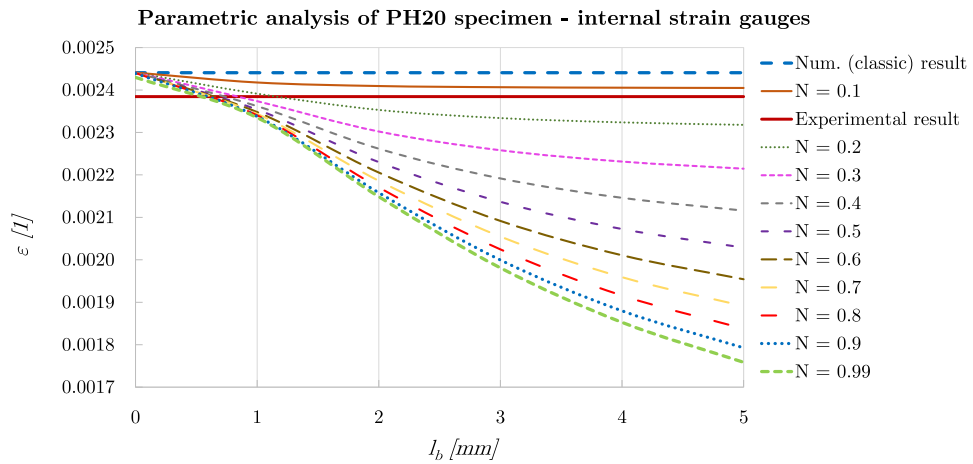


Figure 6.16: Parametric analysis of PH20 sample for internal strain gauges

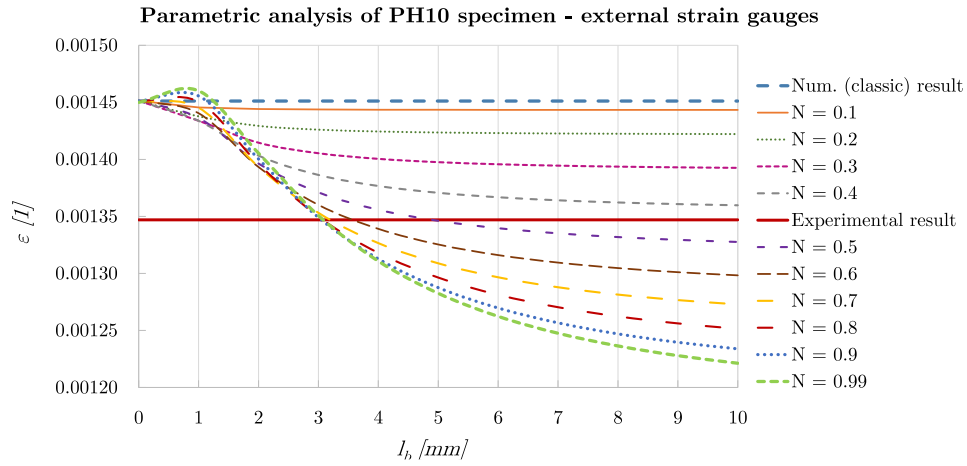


Figure 6.17: Parametric analysis of PH10 sample for external strain gauges

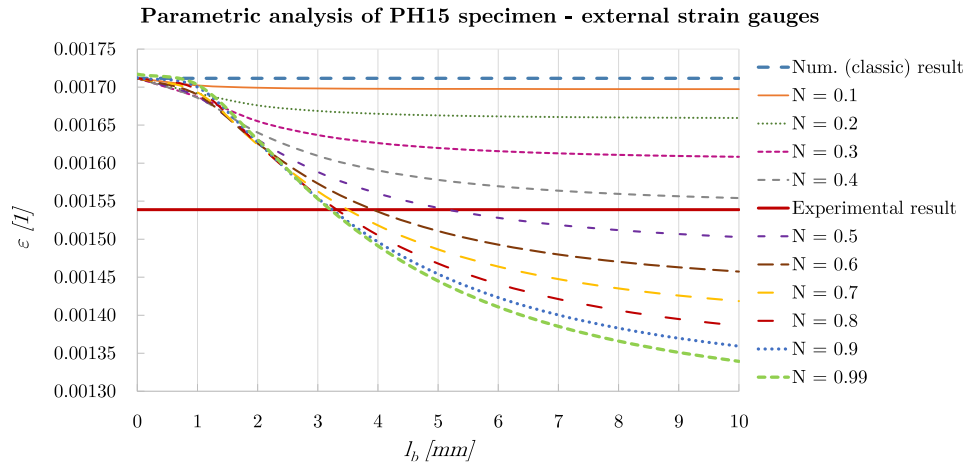


Figure 6.18: Parametric analysis of PH15 sample for external strain gauges

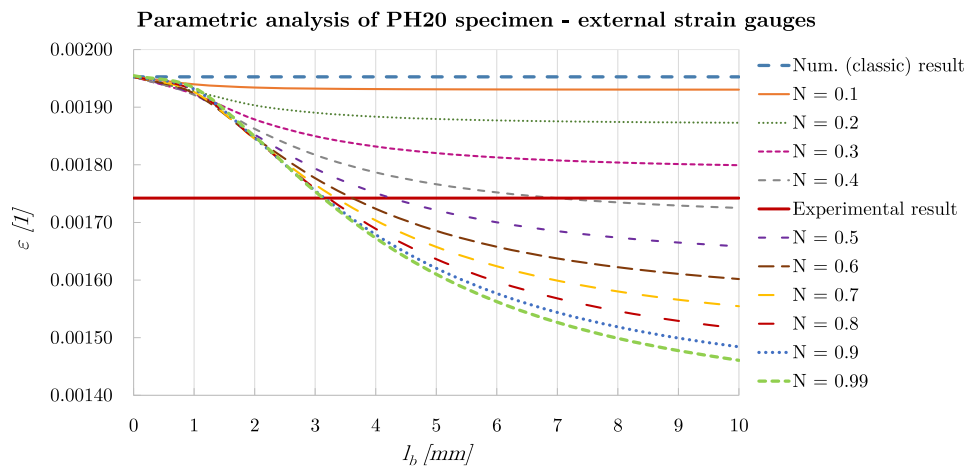


Figure 6.19: Parametric analysis of PH20 sample for external strain gauges

- **Internal strain gauges**

In order to find a parameter combination that properly describes the behaviour of all the specimen types and thus has the potential to be generalised not only for arbitrary $\frac{d}{w}$ ratio, but also for different tests involving the same material, an analysis of the possible combinations of N and l_b has been performed for each specimen type. Only those values of N for which a solution exists for each specimen type ($N = 0.3, \dots, 0.99$) have been retained for analysis. The analysis of combinations has been carried out in such a way that for each N -curve a value of the characteristic length has been sought which provides the numerical results corresponding to the experimental results for each particular specimen type (Table 6.7). For each observed N , an average value of the characteristic length for bending has been calculated from the results for each specimen type. Of course, there are more possible combinations when we consider denser intervals for the N and l_b parameters. Generally, it can be seen that for smaller values of the coupling number N , a suitable value for l_b is higher, and vice versa. More importantly, larger variation of the characteristic bending lengths across the specimen types is observed for smaller values of the coupling number, indicating that a unique characteristic bending length is more likely to be found at the maximum theoretically possible value of the couple number ($N \rightarrow 1$).

Table 6.7: Combinations of parameters N and l_b for each specimen type providing the numerical results for the longitudinal strains equal to the experimental results obtained by the internal strain gauges.

N	Specimen type	l_b	Specimen type	l_b	Specimen type	l_b	Average l_b	Standard deviation
0.3		1.64		1.26		0.84	1.25	0.40
0.4		1.06		1.02		0.74	0.94	0.17
0.5		0.88		0.90		0.68	0.82	0.12
0.6	PH10	0.78	PH15	0.84	PH20	0.64	0.75	0.10
0.7		0.73		0.81		0.62	0.72	0.09
0.8		0.69		0.76		0.61	0.69	0.08
0.9		0.67		0.76		0.60	0.68	0.08
0.99		0.63		0.73		0.59	0.65	0.07

Indeed, for the highest analysed value of the coupling number ($N = 0.99$), the characteristic bending lengths vary the least, leading to the conclusion that their average ($l_b = 0.65$) along with $N = 0.99$ provides the best theoretical prediction. This in turn indicates that here the

microrotation coincides with macrorotation, which is a characteristic of the couple-stress theory [173,174].

- External strain gauges

In an analogous manner, the analysis for the six possible values of the coupling number ($N = 0.5, 0.6, 0.7, 0.8, 0.9, 0.99$) for the external strain gauges has been performed for each specimen type (see Figures 6.17-6.19).

Table 6.8: Combinations of parameters N and l_b for each specimen type providing the numerical results for the longitudinal strains equal to the experimental results obtained by the external strain gauges.

N	Specimen type	l_b	Specimen type	l_b	Specimen type	l_b	Average l_b	Standard deviation
0.5		4.90		5.15		4.26	4.77	0.46
0.6		3.57		3.92		3.62	3.70	0.19
0.7	PH10	3.19	PH15	3.50	PH20	3.35	3.35	0.16
0.8		3.07		3.31		3.22	3.20	0.12
0.9		3.05		3.24		3.15	3.15	0.10
0.99		3.08		3.21		3.13	3.14	0.07

The smallest difference between the experimental and the numerical results for all three specimen types are obtained for the combination with $N = 0.99$ and $l_b = 3.14$. This effectively means that at these positions the material does not exhibit a behaviour featuring an independent microrotation field which is on its own a characteristic of the couple-stress theory [20,174]. As before, the characteristic bending length varies the least for the highest values of the coupling number ($N = 0.99$) providing the average $l_b = 3.14$. This pair of micropolar material parameters therefore provides the best theoretical prediction of the strains at the positions of the external strain gauges.

As can be seen from Tables 6.7, 6.8, a unique combination of the micropolar parameters N and l_b capable of capturing both cases of the strain gauge position *does not exist*. Moreover, the possible parameter combinations in the case of the external strain gauges involve the values of the characteristic length for bending that are several times larger than in the case of the internal strain gauges. Clearly, the micropolar theory therefore cannot model the actual behaviour of the studied problem, nor the couple-stress theory can, as its special case ($N \rightarrow 1$). The unique coupling number of $N = 0.99$ in both sets of experiments, however, clearly indicates that *no*

independent micropolar field develops in the process. Figure 6.20 illustrates the above conclusion about the inability of the couple-stress theory to model the present problem, for the specimen type PH10 (similar graphs may be plotted for the specimen types PH15 and PH20, too). This specimen type is singled out because its ratio $\frac{d}{w} = 0.166$ makes its results comparable with the analysis conducted in [147] ($\frac{d}{w} = 0.156$), where the strain field was measured using the Moiré method, which provided a complete strain distribution in the specimen. Comparing the present strain-gauge measurements with those from [147] for the load of 44.82 N/mm^2 applied here, we are able to validate the present measurements. Furthermore, we may reasonably conclude that the whole longitudinal strain profile across the cross-section cutting through the centre of the hole in [147] is a reliable experimental result, which is plotted in Figure 6.20 and compared with our numerical simulations. Precisely, none of the two parameter choices ($l_b = 0.65$, $l_b = 3.14$), along with $N = 0.99$ can make the numerical results reproduce the experimental curve obtained in [147].

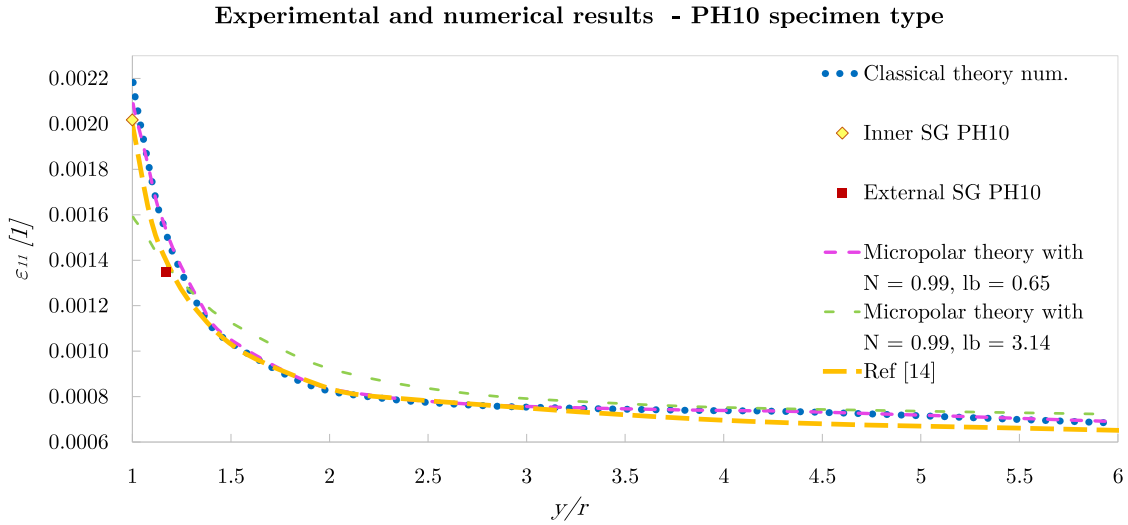


Figure 6.20: Comparison between the experimental and numerical results based on the two theories for PH10 specimen type (r - distance from the hole rim to the specimen edge).

6.5 Conclusion

In an attempt to test if the micropolar theory of elasticity may better describe the stress and strain distribution around the circular hole in an axially loaded strip than the classical theory, laboratory experiments have been carried out on three types of aluminium strip specimens and the corresponding numerical simulations provided. By comparing the experimental longitudinal strains at characteristic positions near the hole obtained by strain gauge measurements with the

corresponding results obtained by a virtual experiment in the framework of numerical analysis based on the classical theory of elasticity, discrepancies of up to 12.08% have been observed. We have stipulated that one of the alternative theories of elasticity, the so-called micropolar theory, would be able to provide a potential solution to this problem through its capacity to accommodate the experimental results via additional material parameters - the coupling number and the characteristic length for bending. To this end, numerical analysis of the problem is performed within the finite element method based on the micropolar theory to find a family of possible solutions. Parametric and inverse numerical analyses have been applied to determine the combination of the two micropolar constants that would provide numerical strain results that agree with the experimental measurements. For both sets of strain-gauge measurements, it has been concluded that the smallest scatter of the characteristic bending lengths across the specimen types takes place for the maximum possible value of the coupling number ($N \rightarrow 1$), which clearly indicates that no independent micropolar field develops in the process. In addition, considerable difference in the values of the characteristic bending length is obtained based on the two sets of measurements. We thus conclude that the micropolar continuum theory is not capable of predicting the actual behaviour and that the answer should be sought in some other alternative continuum theory, possibly of the strain-graded type.

To further validate the presented experimental results in future work, a strain gauge strip composed of several equidistant strain gauges in a chain specifically designed to determine the strain gradient along the analysed line [168] may be used, as well as non-contact measurement in situations when a larger load may be applied while remaining within the confines of linear-elastic behaviour (which has been a limitation in this research).

Chapter 7

Conclusions and future work

7.1 Development of new micropolar finite elements

From the extensive investigation of the relationship between the Lagrangian, the helicoidal and the fixed-pole interpolation in their linear form, and the well-known linked interpolation, the new enhanced fixed-pole interpolation has emerged as a possible interpretation of the linked interpolation. By introducing an additional coefficient into the enriched part of the interpolated displacement field, the same formulation is obtained as in the application of the linked interpolation for the standard degrees of freedom, which is known to provide an exact solution for the 3D Timoshenko beam of arbitrary order with a sufficient number of nodes.

The presented interpolation has been then used for the development of the new family of finite elements of arbitrary order based on the micropolar continuum theory. The new quadrilateral and hexahedral finite elements have been validated through a set of patch tests, where the elements showed the ability to reproduce the constant stress state. The convergence rate has been additionally evaluated on several numerical examples in the static and vibrational analysis of the 2D and 3D micropolar continuum, where the proposed interpolation almost always proves to be the best approximate solution. Given that the research on the dynamic analysis of the micropolar continuum is quite limited so far, this excursion into the numerical analysis of natural frequencies of 2D and 3D micropolar problems with the application of Lagrange interpolation and two variants of fixed-pole interpolation represents a good basis for the future work that includes a complete dynamic analysis of a micropolar continuum.

It is concluded that the newly developed finite elements exhibit convergence and efficiency based on the showed results and therefore, they can be employed as a simulation tool for the

inverse determination of unknown micropolar material parameters in the second part of this research.

7.2 Identification of micropolar material parameters

The described procedure, based on a virtual experiment, has been performed to determine the value of the coupling number for the perforated aluminium specimens, for which the value of another important micropolar material parameter - the characteristic length for bending - was determined in an earlier research. The methodology is based on the virtual experiment of a planar classical model simulating the considered specimens under four-point bending, where the shear influence on the determination of the coupling number value is considered through three different experimental setups. The specimen model is then treated as a homogenised micropolar continuum discretised by the newly developed 2D micropolar finite elements. The coupling number is obtained through inverse analysis by fitting the results of the average displacements along the height of the model of several characteristic profiles based on the results obtained from the virtual experiment (classical model). Although the proposed methodology is not innovative, that is, it is inspired by the methodology from the literature, it does draw attention to certain components in the determination of the coupling number, aimed at its improvement. On the other hand, this study provides us to better understand this micropolar material parameter. It has been demonstrated that the coupling number is a highly sensitive constant and that it does not have a significant influence in the context of the considered 4PB problem, particularly in the 1st setup where the biggest bending moment is present. On the other hand, its influence becomes more pronounced as the ratio of shear to bending increases, leading to a smaller dispersion of the obtained values of N for all 4 types of specimens. For this reason, it is suggested that future research could benefit from exploring the region beyond pure bending or, even more effectively, conducting a virtual experiment involving pure shear to obtain a more accurate determination.

We have also performed tensile laboratory tests on a set of aluminium strips with three different ratios between the hole diameter and the strip width, in order to investigate the frequently reported discrepancies between experimentally obtained results and theoretical values for the stress concentration factor in this classical problem. Considering that the differences are notable in the literature even for homogeneous specimens in linear analysis (which additionally increases under cyclic loading), we limited our study to the simplest possible case of this problem to clearly

investigate the gap between theoretical and experimental values. The numerical results have been carefully compared with the strain gauge measurements, and, the results indeed show a certain deviation. The application of micropolar theory is investigated as an alternative, better description of this problem, which has not been studied before. A methodology based on parametric and inverse numerical analysis is hence suggested for the identification of the micropolar parameters present in the problem (coupling number and characteristic length for bending). However, it is concluded that there exists no specific set of constant values for these parameters that may make the simulation fit with the experiment for all the specimens tested. On the basis of the analysis conducted, we indeed affirm that the micropolar theory cannot predict the experimental results, in particular that it is not suitable for materials with a very low-scale internal structure.

In future work, conducting a 3D analysis of all three types of PH specimens and comparing the numerical solutions with the experimental results would be desirable. Alternatively, it will be good to perform an additional combined comparison with the numerical results of the 2D analysis based on the plane strain condition (only the plane stress condition has been analysed in Chapter 6), since the thickness of the specimens is not so insignificant compared to the width of the hole. This way, it would be completely verified whether the local theory adequately describes this problem. If this is still not satisfactory, future work could investigate whether another theory of the continuum is more adequate - such as the couple stress theory. Additionally, the problem of stress concentration around the circular hole in a plate made of micropolar material could be analysed in future work, specifically, a microstructure of a regular pattern could be artificially designed in the aluminium matrix of the tested specimens, and the inverse and parametric analysis presented in this paper could be performed to identify the micropolar material parameters for the designed microstructure.

As part of the research proposal "*Experimental research and numerical analysis of materials with a pronounced (micro)structure*" for which the BST grant has been awarded, laboratory experiments are also planned on cylindrical 3D-printed specimens of several different dimensions that will be subjected to pure torsion. The *size-effect* will be analysed and attempts will also be made to determine additional micropolar material parameters that manifest themselves in a state of pure torsion.

“Education is not something you can finish.”

Isaac Asimov

Bibliography

- [1] M.I F. Ashby, D. R. H. Jones, Engineering materials 1, 4th Edition, Elsevier, Oxford.
- [2] A. J. M. Spencer, Continuum Mechanics, Dover Publications, New York, 1980.
- [3] A. C. Eringen, Microcontinuum Field Theories: I. Foundations and Solids, Springer Verlag, New York, 2012.
- [4] A. Beveridge, Novel computational methods to predict the deformation of macroscopic heterogeneous materials, Ph.D. thesis, University of Strathclyde, Department of Mechanical Engineering Novel (2011).
- [5] D. Lazarević, J. Dvornik, N. Bićanić, O načelima i postupcima proračuna građevinskih konstrukcija, Faculty of Civil Engineering, University of Zagreb, Zagreb, 2019.
- [6] M. H. Sadd, Elasticity Theory, Applications, and Numerics, 3rd Edition, Elsevier, Oxford, 2014.
- [7] H. Altenbach, Fundamentals of continuum mechanics - Classical approaches and new trends, Journal of Physics: Conference Series 991 (1) (2018). doi:10.1088/1742-6596/991/1/012003.
- [8] S. Timoshenko, J. N. Goodier, Theory of elasticity, 2nd Edition, McGraw-Hill Book Company, Inc., New York, 1951.
- [9] L. Malvern, Introduction to the Mechanics of a Continuous Medium, Prentice-Hall, Inc, New Jersey, 1969.
- [10] W. K. Nowacki, Theory of Asymmetric Elasticity, Pergamon Press, Warszawa, 1985.
- [11] R. S. Lakes, Size effects and micromechanics of a porous solid, Journal of Materials Science 18 (9) (1983) 2572–2580. doi:10.1007/BF00547573.

- [12] M. Puškarić, Metalne pjene, Undergraduate thesis, Karlovac University of Applied Sciences.
- [13] W. B. Anderson, R. S. Lakes, Size effects due to Cosserat elasticity and surface damage in closed-cell polymethacrylimide foam, *Journal of Materials Science* 29 (24) (1994) 6413–6419. doi:10.1007/BF00353997.
- [14] M. Shaat, E. Ghavanloo, S. A. Fazelzadeh, Review on nonlocal continuum mechanics: Physics, material applicability, and mathematics, *Mechanics of Materials* (August) 103587. doi:10.1016/j.mechmat.2020.103587.
- [15] E. Cosserat, F. Cosserat, *Théorie des corps déformables*, Herman, Paris, 1909.
- [16] W. Voigt, Theoretische studien über die elasticitätsverhältnisse der krystalle, *Abh. Wiss. Ges.* 34 (1887) 3–51.
- [17] H. Schäfer, Das Cosserat kontinuum (eng. version), *ZAMM - Journal of Applied Mathematics and Mechanics* 47 (8) (1967) 485–498. doi:10.1002/zamm.19670470802.
- [18] H. Grad, Statistical Mechanics, Thermodynamics and Fluid Dynamics of Systems with an Arbitrary Number of Integrals, *Comm. Pure Appl. Math* 5 (1952) 455–494.
- [19] W. Günther, Zur Statik und Kinematik des Cosseratschen Kontinuums, *Abhandlungen der Braunschweigischen Wissenschaftlichen Gesellschaft* 10 (1958) 195–213.
- [20] R. Mindlin, H. Tiersten, Effects of couple-stresses in linear elasticity, *Arch. Rational Mech. Anal.* 11 (1962) 415–448. doi:0.1007/BF00253946.
- [21] R. A. Toupin, Theories of elasticity with couple-stress, *Archive for Rational Mechanics and Analysis* 17 (2) (1964) 85–112. doi:10.1007/BF00253050.
- [22] M. B. Rubin, *Cosserat Theories: Shells, Rods and Points*, Springer-Science+Business Media, Waterloo, Canada, 2000.
- [23] V. Eremeyev, L. Lebedev, H. Altenbach, Springer-Verlag, Berlin. doi:10.1007/978-3-642-28353-6.
- [24] M. H. Baluch, J. E. Goldberg, S. L. Koh, Finite element approach to bending of micropolar plates, *Journal of the Structural Division (ASCE)* 98 (9) (1972) 1957–1964. doi:10.1061/JSDEAG.0003326.

- [25] J. E. Goldberg, M. H. Baluch, T. Korman, S. L. Koh, Finite element approach to bending of micropolar plates, *International Journal for Numerical Methods in Engineering* 8 (2) (1974) 311–321. doi:10.1002/nme.1620080210.
- [26] S. Nakamura, R. Benedict, R. Lakes, Finite element method for orthotropic micropolar elasticity, *International Journal of Engineering Science* 22 (3) (1984) 319–330. doi:10.1016/0020-7225(84)90013-2.
- [27] P. N. Kaloni, T. Ariman, Stress concentration effects in micropolar elasticity, *Zeitschrift für angewandte Mathematik und Physik ZAMP* 18 (1) (1967) 136–141. doi:10.1007/BF01593904.
- [28] S. Ghosh, Y. Liu, Voronoi cell finite element model based on micropolar theory of thermoelasticity for heterogeneous materials, *International Journal for Numerical Methods in Engineering* 38 (8) (1995) 1361–1398. doi:10.1002/nme.1620380808.
- [29] F. Y. Huang, Two and three-dimensional isoparametric finite elements for axisymmetric micropolar elasticity, Ph.D. thesis, New Jersey Institute of Technology (1986).
- [30] W. D. Pilkey, D. F. Pilkey, *Peterson's Stress Concentration Factors*, 3rd Edition, John Wiley & Sons, Ltd, 2011.
- [31] F. Y. Huang, B. H. Yan, J. L. Yan, D. Yang, Bending analysis of micropolar elastic beam using a 3-D finite element method, *International Journal of Engineering Science* 38 (2000) 275–286. doi:10.1016/S0020-7225(99)00041-5.
- [32] S. Nakamura, R. Lakes, Finite element analysis of Saint-Venant end effects in micropolar elastic solids, *Engineering Computations* 12 (6) (1995) 571–587. doi:10.1108/02644409510799785.
- [33] D. Yang, F. Huang, Analysis of Poisson's ratio for a micropolar elastic rectangular plate using the finite element method, *Engineering Computations* 18 (7) (2001) 1012–1030. doi:10.1108/EUM0000000006213.
- [34] E. Providas, M. A. Kattis, Finite element method in plane Cosserat elasticity, *Computers and Structures* 80 (27-30) (2002) 2059–2069. doi:10.1016/S0045-7949(02)00262-6.
- [35] H. Neuber, On the general solution of linear-elastic problems in isotropic and anisotropic Cosserat continua, in: *Applied Mechanics: Proceedings of the Eleventh International*

Congress of Applied Mechanics Munich, Springer Berlin Heidelberg, Berlin, Heidelberg, 1966, pp. 153–158. doi:10.1007/978-3-662-29364-5{_}16.

- [36] L. Li, S. Xie, Finite element method for linear micropolar elasticity and numerical study of some scale effects phenomena in MEMS, *International Journal of Mechanical Sciences*, 46 (2004) 1571–1587.
- [37] V. V. Korepanov, I. N. Matveenko, V. P. andShardakov, Finite element analysis of two- and three-dimensional static problems in the asymmetric theory of elasticity as a basis for the design of experiments, *Acta Mechanica* 223 (2012) 1739–1750.
- [38] M. A. Wheel, A control volume-based finite element method for plane micropolar elasticity, *International Journal for Numerical Methods in Engineering* 75 (8) (2008) 992–1006. doi:10.1002/nme.2293.
- [39] A. Beveridge, M. Wheel, D. Nash, A higher order control volume based finite element method to predict the deformation of heterogeneous materials, *Computers & Structures* 129 (2013) 54–62. doi:10.1016/j.compstruc.2013.08.006.
- [40] S. Grbčić, A. Ibrahimbegović, G. Jelenić, Variational formulation of micropolar elasticity using 3D hexahedral finite-element interpolation with incompatible modes, *Computers and Structures* 205 (2018) 1–14. doi:10.1016/j.compstruc.2018.04.005.
- [41] S. Grbčić, G. Jelenić, D. Ribarić, Quadrilateral 2D linked-interpolation finite elements for micropolar continuum, *Acta Mechanica Sinica* 35 (2019) 1001–1020. doi:10.1007/s10409-019-00870-1.
- [42] S. Grbčić, Linked interpolation and strain invariance in finite-element modelling of micropolar continuum, PhD dissertation, University of Rijeka and Université de Technologie de Compiègne – Sorbonne Universités, Rijeka (2018).
- [43] Q. Xie, Y. Hu, Y. Zhou, W. Han, Improving the bending response of four-node quadrilateral and eight-node hexahedral elements for Cosserat elasticity problems, *Engineering Computations* 36 (6) (2019) 1950–1976. doi:10.1108/EC-08-2018-0380.
URL <https://www.emerald.com/insight/content/doi/10.1108/EC-08-2018-0380/full/html>

- [44] J. Padovan, Applications of 3-D finite element procedures to static and dynamic problems in micropolar elasticity, *Computers and Structures* 8 (2) (1978) 231–236. doi:10.1016/0045-7949(78)90027-5.
- [45] M. Godio, I. Stefanou, K. Sab, J. Sulem, Dynamic finite element formulation for Cosserat elastic plates, *International Journal for Numerical Methods in Engineering* 101 (13) (2015) 992–1018. doi:10.1002/nme.4833.
- [46] R. Ansari, A. Norouzzadeh, A. H. Shakouri, M. Bazdid-Vahdati, H. Rouhi, Finite element analysis of vibrating micro-beams and -plates using a three-dimensional micropolar element, *Thin-Walled Structures* 124 (November 2017) (2018) 489–500. doi:10.1016/j.tws.2017.12.036.
- [47] M. Kohansal-Vajargah, R. Ansari, M. Faraji-Oskouie, M. Bazdid-Vahdati, Vibration analysis of two-dimensional structures using micropolar elements, *Applied Mathematics and Mechanics (English Edition)* 42 (7) (2021) 999–1012. doi:10.1007/s10483-021-2746-8.
- [48] M. Kohansal-Vajargah, R. Ansari, Quadratic tetrahedral micropolar element for the vibration analysis of three-dimensional micro-structures, *Thin-Walled Structures* 167 (July) (2021) 108152. doi:10.1016/j.tws.2021.108152.
- [49] H. Bahaloo, Y. Li, Micropolar Modeling of Auxetic Chiral Lattices with Tunable Internal Rotation, *Journal of Applied Mechanics, Transactions ASME* 86 (4) (2019). doi:10.1115/1.4042428/446426.
- [50] J. Liu, Z. Y. Yin, L. Wu, P. Y. Hicher, Finite element implementation and application of a sand model in micropolar theory, *SN Applied Sciences* 3 (8) (2021) 1–14. doi:10.1007/S42452-021-04708-Z/FIGURES/15.
- [51] S. Massoumi, G. La Valle, Static analysis of 2D micropolar model for describing granular media by considering relative rotations, *Mechanics Research Communications* 119 (2022). doi:10.1016/J.MECHRESCOM.2021.103812.
- [52] F. Shi, N. Fantuzzi, Y. Li, P. Trovalusci, Z. Wei, Modeling of dilatancy effect in layered rock with rough interfaces using micropolar continuum, *Mechanics Research Communications* 125 (2022). doi:10.1016/J.MECHRESCOM.2022.103994.

- [53] J. Wan, D. Yang, X. Chu, W. Qu, A micropolar peridynamic differential operator and simulation of crack propagation, *Engineering Fracture Mechanics* 269 (2022) 108532. doi:10.1016/J.ENGFRACTMECH.2022.108532.
- [54] J. C. Frame, M. A. Wheel, P. E. Riches, A numerical investigation and experimental verification of size effects in loaded bovine cortical bone, *International Journal for Numerical Methods in Biomedical Engineering* 34 (1) (2018) e2903. doi:10.1002/CNM.2903.
- [55] H. Asadi, K. Javaherdeh, S. Ramezani, Micropolar fluid model for blood flow through a stenosed artery, *International Journal of Applied Mechanics* 5 (4) (2013). doi:10.1142/S1758825113500439.
- [56] V. A. Eremeyev, A. Skrzat, A. Vinakurava, Application of the Micropolar Theory to the Strength Analysis of Bioceramic Materials for Bone Reconstruction, *Strength of Materials* 48 (4) (2016) 573–582. doi:10.1007/s11223-016-9800-1.
- [57] J. Schijve, Note on couple stresses, *Journal of the Mechanics and Physics of Solids* 14 (2) (1966) 113–120. doi:10.1016/0022-5096(66)90042-1.
- [58] R. W. Ellis, C. W. Smith, A thin-plate analysis and experimental evaluation of couple-stress effects, *Experimental Mechanics* 7 (9) (1967) 372–380. doi:10.1007/BF02326308/METRICS.
- [59] Askar1972, Molecular crystals and the polar theories of the continua Experimental values of material coefficients for KNO₃, *International Journal of Engineering Science* 10 (3) (1972) 293–300. doi:10.1016/0020-7225(72)90044-4.
- [60] R. Gauthier, W. E. Jahsman, A Quest for Micropolar Elastic Constants, *Journal of Applied Mechanics* 42 (2) (1975) 369–374. doi:10.1115/1.3423583.
- [61] Richard David Gauthier, Analytical and Experimental Investigations in Linear Isotropic Micropolar Elasticity, Ph.D. thesis, University of Colorado (1974).
- [62] D. Bigoni, W. J. Drugan, Analytical derivation of cosserat moduli via homogenization of heterogeneous elastic materials, *Journal of Applied Mechanics, Transactions ASME* 74 (4) (2007) 741–753. doi:10.1115/1.2711225.
- [63] Z. He, H. Zhu, X. Wang, S. Ma, Experimental investigation on scale effect of mechanical properties of heterogeneous micropolar medium materials, *Composite Structures* 251 (2020) 112667. doi:https://doi.org/10.1016/j.compstruct.2020.112667.

- [64] R. S. Lakes, S. Nakamura, J. C. Behiri, W. Bonfield, Fracture mechanics of bone with short cracks, *Journal of Biomechanics* 23 (10) (1990) 967–975. doi:10.1016/0021-9290(90)90311-P.
- [65] R. S. Lakes, Reduced warp in torsion of reticulated foam due to cosserat elasticity: Experiment, *Zeitschrift fur Angewandte Mathematik und Physik* 67 (3) (2016). doi:10.1007/s00033-016-0632-4.
- [66] C. P. Chen, R. S. Lakes, Holographic study of conventional and negative Poisson’s ratio metallic foams: elasticity, yield and micro-deformation, *Journal of Materials Science* 26 (20) (1991) 5397–5402. doi:10.1007/BF02403936.
- [67] Z. Rueger, C. Ha, R. Lakes, Cosserat elastic lattices, *Meccanica* 54 (2019) 1983—1999. doi:10.1007/s11012-019-00968-7.
- [68] Z. Rueger, C. S. Ha, R. S. Lakes, Flexible Cube Tilt Lattice with Anisotropic Cosserat Effects and Negative Poisson’s Ratio, *Basic solid state physics* 256 (2019) 1800512.
- [69] D. R. Reasa, R. S. Lakes, Nonclassical chiral elasticity of the gyroid lattice, *Phys. Rev. Lett.* 125 (2020) 205502. doi:10.1103/PhysRevLett.125.205502.
- [70] Q. Zhang, W. Lu, F. Scarpa, D. Barton, R. Lakes, et al., Large stiffness thermoformed open cell foams with auxeticity, *Applied Materials Today* 20 (2020) 1–14. doi:10.1016/j.apmt.2020.100775.
- [71] E. Papa Dukić, L. Grbac, G. Jelenić, Characteristic bending length in micropolar materials with periodic internal structure, *Journal of Mechanics of Materials and Structures* (2024).
- [72] S. Valliappan, *Continuum mechanics : Fundamentals*, A. A. Balkema, Rotterdam, 1981.
- [73] X. Oliver, C. A. de Saracibar, *Continuum mechanics*, 2nd Edition, 2017. doi:10.13140/RG.2.2.25821.20961.
- [74] A. C. Eringen, E. S. Suhubi, Nonlinear theory of simple micro-elastic solids, *International Journal of Engineering Science* 2 (2) (1964) 189–203. doi:10.1016/0020-7225(64)90004-7.
URL <http://www.sciencedirect.com/science/article/pii/0020722564900047>

- [75] R. W. Ogden, Non-Linear Elastic Deformations, Dover Publications, Inc., Mineola, New York, 2013.
URL <https://books.google.com/books?id=52XDagAAQBAJ{&}pgis=1>
- [76] D. Hughes-Hallett, et al., Multivariable Calculus: Analytical Geometry III, 5th Edition, Wiley, Valencia Community College, 2011.
- [77] Anchordoqu, L., Lecture: Gauss' and Stokes' Theorems, Lehman College, City UNY, 2021.
URL <https://www.lehman.edu/faculty/anchordoqui/VC-4.pdf>
- [78] J. Brnić, Elastomehanika i plastomehanika, Školska knjiga - Zagreb, Sveučilište u Rijeci, 1996.
- [79] S. Hassanpour, G. R. Heppler, Micropolar elasticity theory: a survey of linear isotropic equations, representative notations, and experimental investigations, Mathematics and Mechanics of Solids (2015) 1–19doi:10.1177/1081286515581183.
- [80] J. Renton, Applied elasticity : matrix and tensor analysis of elastic continua, Woodhead Publishing, University of Oxford, UK, 2003.
- [81] R. S. Lakes, Physical meaning of elastic constants in cosserat, void, and microstretch elasticity, Mech. Mater. Struct 11 (2017) 1–13. doi:10.2140/jomms.2016.11.217.
- [82] A. C. Eringen, Microcontinuum Field Theories, Springer New York, 1999. doi:10.1007/978-1-4612-0555-5.
- [83] P. Neff, Relations of constants for isotropic linear Cosserat elasticity (2008).
- [84] S. Cowin, Stress functions for Cosserat elasticity, Int J Solids Struct 6(4) (1970) 389–398. doi:10.1016/0020-7683(70)90091-0.
- [85] L. Grbac, G. Jelenić, D. Ribarić, S. G. Erdelj, Hexahedral finite elements with enhanced fixed-pole interpolation for linear static and vibration analysis of 3d micropolar continuum, International Journal for Numerical Methods in Engineering 125 (8) (2024).
- [86] L. Žiković, B. Crnković, Analiza Kirschvog problema prema klasičnoj teoriji i mikropolarnoj teoriji elastičnosti, Primijenjena viša matematika (seminarski rad) (2020).
- [87] J. Brnić, M. Čanadija, Analiza deformabilnih tijela metodom konačnih elemenata, Fintrade & Tours d.o.o Rijeka, Sveučilište u Rijeci, 2009.

- [88] R. Courant, Variational methods for the solution of problems of equilibrium and vibrations, *Bull. Amer. Math. Soc.* 49 (1) (1943) 1–23.
- [89] O. C. Zienkiewicz, R. L. Taylor, D. Fox, *The Finite Element Method for Solid and Structural Mechanics: Seventh Edition*, Elsevier Ltd, 2013. doi:10.1016/C2009-0-26332-X.
- [90] Y. K. Cheung, M. F. Yeo, *A practical introduction to finite element analysis*, Pitman, 1979.
- [91] G. M., Three-node flat shell finite elements based on the cubic linked interpolation and the assumed strain method, Ph.D. thesis, Sveučilište u Rijeci, Građevinski fakultet (2022).
- [92] R. H. Macneal, Derivation of element stiffness matrices by assumed strain distributions, *Nuclear Engineering and Design* (1) 3–12. doi:10.1016/0029-5493(82)90262-X.
- [93] O. C. Zienkiewicz, Z. Xu, L. F. Zeng, A. Samuelsson, N. E. Wiberg, Linked interpolation for Reissner-Mindlin plate elements: Part I—A simple quadrilateral, *International Journal for Numerical Methods in Engineering* 36 (18) (1993) 3043–3056. doi:10.1002/nme.1620361802.
- [94] E. Wilson, R. Taylor, W. Doherty, J. Ghaboussi, Incompatible displacement models, in: *Numerical and Computer Methods in Structural Mechanics*, Elsevier, 1973, pp. 43–57. doi:10.1016/B978-0-12-253250-4.50008-7.
- [95] J.-L. Batoz, E. Antaluca, I. Katili, On the formulation and evaluation of old and new efficient low order triangular plate bending elements with shear effects, *Computational Mechanics* (1) 69–96. doi:10.1007/s00466-021-02020-6.
- [96] E. Reissner, On one-dimensional finite-strain beam theory: The plane problem, *Zeitschrift für angewandte Mathematik und Physik ZAMP* 23 (5) (1972) 795–804. doi:10.1007/BF01602645.
- [97] J. C. Simo, A finite strain beam formulation. The three-dimensional dynamic problem. Part I, *Computer Methods in Applied Mechanics and Engineering* 49 (1) (1985) 55–70. doi:10.1016/0045-7825(85)90050-7.
- [98] M. Borri, C. Bottasso, An intrinsic beam model based on a helicoidal approximation—Part I: Formulation, *International Journal for Numerical Methods in Engineering* 37 (13) (1994) 2267–2289. doi:10.1002/nme.1620371308.

- [99] C. L. Bottasso, M. Borri, Integrating finite rotations, *Computer Methods in Applied Mechanics and Engineering* 164 (3-4) (1998) 307–331. doi:10.1016/S0045-7825(98)00031-0.
- [100] G. Jelenić, E. Papa, Exact solution of 3D Timoshenko beam problem using linked interpolation of arbitrary order, *Archive of Applied Mechanics* 81 (2) (2011) 171–183. doi:10.1007/s00419-009-0403-1.
- [101] K. J. Bathe, *Finite Element Procedures*, Prentice Hall, New Jersey, 1996.
- [102] A. Tessler, S. B. Dong, On a hierarchy of conforming Timoshenko beam elements, Vol. 14, 1981. doi:10.1016/0045-7949(81)90017-1.
- [103] J. S. Przemieniecki, *Theory of Matrix Structural Analysis*, McGraw-Hill, New York, 1968.
- [104] J. N. Reddy, On locking-free shear deformable beam finite elements, *Computer Methods in Applied Mechanics and Engineering* 149 (1-4) (1997) 113–132. doi:10.1016/S0045-7825(97)00075-3.
- [105] E. Papa Dukić, G. Jelenić, Exact solution of 3D Timoshenko beam problem: Problem-dependent formulation, *Archive of Applied Mechanics* 84 (3) (2014) 375–384. doi:10.1007/s00419-013-0805-y.
- [106] J. C. Simo, L. Vu-Quoc, On the dynamics of flexible beams under large overall motions—the plane case: Part I, *Journal of Applied Mechanics, Transactions ASME* 53 (4) (1986) 849–854. doi:10.1115/1.3171870.
- [107] M. Gaćeša, G. Jelenić, Modified fixed-pole approach in geometrically exact spatial beam finite elements, *Finite Elements in Analysis and Design* 99 (2015) 39–48. doi:10.1016/j.finel.2015.02.001.
- [108] A. Arnold, M. and Cardona, O. Brüls, A lie algebra approach to lie group time integration of constrained systems, report no. 01 (2015).
- [109] B. C. Hall, *Lie Groups, Lie Algebras, and Representations*, Vol. 222 of Graduate Texts in Mathematics, Springer International Publishing, Cham, 2015. doi:10.1007/978-3-319-13467-3.
- [110] M. A. Crisfield, G. Jelenić, Objectivity of strain measures in the geometrically exact three-dimensional beam theory and its finite-element implementation, *Proceedings of the Royal*

- Society A: Mathematical, Physical and Engineering Sciences 455 (1983) (1999) 1125–1147. doi:10.1098/rspa.1999.0352.
- [111] M. Borri, C. Bottasso, An intrinsic beam model based on a helicoidal approximation—Part II: Linearization and finite element implementation, *International Journal for Numerical Methods in Engineering* 37 (13) (1994) 2291–2309. doi:10.1002/nme.1620371309.
- [112] G. Jelenić, M. A. Crisfield, Geometrically exact 3D beam theory: Implementation of a strain-invariant finite element for statics and dynamics, *Computer Methods in Applied Mechanics and Engineering* 171 (1-2) (1999) 141–171. doi:10.1016/S0045-7825(98)00249-7.
- [113] E. Papa Dukić, G. Jelenić, M. Gaćeša, Configuration-dependent interpolation in higher-order 2D beam finite elements, *Finite Elements in Analysis and Design* 78 (2014) 47–61. doi:10.1016/j.finel.2013.10.001.
- [114] V. Sonnevile, A. Cardona, O. Brüls, Geometrically exact beam finite element formulated on the special Euclidean group SE(3), *Computer Methods in Applied Mechanics and Engineering* 268 (2014) 451–474. doi:10.1016/j.cma.2013.10.008.
- [115] E. Papa Dukić, Configuration-Dependent Interpolation in Non-linear Higher-order 2D Beam Finite Elements, Phd thesis, University of Rijeka, Faculty of civil engineering (2013).
- [116] J. C. Simo, L. Vu-Quoc, A three-dimensional finite-strain rod model. part II: Computational aspects, *Computer Methods in Applied Mechanics and Engineering* 58 (1) (1986) 79–116. doi:10.1016/0045-7825(86)90079-4.
- [117] J. Argyris, An excursion into large rotations, *Computer Methods in Applied Mechanics and Engineering* 32 (1) (1982) 85–155. doi:https://doi.org/10.1016/0045-7825(82)90069-X.
- [118] M. Gaćeša, Fixed-Pole Concept in 3D Beam Finite Elements - Relationship to Standard Approaches and Analysis of Different Interpolations, Phd thesis, University of Rijeka, Faculty of civil engineering (2015).
- [119] J. Sorić, Metoda konačnih elemenata, Golden marketing - Tehnička knjiga, Zagreb, 2004.
- [120] A. Ibrahimbegović, F. Frey, I. Kožar, Computational aspects of vector-like parametrization of three-dimensional finite rotations, *International Journal for Numerical Methods in Engineering* 38 (21) (1995) 3653–3673. doi:https://doi.org/10.1002/nme.1620382107.

- [121] A. Cardona, M. Geradin, A beam finite element non-linear theory with finite rotations, *International Journal for Numerical Methods in Engineering* 26 (11) (1988) 2403–2438. doi:10.1002/nme.1620261105.
- [122] E. Papa Dukić, G. Jelenić, M. Gaćeša, Configuration-dependent interpolation in higher-order 2D beam finite elements, *Finite Elements in Analysis and Design* 78 (2014) 47–61.
- [123] M. Borri, L. Trainelli, C. L. Bottasso, On representations and parameterizations of motion, *Multibody System Dynamics* 4 (2-3) (2000) 129 – 193. doi:10.1023/a:1009830626597.
- [124] S. Mukherjee, J. Reddy, C. Krishnamoorthy, Convergence properties and derivative extraction of the superconvergent timoshenko beam finite element, *Computer Methods in Applied Mechanics and Engineering* 190 (26) (2001) 3475–3500. doi:10.1016/S0045-7825(00)00280-2.
- [125] M. Ranjbar, L. Škec, G. Jelenić, D. Ribarić, Mixed-mode delamination of layered structures modeled as timoshenko beams with linked interpolation, *International Journal for Numerical Methods in Engineering* 124 (8) (2023) 1773–1797. doi:10.1002/nme.7187.
- [126] M. Grbac, D. Ribarić, Three-node assumed strain mindlin plate finite elements, *ZAMM - Journal of Applied Mathematics and Mechanics / Zeitschrift für Angewandte Mathematik und Mechanik* 102 (6) (2022) 1 – 18. doi:10.1002/zamm.202100447.
- [127] R. L. Taylor, S. Govindjee, *FEAP: A Finite Element Analysis Program, User Manual*, University of California at Berkeley, Berkeley, California (2020).
URL <http://projects.ce.berkeley.edu/feap/>
- [128] S. Timoshenko, J. N. Goodier, *Theory of elasticity*, The Maple Press Company, New York, 1951.
- [129] G. N. Watson, *A Treatise on the Theory of Bessel Functions*, Cambridge University Press, 1995.
- [130] A. J. Beveridge, M. A. Wheel, D. H. Nash, The micropolar elastic behaviour of model macroscopically heterogeneous materials, *International Journal of Solids and Structures* 50 (1) (2013) 246–255. doi:10.1016/j.ijsolstr.2012.09.023.
URL <http://dx.doi.org/10.1016/j.ijsolstr.2012.09.023>

- [131] M. Sarhil, L. Scheunemann, J. Schröder, P. Neff, Size-effects of metamaterial beams subjected to pure bending: on boundary conditions and parameter identification in the relaxed micromorphic model, *Computational Mechanics* (2023). doi:10.1007/s00466-023-02332-9.
- [132] C. Geuzaine, J. F. Remacle, Gmsh: A three-dimensional finite element mesh generator with built-in pre- and post-processing facilities, last visited 2021-12-10.
URL <https://gmsh.info/>
- [133] B. Hassanati, M. Wheel, Quantifying numerically forecast size effects in the free vibration of heterogeneous beams, *International Journal of Mechanical Sciences* 152 (January) (2019) 298–311. doi:10.1016/j.ijmecsci.2019.01.009.
- [134] L. Žiković, G. Jelenić, N. Čeh, Axially loaded strip with circular hole – assessment of predictive capacity of micropolar continuum theory, Submitted (2023).
- [135] E. Kirsch, Die Theorie der Elastizität und die Bedürfnisse der Festigkeitslehre, *Zeitschrift des Vereines deutscher Ingenieure* 42 (1898) 797–807.
- [136] R. C. J. Howland, Stresses in a plate containing an infinite row of holes, *Proceedings of the Royal Society of London. Series A - Mathematical and Physical Sciences* 148 (864) (1935) 471–491. doi:10.1098/rspa.1935.0030.
- [137] S. G. Lekhnitskiy, *Anisotropic plates*, Gordon and Breach Science Publishers, New York, 1968.
- [138] A. E. Green, General bi-harmonic analysis for a plate containing circular holes, *Proceedings of the Royal Society of London. Series A. Mathematical and Physical Sciences* 176 (964) (1940) 121–139. doi:10.1098/rspa.1940.0082.
- [139] C. B. Ling, On stresses in a perforated strip, *Journal of the Franklin Institute* 303 (5) (1977) 405–414. doi:10.1016/0016-0032(77)90020-5.
- [140] L. Žiković, B. Crnković, Analiza kirschovog problema klasičnom i mikropolarnom teorijom elastičnosti, *Zbornik radova (Građevinski fakultet Sveučilišta u Rijeci)* 25 (1) (2022) 247–262. doi:10.32762/zr.25.1.16.

- [141] X. Lu, Y. Hou, Y. Tie, C. Li, C. Zhang, Crack nucleation and propagation simulation in brittle two-phase perforated/particulate composites by a phase field model, *Acta Mechanica Sinica* 36 (2) (2020) 493–512. doi:10.1007/s10409-020-00927-6.
- [142] P. L. Bishay, J. Sladek, N. Fabry, V. Sladek, C. Zhang, Perturbation finite element solution for chemo-elastic boundary value problems under chemical equilibrium, *Acta Mechanica Sinica* 35 (5) (2019) 981–991. doi:10.1007/s10409-019-00871-0.
- [143] Z. Hongwu, W. Hui, C. Biaosong, X. Zhaoqian, Parametric variational principle based elastic-plastic analysis of Cosserat continuum, *Acta Mechanica Solida Sinica* 20 (1) (2007) 65–74. doi:10.1007/s10338-007-0708-y.
- [144] S. Haitao, W. Yuanhan, The meshless virtual boundary method and its applications to 2D elasticity problems, *Acta Mechanica Solida Sinica* 20 (1) (2007) 30–40. doi:10.1007/s10338-007-0704-2.
- [145] E. G. Coker, The effects of holes and semicircular notches on the distribution of stress in tension members, *Proceedings of the Physical Society of London* 25 (1) (1912) 95–105. doi:10.1088/1478-7814/25/1/309.
- [146] A. M. Wahl, R. Beeuwkes Jr., Stress concentration produced by holes and notches, *Transactions of the American Society of Mechanical Engineers* 56 (1934) 617–625.
- [147] A. J. Durelli, C. A. Sciammarella, Elastoplastic Stress and Strain Distribution in a Finite Plate With a Circular Hole Subjected to Unidimensional Load This, *Journal of Applied Mechanics* 30 (1) (1963) 115 – 121. doi:10.1115/1.3630055.
- [148] G. E. Griffith, Experimental investigation of the effects of plastic flow in a tension panel with a circular hole, *National Advisory Committee For Aeronautics* TN 1705 (1948).
- [149] L. Toubal, M. Karama, B. Lorrain, Stress concentration in a circular hole in composite plate, *Composite Structures* 68 (1) (2005) 31–36. doi:10.1016/j.compstruct.2004.02.016.
- [150] J. Koord, J. L. Stüven, E. Petersen, O. Völkerink, C. Hühne, Investigation of exact analytical solutions for circular notched composite laminates under tensile loading, *Composite Structures* 243 (February) (2020) 112–180. doi:10.1016/j.compstruct.2020.112180.

- [151] Q. Yang, H. Cao, Y. Tang, Y. Li, X. Chen, materials Experimental Investigation of Stress Distributions in 3D Printed Graded Plates with a Circular Hole, *Materials* 14 (2021) 13. doi:10.3390/ma14247845.
- [152] Q. Wang, Q. Chen, Y. Chen, J. Li, Q. Li, The Effect of Internal Delamination Damage on the Tensile Strength of Aeronautical Composites, *Acta Mechanica Solida Sinica* 2022 35 (4) (2022). doi:10.1007/S10338-022-00335-2.
- [153] N. Momčilović, M. Motok, T. Maneski, Stress concentration on the contour of a plate opening: Analytical, numerical and experimental approach, *Journal of Theoretical and Applied Mechanics (Poland)* 51 (4) (2013) 1003–1012.
- [154] V. G. Aradhya, S.S.Kulkarni, Experimental Investigation of Stress Concentration Factor in an Isotropic and Orthotropic Plate with Multiple Circular Holes, *International Journal of Science, Engineering and Technology Research (IJSETR)* 4 (11) (2015) 3780–3784.
- [155] P. J. Romanowicz, B. Szybiński, M. Wygoda, Application of DIC method in the analysis of stress concentration and plastic zone development problems, *Materials* 13 (16) (2020). doi:10.3390/MA13163460.
- [156] P. J. Romanowicz, B. Szybiński, M. Wygoda, Preliminary experimental and numerical study of metal element with notches reinforced by composite materials, *Journal of Composites Science* 5 (5) (2021). doi:10.3390/jcs5050134.
- [157] W. Guo, W. Guo, Formulization of Three-Dimensional Stress and Strain Fields at Elliptical Holes in Finite Thickness Plates, *Acta Mechanica Solida Sinica* 32 (4) (2019) 393–430. doi:10.1007/s10338-019-00091-w.
- [158] E. Preuss, *Forschungsarbeiten (Mitteilungen ilber Forschungs- arbeiten)*, V. D. I. (134) (1913).
- [159] A. Henning, *Polarisationsoptische Spannungsuntersuchungen am gelochten Zugstab und am Nietloch*, *Forsch. Gebiete Ing.*, V. D. I. (4) (1933).
- [160] C. A. Sciammarella, A. J. Durelli, The Moire Fringe as a Means of Analyzing Strains, *Proceedings, The American Society of Civil Engineers* 87 (1) (1961).
- [161] C. A. Sciammarella, F. M. Sciammarella, *Experimental Mechanics of Solids*, John Wiley and Sons, 2012. doi:10.1002/9781119994091.

- [162] M. Motok, Stress concentration on the contour of the plate opening of an arbitrary corner radius of curvature, *Marine Structures* 1 (1997) 1–13.
- [163] V. A. Eremeyev, A. Skrzat, A. Vinakurava, Application of the Micropolar Theory to the Strength Analysis of Bioceramic Materials for Bone Reconstruction, *Strength of Materials* 48 (4) (2016) 573–582. doi:10.1007/s11223-016-9800-1.
- [164] C. European Standard, EN ISO 6892-1: Metallic materials-Tensile testing-Part1: Method of test at room temperature, European Committee for Standardization, Brussels, 2010.
- [165] University of Rijeka, Faculty of Civil Engineering, Laboratory Equipment Catalogue of the Faculty of Civil Engineering, last visited 2021-11-08.
URL <https://gradri.uniri.hr/laboratoriji/katalog-opreme/>
- [166] Zwick Roell Group, Testing software testXpert, last visited 2022-01-27.
URL <https://www.zwickroell.com/accessories/testing-software/testxpert-iii/#c67426>
- [167] A. Ambroziak, M. T. Solarczyk, A. Biegus, Numerical and Analytical Investigation of Aluminium Bracket Strengthening, *Archives of Civil Engineering* 64 (2) (2018) 37–54. doi:10.2478/ace-2018-0015.
- [168] HBM and HBK Company, Strain Gauges for Stress Analysis Catalogue, last visited 2021-11-16.
URL <https://www.hbm.com/en/>
- [169] National Instruments Corp, NI Signal Express, last visited 2022-01-27.
URL <https://www.ni.com/>
- [170] K. Panasiuk, Influence of effectiveness speed in mechanical properties of aw6060 t66 (pa38) alloy, *Journal of KONES* 24 (4) (2017) 219–226. doi:doi:10.5604/01.3001.0010.3133.
- [171] O. Glushko, A simple and effective way to evaluate the accuracy of digital image correlation combined with scanning electron microscopy (SEM-DIC), *Results in Materials* 14 (January) (2022) 30–32. doi:10.1016/j.rinma.2022.100276.
- [172] Siemens Digital Industries Software, Introduction to Strain Gauges, last visited 2022-03-28.
URL <https://community.sw.siemens.com/s/article/Introduction-to-Strain-Gauges>

- [173] R. D. Mindlin, H. F. Tiersten, Effects of couple-stresses in linear elasticity, *Archive for Rational Mechanics and Analysis* 11 (1) (1962) 415–448. doi:10.1007/BF00253946.
- [174] C. Wang, X. Zhang, P. Hu, Assumed stress quasi-conforming triangular element for couple stress theory, *Acta Mechanica Solida Sinica* 30 (4) (2017) 335–344. doi:10.1016/J.CAMSS.2017.07.006.

List of Figures

2.1	Initial (undeformed) and deformed configuration of the continuous body.	16
2.2	Internal forces and moments acting on a small surface of part I of the observed body under the action of an external load.	17
2.3	Arbitrary part of the body.	22
2.4	Tetrahedral element in continuum media with the mean stress and couple stress vectors on a slanted surface (left) and on surfaces with the normals parallel to the coordinate axes (right).	23
3.1	Initial and deformed state of a straight beam.	45
4.1	Hexahedral finite element with eight nodes - the relation between natural and global coordinates (according to [119])	59
4.2	Cantilever beam subject to the pure tension.	62
4.3	Distorted finite element mesh for the displacement patch tests (following [41]).	63
4.4	Discretised micropolar beam subjected to pure bending.	66
4.5	Convergence curves of <i>Hex8EFP</i> and <i>Hex8LI</i> elements for normalized vertical displacement u_2 when $l_b = 0.1$	67
4.6	Convergence curves of <i>Hex8EFP</i> and <i>Hex8LI</i> elements for normalized vertical displacement u_2 when $l_b = 1.8$	68
4.7	Solid circular cylinder under torsion.	69
4.8	Graphs of external load distribution	70
4.9	Comparison of numerical solutions for displacement u_θ and microrotation φ_{x_3} at node $(a, 0, c)$ with respect to lb/a	71
4.10	Schematic representation of the discretisation 3D micropolar plates.	72
4.11	Convergence study of first three natural frequencies of CCCC plate (<i>i</i>)	73
4.12	Convergence study of first three natural frequencies of CFFF plate (<i>ii</i>)	73

4.13	Convergence study of first three natural frequencies of CCCC plate with the circular hole (iii)	74
4.14	Convergence study of first three natural frequencies of CFFF plate with the circular hole (iv)	74
4.15	Quadrilateral finite elements with four and nine nodes in the natural coordinate system	78
4.16	Schematic representation of discretisation in numerical example (iii) and (iv) with a mesh of 10x10 elements per each quadrant.	80
4.17	Convergence study of the first three natural frequencies for the cantilever beam (i): Q4 elements on the left, Q9 elements on the right.	81
4.18	Convergence study of the first three natural frequencies for the fully clamped (ii): Q4 elements on the left side, Q9 elements on the right side.	82
4.19	Convergence study of the first three natural frequencies for the cantilever square plate with a circular hole (iii): Q4 elements on the left side, Q9 elements on the right side.	83
4.20	Convergence study of the first three natural frequencies for the circular plate with a circular hole (iv): Q4 elements on the left, Q9 elements on the right.	84
5.1	The geometry of internal structure for the analysed specimens, following [130]. . .	89
5.2	Perforated specimens B1-B4 with marked positions of applied forces and supports.	89
5.3	Set-up of HMD specimens subjected to the four-point bending.	91
5.4	The schematic representation of finite element mesh density for a unit cell.	93
5.5	Plotted numerical results for vertical displacement field of B1 model [mm].	94
5.6	Plotted numerical results for vertical displacement field of B2 model [mm].	94
5.7	Plotted numerical results for vertical displacement field of B3 model [mm].	94
5.8	Plotted numerical results for vertical displacement field of B4 model [mm].	94
5.9	Characteristic profiles P for calculating the average displacements.	95
5.10	Coupling number obtained from the inverse analysis based on the virtual experiment, and their linear regression.	97
6.1	PH Specimens.	107
6.2	Test specimens (TS) for determination of material properties.	108

6.3	Stress–strain curves for tested TS7- <i>i</i> specimens and according to Ramberg-Osgood relationship.	109
6.4	Used strain gauges from the manufacturer’s catalogue [168].	110
6.5	Strain-gauge positions (LI, RI - type K-CLY9x-1.5/120 placed inside the hole; LO, RO - type 1-LY5x-3/120 placed near the hole on the face of the specimen).	110
6.6	Preparation for strain measuring.	111
6.7	Experiment - a specimen subjected to uniaxial tension.	112
6.8	Strain measurements for the specimen PH10.	113
6.9	Strain measurements for the specimen PH15.	113
6.10	Strain measurements for the specimen PH20.	114
6.11	Control experiment - specimen subjected to uniaxial tension using pneumatic jaws.	115
6.12	Quarter-plate model with a circular hole subjected to uniaxial tension.	117
6.13	Finite element mesh around the hole of PH10 specimen [mm].	117
6.14	Parametric analysis of PH10 sample for internal strain gauges	122
6.15	Parametric analysis of PH15 sample for internal strain gauges	122
6.16	Parametric analysis of PH20 sample for internal strain gauges	122
6.17	Parametric analysis of PH10 sample for external strain gauges	123
6.18	Parametric analysis of PH15 sample for external strain gauges	123
6.19	Parametric analysis of PH20 sample for external strain gauges	123
6.20	Comparison between the experimental and numerical results based on the two theories for PH10 specimen type (r - distance from the hole rim to the specimen edge).	126

List of Tables

- 3.1 Coefficients m and k in the interpolations presented in Sections 3.2.2 - 3.2.5. 51
- 4.1 Numerical results for third displacement patch test: displacements/microrotation at P_9 , stress/couple stress at (0.07536, 0.03435, 0.02423). 64
- 4.2 Differences between analytical solutions and numerical results using *Hex8L* and *Hex8EFP*. 67
- 4.3 Comparison between analytical and numerical results at $(a, 0, c)$ for the cylinder subjected to the torque using hexahedral finite elements with the enhanced fixed-pole and Lagrangian interpolation. 71
- 4.4 Reference solutions of the first three natural frequencies (f_1, f_2 and f_3) of all four considered plate types. 73
- 4.5 Reference solutions for the first three natural frequencies (f_1, f_2 and f_3) of all four considered numerical example. 81
- 5.1 Dimensions of beam specimens [mm] [130]. 89
- 5.2 Positions of supports for specimens B1 and B4 (the specimens with different symmetry axis of geometry and internal structure) [mm]. 91
- 5.3 Positions of supports for specimens B2 and B3 [mm]. 91
- 5.4 The values of the maximum applied forces F [kN] on specimens B1 and B4 and the positions of their application [mm]. 92
- 5.5 The values of the maximum applied forces F [kN] on specimens B2 and B3 and the positions of their application [mm]. 92
- 5.6 The total number of finite elements for each type of model. 92
- 5.7 The average values of the vertical displacements computed from the virtual experiments on classical models B1-B4 for each characteristic profile. 96
- 5.8 Determined values for the coupling number and its average for each set-up. 97

6.1	Measured distances between the inner edge of each external strain gauge and the edge of the hole [mm].	111
6.2	Experimental measurements obtained by external and internal strain gauges for $F = 20$ kN.	114
6.3	Experimental measurements from both conducted experiments for $F = 10.5$ kN.	115
6.4	Comparison between Howland's analytical solution [136] and numerical results (using Q4 and Q9 finite elements) for the stress concentration factor at the edge of the hole.	118
6.5	Comparison between numerical and experimental results at the internal strain gauges.	119
6.6	Comparison between numerical and experimental results at the external strain gauges.	119
6.7	Combinations of parameters N and l_b for each specimen type providing the numerical results for the longitudinal strains equal to the experimental results obtained by the internal strain gauges.	124
6.8	Combinations of parameters N and l_b for each specimen type providing the numerical results for the longitudinal strains equal to the experimental results obtained by the external strain gauges.	125

Laura Grbac, née Žiković

Born on 31 October 1992 in Pula, Croatia. Attended the Technical High School for an architectural technician in Pula from 2007 to 2011. During the high school education, worked occasionally as an intern at the architecture and design company Vizual ARH. d.o.o., in addition to the mandatory professional practice.

Attended the Faculty of Civil Engineering at the University of Rijeka from 2011 to 2017 and received a bachelor's and a master's degree in the field of structural engineering. During master's studies worked as a draughtsman at Emis d.o.o (from 2012 to 2015) and as an undergraduate student teaching assistant (subject: Mechanics of Materials I) at the Faculty of Civil Engineering in Rijeka in the summer semesters of 2014 and 2015.

Shortly after graduation, worked as a structural engineer at Marecon d.o.o. on static and dynamic analysis and design of coastal structures. She worked on many projects at Marecon, among which the project of the San Pelagio port in Rovinj stands out.

In 2019, enrolled the postgraduate doctoral study programme in Civil Engineering in the field of Engineering mechanics and started a full-time position as a research assistant at the University of Rijeka, Faculty of Civil Engineering within the scientific projects *Fixed-Pole Concept in Numerical Modelling of Cosserats' Continuum - FIMCOS* (HRZZ-IP -2018-01-1732) and *Young Researchers' Career Development Project – Training New Doctoral Students*, financed by the Croatian Science Foundation under the supervision of Prof. Gordan Jelenić. During the last year of doctoral study, spent three months at the University of Ljubljana, Faculty of Civil and Geodetic Engineering under the supervision of Prof. Dejan Zupan.

List of Publications

1. L. Grbac, G. Jelenić D. Ribarić and S. Grbčić Erdelj, "Hexahedral finite elements with enhanced fixed-pole interpolation for linear static and vibration analysis of 3D micropolar continuum", *International Journal for Numerical Methods in Engineering*. 125(8):e7440, 2024., doi: 10.1002/nme.7440.
2. L. Grbac, G. Jelenić and N. Čeh, "Axially loaded strip with circular hole – assessment of predictive capacity of micropolar continuum theory", *submitted to Journal of Mechanics of Materials and Structures*, 2024.
3. E. Papa Dukić, L. Grbac and G. Jelenić, "Characteristic bending length in micropolar materials with periodic internal structure", *Journal of Mechanics of Materials and Structures*, 2024.
4. L. Grbac and G. Jelenić, "Interdependence of helicoidal and fixed-pole interpolation in linear elasticity with linked interpolation, and application in FE modelling of Cosserats' continuum", *Proceeding of the International Conference on Highly Flexible Slender Structures (HFSS 2023)*, Rijeka, 2023.
5. L. Grbac and G. Jelenić, "Vibracijska analiza 3D mikropolarnog kontinuuma uz primjenu fixed-pole interpolacije", *Zbornik radova 12. susreta Hrvatskoga društva za mehaniku*, Split, 2023.
6. L. Grbac and G. Jelenić, "Analiza prirodnih frekvencija 2D mikropolarnog kontinuuma", *Zbornik radova X. skupa mladih istraživača iz područja građevinarstva i srodnih tehničkih znanosti - Zajednički temelji 2023*, Split, 2023.
7. L. Žiković, G. Jelenić and E. Papa Dukić "Identification of coupling number in micropolar elasticity using laboratory or virtual experiments", *Proceeding of the 20th International Conference on Experimental Mechanics Applications in Materials Science (ICEM20)*, Porto, Portugal, 2023.
8. L. Žiković and B. Crnković, "Analysis of Kirsch's Problem Using Classical and Micropolar Theory of Elasticity", *Zbornik radova Građevinskog fakulteta u Rijeci*, 25(1); pp. 247-262, 2022.

9. L. Žiković and G. Jelenić "Quadrilateral 2D Finite Elements with Enhanced Fixed-Pole Interpolation in Linear Analysis of Micropolar Continuum", *Proceeding of the 10th International Congress of Croatian Society of Mechanics (ICCSM)*, Pula, 2022.
10. M. Ismail, L. Žiković, N. Čeh and G. Jelenić "Experimental and numerical analysis of stress concentration in a plate with a circular hole", *Proceeding of the 10th International Congress of Croatian Society of Mechanics (ICCSM)*, Pula, 2022.
11. L. Žiković and G. Jelenić "Experimental and numerical investigation of aluminium specimens with a circular hole subjected to tension", *Proceeding of the 38th Danubia-Adria Symposium on Advances in Experimental Mechanics*, Póros, Greece, 2022.
12. D. Jurković, L. Žiković, E. Papa Dukić and G. Jelenić, "Analytical, Experimental and Numerical Analysis of Pure Bending of Aluminum Beams with Artificially Produced Structure", *Zbornik radova Građevinskog fakulteta u Rijeci*, 24(1); pp. 51-65, 2021.
13. L. Žiković and G. Jelenić "Finite element analysis of micropolar continuum: application of the fixed-pole interpolation concept", *Book of Abstracts My First Conference 2021*, Rijeka, 2021.
14. E. Papa Dukić, L. Žiković and G. Jelenić "Experimental analysis of specimens with microstructure", *Proceeding of the 37th Danubia-Adria Symposium on Advances in Experimental Mechanics*, Linz, Austria, 2021.
15. L. Žiković and G. Jelenić, "Primjena fixed-pole interpolacije u dinamičkoj analizi Timošenkove grede", *Zbornik radova 11. susreta Hrvatskoga društva za mehaniku*, Rijeka, 2021.
16. L. Žiković and G. Jelenić, "Fixed-Pole Interpolation in Linear Analysis of Micropolar Continuum", *Proceeding of the 6th ECCOMAS Young Investigators Conference*, Valencia, Spain, 2021.
17. L. Žiković and G. Jelenić, "Fixed-pole interpolacija u linearnoj analizi mikropolarnog kontinuuma", *Zbornik radova 10. susreta Hrvatskoga društva za mehaniku*, Slavonski Brod, 2020.
18. L. Žiković and G. Jelenić, "Analiza 2D mikropolarnog kontinuuma metodom konačnih elemenata", *Zbornik radova sedmog skupa mladih istraživača iz područja građevinarstva i srodnih tehničkih znanosti - Zajednički temelji 2019*, Rijeka, 2019.

19. L. Žiković and G. Jelenić, "Primjena metode konačnih elemenata na ravninsku analizu mikropolarnog kontinuuma", *Zbornik radova 9. susreta Hrvatskoga društva za mehaniku*, Zagreb, 2019.